ABSTRACT

Title of Dissertation: SUBWAVELENGTH SPATIAL CONTROL AND MEASUREMENT OF COLD ATOMS VIA OPTICAL NONLINEARITY AND A NEW EXPERIMENTAL PLATFORM FOR TWO-SPECIES ATOM TWEEZER ARRAYS

Tsz-Chun Tsui
Doctor of Philosophy, 2022

Dissertation Directed by: Professor Steven Rolston
Professor Trey Porto
Joint Quantum Institute
National Institute of Standards and Technology
and
Department of Physics, University of Maryland

Cold atoms trapped in optical lattices have been proven to be a versatile, well-controlled and powerful platform for simulating and studying physics, from condensed matter systems to high energy physics and cosmology. However, the diffraction limit restricts the spatial resolution of light-induced confinement and measurement. Since the length scale of confinement sets a characteristic energy scale of the system, it is desirable to circumvent this diffraction limit to provide more control of the associated energy scale.

In the first half of this thesis, I describe a series of experiments that exploit the nonlinear optical response in the three-level system of ^{171}Yb to realize subwavelength spatial control and measurement of cold atoms. First, I report the experimental realization of a conservative optical lattice for cold atoms with subwavelength spatial structure. The

three-level system is coupled by two laser fields in a way that the dark state of the three-level system changes its spin composition over a narrow spatial region. The kinetic energy associated with this large gradient in the spin composition creates a lattice of narrow barriers with a width of 10 nm, which is one-fiftieth of the laser wavelength. Extending from this, I describe the realization of a wave-function density microscope with a spatial resolution of 10 nm and temporal resolution of 500 microseconds. Using the sharp spatial dependence in the spin composition of the dark state, we shelve narrow slices of the wave-function within every unit cell of the lattice into the selected spin state, which is then selectively read out to achieve subwavelength measurement of the atomic probability density. Finally, I report the stroboscopic realization of a $\lambda/4$-spaced lattice. We stroboscopically apply shifted versions of the lattice of narrow barriers mentioned earlier, thereby creating an effective time-averaged potential with a lattice spacing of $\lambda/4$.

In the past decade, significant progress has been made by extending the control of atoms to the single atom level, and single neutral atoms optically trapped in arrays have emerged as a compelling and scalable platform for quantum simulation and computing. A natural step is to extend to multi-species systems, which will help solve challenges encountered in single-species platforms.

In the second half of the thesis, I motivate and describe the construction of a new dual-species tweezer array apparatus. An inherent challenge in single-species platforms is the crosstalk between atoms due to the scattered photons from nearby atoms during site-selective control and measurement. A dual-species architecture with Rb and Yb can suppress unwanted crosstalk and even allow parallel tasking on Rb and Yb separately due to the large separation in resonance frequencies. Moreover, the use of multi-species

atoms provides an extra tuning knob that is useful in realizing multi-qubit gates. By manipulating the substantial difference in the intra- and inter-species van der Waals force, multi-qubit gates could be realized on Rb and Yb, giving significant speedups for some quantum algorithms and error-correction schemes.

SUBWAVELENGTH SPATIAL CONTROL AND MEASUREMENT OF COLD ATOMS VIA OPTICAL NONLINEARITY AND A NEW EXPERIMENTAL PLATFORM FOR TWO-SPECIES ATOM TWEEZER ARRAYS

by

Tsz-Chun Tsui

Dissertation submitted to the Faculty of the Graduate School of the
University of Maryland, College Park in partial fulfillment
of the requirements for the degree of
Doctor of Philosophy
2022

Advisory Committee:
Professor Steven Rolston, Chair/Advisor
Professor Trey Porto, Co-Advisor
Professor Ian Spielman
Professor Norbert Linke
Professor Ronald Walsworth (Dean's Representative)

Dedication

To Rui and my family

Acknowledgments

I still remember the day and how ignorant I was when I entered the lab for the first time. Pursuing a Ph.D. is not an easy task. It is impossible for me to get to where I am without the help from many others. I would like to take this chance to acknowledge the people who have helped me along the way in the past six years.

First, I want to thank my advisors, Trey Porto and Steve Rolston, who have led me through this long journey. Their physics knowledge and responsiveness are always remarkable and impressive to witness. Working with them over the years taught me the taste of physics, critical thinking, and how to get the priorities right. In addition, they have been very supportive throughout the years. Their doors are always open to students to answer their questions and provide help. They strike the right balance of being hands-off and supportive, which benefits me a lot in becoming an independent physicist. I am truly grateful for their mentor and advisory.

Over the years, I have been fortunate to work with amazing people on the experiment. Yang Wang, who was the post-doc in the RbYb mixture experiment, taught me the essential skills for AMO experiments and guided me through the steep learning curve. I really appreciate his patience and endurance with my ignorant questions when I was still a novice graduate student. Sarthak Subhankar, who has been a valuable member of the group for years, has made numerous contributions to the experiments. I am impressed by his

dedication to research shown throughout the years. Kevin Weber, who joined our group as a theorist, has been picking up his skills as an AMO experimentalist. Recently, he has been turning himself into an expert in optics in our group. Alan Tsidilkovski made a significant contribution to our lab and built the auto-alignment project for our 308 nm laser, which will save us from the hazardous alignment. I wish the best for the group and look forward to great results.

Furthermore, I would like to express my gratitude to members of the JQI community. I have to thank Alessandro Restelli, who has taught me almost all of my electronics knowledge and endured my ignorant questions. I am always amazed by how much he knows. He can always provide a solution when I encounter a problem with electronics. It would be impossible for me to finish the sideband locking project without his help and guidance. I also need to thank Joe Britton and Wance Wang for generously sharing their experience in aligning ULE cavities and lending their IR camera, which proved invaluable and saved us a lot of time. I also want to thank graduate students in JQI, who provided precious advice on various subjects, and lent us equipment that we probably did not return: Dalia Ornelas, Alexander Craddock, Patrick Banner, Deniz Kurdak, James Maslek, Ananya Sitaram, Hector Sosa Martínez, Swarnav Banik, Monica Gutierrez Galan, Shouvik Mukherjee, Yanda Geng, Hyok Sang Han, Ahreum Lee, Mingshu Zhao, and Junheng Tao. I need to thank Carlos Bracamontes Palma who designed and built the DDS that makes the wave-function density microscope and stroboscopic lattice paper possible. I also owe a special thank you to Peter Elgee, who helped us rebuild the baking oven and shared his knowledge on UHV. I also need to thank Josiland Chambers, who helped me to get through the paperwork for this defense.

I would like to thank my friend, Duli Shi, and her husband, Zheling Mei, who provided me food, free rides, emotional support throughout the years. Shout out to my friend since my undergraduate, Chung Hei Leung and Tian Chan. Thanks for organizing the trip to Virginia and introducing me to the energetic Delaware community, Ai Nin Yang, Ying Peng and Zeming. I need to thank Kyle and John for organizing the thesis writing meeting, which provided a good place for "complain therapy".

Finally, I want to thank my parents for their love and support. Most of all, I want to thank Rui, who gives me support and hope that our best years lie ahead of us. I am unbelievably fortunate to have met you in my PhD. Thank you for bringing color to my life. Thank you for comforting me when I was stressed and frustrated. I am beyond excited to start the new chapter of my life with you.

Table of Contents

List of Tables

List of Figures

List of Abbreviations

ADC	analog-to-digital converters
AOM	acousto-optic modulator
AR	anti-reflection
BNC	Bayonet Neill–Concelman
BO	Born-Oppenheimer
COM	center of mass
CF	ConFlat
CNC	computer numerical control
DAC	digital-to-analog converter
DDS	direct digital synthesis
EIT	electromagnetically induced transparency
EMCCD	electron multiplying charge coupled device
EOM	electro-optic modulator
FPGA	field-programmable-gate-array
FSR	free spectral range
FWHM	full width at half maximum
KP	Kronig-Penney
LIAD	light-induced atom desorption
MOT	magneto-optical trap
NA	numerical aperture
NEG	non evaporable getter
PCB	printed circuit board
PD	photodiode
PDH	Pound-Drever-Hall
PLL	phase lock loop
QAM	quadrature amplitude modulation
QND	quantum non-demolition
RAR	random anti-reflecting
RF	radio-frequency
RHS	right hand side
STIRAP	stimulated Raman adiabatic passage
STM	scanning tunneling microscope
TA	tapered amplifier
TOF	time-of-Flight

USB universal serial bus

Chapter 1: Introduction and Statement on Contributions

This dissertation consists of two main parts. The first half of the dissertation describes a series of experiments that exploit the non-linear optical response in a three-level system in ^{171}Yb atoms to realize subwavelength spatial control and measurement of cold atoms. It consists of three parts:

- Chapter 2 presents the experimental realization of a conservative optical lattice for cold atoms with subwavelength spatial structure. The potential is based on the nonlinear optical response of the laser-dressed dark-state in a three-level system, which is not constrained by the diffraction limit of the light generating the potential. This chapter is based on the publication [1]:

  Y. Wang, S. Subhankar, P. Bienias, and M. Łącki, T.-C. Tsui, M. A. Baranov, A. V. Gorshkov, P. Zoller, J. V. Porto, and S. L. Rolston, Dark State Optical Lattice with a Subwavelength Spatial Structure, Phys. Rev. Lett. 120, 083601 (2018).

- Chapter 3 presents the subwavelength optical measurement of atomic probability density within the unit cell of 1-D optical lattices with a resolution of 11 nm, which is 1/50 of the imaging light wavelength. This chapter is based on the publication [2]:

  S. Subhankar, Y. Wang, T.-C. Tsui, S. L. Rolston, and J. V. Porto, Nanoscale Atomic

Density Microscopy, Phys. Rev. X 9, 021002 (2019).

- Chapter 4 reports the realization of a $\lambda/4$-spaced lattice by stroboscopically applying optical Kronig-Penney-like potentials, which are generated using spatially dependent dark states as presented in Chapter 2. This chapter is based on the publication [3]:

  T.-C. Tsui, Y. Wang, S. Subhankar, J. V. Porto, and S. L. Rolston, Realization of a stroboscopic optical lattice for cold atoms with subwavelength spacing, Phys. Rev. A 101, 041603 (2020).

The experimental work on the optical lattice with subwavelength spatial structure in chapter 2 was undertaken by Yang Wang, Sarthak Subhankar and myself. Theory support was provided by Przemek Bienias, Mateusz Lacki, Mikhail Baranov, Alexey Gorshkov and Peter Zoller. This experiment was led by Yang. Yang and Sarthak upgraded the experimental apparatus for studying the dark state lattice. Yang and Sarthak collected and analyzed the data. Sarthak also performed a detailed analysis of the band structure. My efforts were primarily data collection, calibration on the Rabi frequencies and performing some preliminary calculations on the band structure.

Regarding the work on the nanoscale atomic density microscope in chapter 3, the experiment was operated by Sarthak, Yang and myself. I was primarily responsible for the data analysis and the calculations of the wave-functions of atoms in different lattices. For the work on the realization of a stroboscopic optical lattice in chapter 4, the experiment was operated by myself, Yang and Sarthak. I was primarily responsible for the data collection and data analysis. Sarthak Subhankar worked on the theoretical model for the stroboscopic lattices and provided the optimal ramping shape of the control beams.

The second half describes the design and the construction of a new experimental apparatus to trap Rb and Yb atoms in reconfigurable tweezer arrays and perform quantum computation and simulation tasks.

- Chapter 5 reviews some relevant properties of Rydberg atoms and motivates a dual-species Rydberg tweezer platform.
- Chapter 6 details the design and construction of the new experimental apparatus. The apparatus is still under construction, so only completed parts are discussed.

For the new dual-species Rydberg tweezer array apparatus, Sarthak was responsible for designing the vacuum system and the optical setup. Sarthak, Kevin Weber and I assembled the vacuum system and set up the laser systems. I designed the magnetic field coils and the electrodes for electric field control. I also developed the electronics for locking the Rydberg lasers. Sarthak and Kevin aligned the Rydberg laser beams to the ULE cavity for locking.

Chapter 2: Creation of Dark State Optical Lattice with Subwavelength Structure

Conservative optical potentials, such as optical dipole traps and optical lattices, have been used extensively in cold atoms experiments to confine the position and control the motion of atoms for optical clocks, simulating condensed matter systems, and quantum computing platforms [4, 5, 6, 7]. The spatial resolution of these optical potentials is typically limited by the diffraction limit, which is of order the wavelength of the light creating the potential landscape. For example, the lattice constant of a standard one-dimensional optical lattice formed by retro-reflecting a laser beam is $\lambda/2$. This fundamentally limits our capability to manipulate atoms. Moreover, the characteristic length scale of optical lattice systems sets the energy scale for both kinetic energy and interaction energy in the simulation of condensed matter systems, often posing stringent a temperature requirement to observe the quantum phenomenon of interest. There is, therefore, a desire to increase the fundamental energy scale of ultra-cold atoms by reducing the length scale of the system, thereby relieving the constraint on temperature.

Several approaches have been proposed or even demonstrated to overcome this diffraction limit, including lattices using multi-photon Raman processes [8], radio-frequency dressed optical potentials [9, 10], and trapping with near-field guided modes with

nanophotonic systems [11, 12]. An alternative approach is to utilize the non-linearity in the atomic response of a three-level system to circumvent the diffraction limit [13, 14]. Here, we present an experimental realization of a lattice for ^{171}Yb, which consists of a one-dimensional array of ultra-narrow barriers with widths less than 10 nm, well below the wavelength of the lattice light with ^{171}Yb [1]. By stroboscopically shifting the narrow barriers, a time-averaged potential with an effective lattice spacing below $\lambda/2$ can be realized as discussed in chapter 4. This chapter is based on a published work [1]. Sarthak Subhankar, the second author of this work and the senior graduate student, will discuss the technical details and calculations in his thesis. To avoid overlapping, I will report the main results from the paper.

2.1 Theory

The underlying principle of this approach utilizes the non-linearity of the atomic response to the driving laser field in a Λ-type three-level system, as illustrated in Fig. 2.1 (a). The two ground states, $|g_1\rangle$ and $|g_2\rangle$, are coupled to an excited state, $|e\rangle$, in a Λ-configuration by two optical fields separately: a standing-wave control field, $\Omega_c(x) = \Omega_c \sin(kx)$, where $k = 2\pi/\lambda$ and λ is the wavelength of light, and a weak constant probe field Ω_p propagating along the y-axis (see Fig. 2.1 (b) and (c)). To simplify the discussion, the lasers are assumed to be tuned to a zero two-photon detuning, $\delta = 0$, while the single-photon detuning, Δ, can be on- or off-resonant. The Hamiltonian of the atom consists of

kinetic energy and the internal atomic Hamiltonian:

$$H = \frac{-\hbar^2}{2m}(\frac{\partial}{\partial x})^2 + H_a, \tag{2.1}$$

$$H_a = \hbar((-\Delta - i\frac{\Gamma}{2})|e\rangle\langle e| + \frac{\Omega_c(x)}{2}|e\rangle\langle g_1| + \frac{\Omega_p}{2}|e\rangle\langle g_2| + \text{H.c.}). \tag{2.2}$$

In the regime of slow atomic motion, the kinetic energy term is small relative to the energy scale of the internal degree of freedom. Under the Born-Oppenheimer (BO) approximation, the spatially dependent eigen-states and eigen-energies of the internal degree can be obtained by diagonalizing the atomic Hamiltonian, $H_a(x)|E_\sigma\rangle = E_\sigma(x)|E_\sigma(x)\rangle$, where $\sigma = 0, \pm$ indicate the dark and bright states respectively. The Λ-configuration supports an atomic dark state, $|E_0(x)\rangle = \sin(\alpha(x))|g_1\rangle - \cos(\alpha(x))\,|g_2\rangle$, where $\alpha(x) = \arctan(\Omega_c(x)/\Omega_p)$, with energy $E_0 = 0$, so that the dark state is decoupled from the excited state $|e\rangle$ due to quantum interference. On the other hand, the two bright states $|E_\pm\rangle$ have an excited state component $|e\rangle$, leading to light scattering.

As shown in Fig. 2.1 (b), the control and probe beam are designed in a way that the composition of the dark state undergoes a rapid change over a narrow region determined by the ratio, $\epsilon = \Omega_p/\Omega_c$. In regions where $|\Omega_c(x)| \gg \Omega_p$, the dark state $|E_0\rangle$ is approximately $|g_1\rangle$. However, near the nodes of $\Omega_c(x)$, $|\Omega_c(x)| \ll \Omega_p$, and the composition of $|E_0\rangle$ becomes approximately $|g_2\rangle$. This substantial change in spin structure happens near the nodes of $|\Omega(x)|$ over a distance of $\epsilon\lambda/(2\pi)$, which is much smaller than the wavelength since $\epsilon \ll 1$ under the chosen laser configuration. For an atom prepared in the dark state, it will change its internal spin composition rapidly over the length $\epsilon\lambda/(2\pi)$ according to $|E_0\rangle$, assuming the atom is cold enough and the adiabaticity requirement is satisfied. As a result, there will

be quantum kinetic energy associated with this large gradient in the spin-wave composition giving rise to a conservative potential $V(x)$ for atoms in the dark state $|E_0\rangle$ [13, 14].

$$V(x) = \frac{\hbar^2}{2m_{\mathrm{Yb}}}(\frac{d\,\alpha(x)}{dx})^2 = E_R\frac{\epsilon^2\cos^2(kx)}{(\epsilon^2+\sin^2(kx))}, \tag{2.3}$$

where $k = 2\pi/\lambda$, $E_R = \hbar^2k^2/(2m_{\mathrm{Yb}})$ is the recoil energy, $\epsilon = \Omega_p/\Omega_c$, and m_{Yb} is the mass of the atom. The potential $V(x)$ can be considered as the non-adiabatic correction to the BO potential or artificial scalar gauge potential. When $\epsilon \ll 1$, the potential $V(x)$ has narrow barriers with the barrier height equal to E_R/ϵ^2, the full width at half maximum (FWHM) scaling as $0.2\lambda\epsilon$, and the lattice spacing being $\lambda/2$.

This dark state potential $V(x)$ has several features making it distinct from the conventional optical potentials based on ac-Stark shift. First, the explicit dependence of $V(x)$ on Planck's constant implies the quantum nature of this potential, while the typical optical potentials can be described classically as the interaction between induced dipoles and the optical fields. Second, unlike the typical optical potentials, which can be either repulsive or attractive, this dark state potential is always repulsive, since the gradients in wave functions always cost energy. Third, the potential $V(x)$ depends only on the ratio of Rabi frequencies $\epsilon = \Omega_p/\Omega_c$, but not the absolute values, making it relatively immune to technical noises if both fields are derived from the same laser.

2.2 Methods

In the following section, I discuss the experimental details of realizing the dark state potential with ultra-narrow barriers using ^{171}Yb, which has an electronic structure favorable

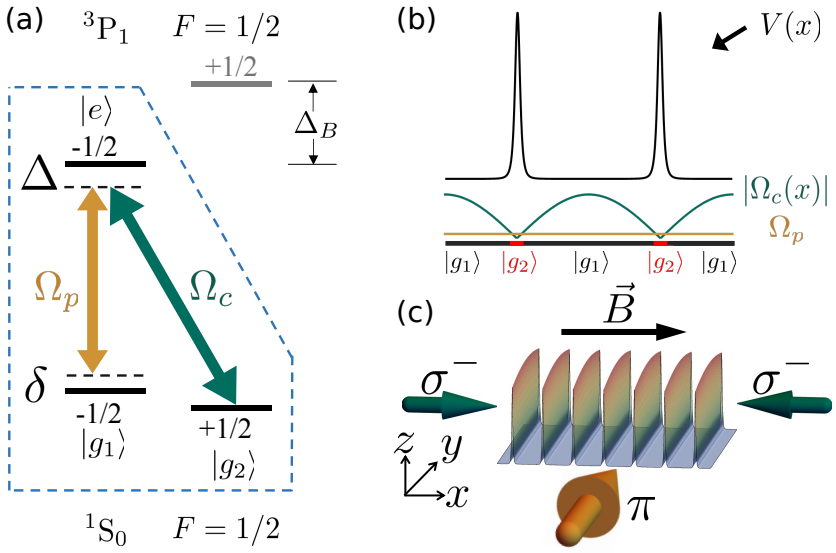

Figure 2.1: Level structure and experimental geometry. (a) The three states in ^{171}Yb used to realize the dark state lattices are separated from the $(^3P_1, F = 1/2, m_F = 1/2)$ state by a magnetic field of 12 mT. The three states are coupled by a strong σ^--polarized control field Ω_c (green) and a weak π-polarized probe field Ω_p (orange). (b) Spatial dependence of the dark state composited is created by a standing wave control field $\Omega_c(x)$ and a traveling probe field Ω_p. The rapid change in spin composition near the nodes results in the narrow barriers $V(x)$ (black). (c) The two counter-propagating σ^- beams creating the standing wave are aligned with the strong magnetic field along $\hat{x}$, while the π-beam travels along $\hat{y}$.

for achieving the Λ-system required for the potential. Ultracold Yb atoms are prepared by sympathetically cooling with ^{87}Rb atoms in a bi-chromatic crossed dipole trap. The details of the experimental apparatus and cooling sequence can be found in [15].

2.2.1 Realization of Λ-system in ^{171}Yb

The Λ-type three-level system is realized using three electronic states chosen from the $(^1S_0, F = 1/2)$ and $(^3P_1, F = 1/2)$ hyperfine manifolds. In the $(^1S_0, F = 1/2)$ manifold, the two ground states $(^1S_0, F = 1/2, m_F = \mp 1/2)$ comprise $|g_1\rangle$ and $|g_2\rangle$ respectively. The $m_F = -1/2$ state in the $(^3P_1, F = 1/2)$ manifold, with an inverse lifetime $\Gamma = 2\pi \times 182$ kHz acts as the excited state $|e\rangle$ in the Λ-configuration. The level structure of the $^1S_0$ and $^3P_1$ manifolds is shown in Fig. 2.1 (a). A magnetic field of 12 mT is applied to Zeeman split the two $^3P_1$ states by $\Delta_B = 1.8 \times 10^3\,\Gamma$, while the two $^1S_0$ ground states are only split by $-0.5\,\Gamma$ due to the absence of electronic magnetic moment leaving only the small nuclear magnetic moment in $^1S_0$ states. The presence of two and only two ground states, the large Zeeman shift of the $^3P_1$ states, and a relatively small linewidth of the intercombination transition between $^1S_0$ and $^3P_1$ manifold allow us to obtain a well-isolated three-level system with a reasonable magnetic field.

The three states, $|g_1\rangle$, $|g_2\rangle$ and $|e\rangle$, are coupled with the control and probe fields to give the Λ-system (Fig. 2.1). The standing-wave control field $\Omega_c(x)$, traveling along $\vec{B}$, is formed by two counter-propagating (σ_1 and σ_2) σ^--polarized laser beams that couple the $|g_2\rangle$ and $|e\rangle$ states with amplitudes $\Omega_{c1}\, e^{ikx}$ and $\Omega_{c2}\, e^{-ikx}$. The probe field is given by a third beam, which is traveling normal to $\vec{B}$ and π-polarized, coupling the $|g_1\rangle$ and $|e\rangle$ with an amplitude

$\Omega_p\, e^{iky}$. The off-resonant coupling between $|g_2\rangle$ and $|e\rangle$ by the π-polarized probe beam is suppressed by the Zeeman shift of Δ_B =1.8×10$^3\,\Gamma$. The frequency of the three beams can be tuned to set the single and two-photon detunings, Δ and δ. Two-photon detuning $\delta = 0$ is defined as the dark state condition for an isolated three-level system. However, off-resonant couplings to other states in the ($^3P_1$, $F = 1/2, 3/2$) manifolds introduce light shifts, which requires non-zero δ to maintain the dark state condition. In addition to the laser frequency, the polarization of the control and probe beams needs to be well controlled. The polarization of the beams is sensitive to the alignment of the beams $\vec{k}_p$, $\vec{k}_{ci}$, with respect to the magnetic field $\vec{B}$. The alignment of the k-vector of the beams to the magnetic field is achieved by measuring the atom loss in an off-resonant EIT configuration. The details of this technique are discussed in the published work [1] and Sarthak's thesis.

2.2.2 Dark State Lattice Loading Procedure

After the sympathetic cooling process detailed in [15], approximately 2×10^5 Yb atoms are collected with a temperature T of $\approx$ 300 nK ($T = 1.1\ T_F$, where T_F is the Fermi temperature). A temperature of 300 nK corresponds to 1.6 E_R, where E_R is the recoil energy. The magnetic field in the x-direction is then ramped up to 12 mT in 100ms, removing the remaining magnetically confined Rb atoms. To adiabatically load the Yb atoms into the ground band of the dark state lattice, in addition to cooling the external atomic motion to a sufficiently low temperature, we also need to properly prepare the internal state of the atoms, as the dark state potential arises from the twist in the internal state composition. Therefore, we first optically pump the Yb atoms into $|g_1\rangle$ with a 50 ms

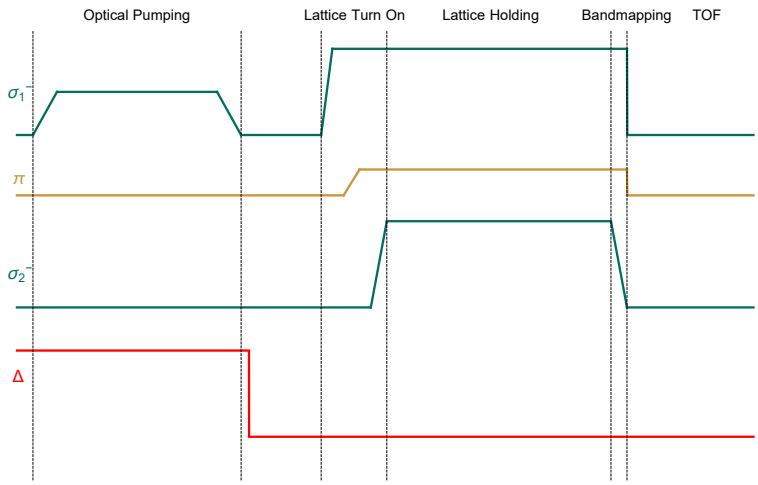

Figure 2.2: Procedure to adiabatically load atoms into the ground band of the dark state lattice and to perform bandmapping at the end of the sequence.

pulse of σ_1 beam with $\Delta = 12$ MHz, resulting in $\approx 1.5{\times}10^5$ Yb atoms polarized in $|g_1\rangle$. Then, Δ is changed to the final desired value. The next step is to populate the atoms into a homogenous dark state. The power of the σ_1 beam is first ramped up, after 1 ms wait time, the π-polarized probe beam is ramped on in 0.3 ms. The atoms are transferred from $|1\rangle$ into a spatially homogeneous dark state in the σ_1-π configuration. Finally, σ_2 is ramped on to give a twist in the dark state composition, adiabatically loading the atoms into the dark state potential. The loading procedure is illustrated in Fig. 2.2.

This narrow dark state potential originates from the large gradients of spin-wave composition near the nodes of the standing-wave control field, where $|\Omega_c(x)| \ll \Omega_p$. In our experimental setup, the standing-wave control field is generated from the two counter-propagating σ^- laser beams, σ_1 and σ_2, while the probe field comes from a π-polarized beam normal to the control beams. Therefore, the Rabi frequencies of the three beams need to be well-calibrated, since a slight imbalance in the Rabi frequencies of the two

control beams will invalidate the requirement of $|\Omega_c(x)| \ll \Omega_p$ near the nodes and thus significantly diminish the dark-state barriers. I will discuss the calibration of the Rabi frequencies before showing the measurement results.

2.2.3 Rabi Frequency Calibration

We calibrate the Rabi frequencies of the two control beams and the probe beam by measuring two-photon Raman Rabi frequencies, Ω_R, and light-shift induced Raman detuning, δ_R, of the control-probe pairs of beams as a function of their beam powers. In the calibration, we use a large single-photon detuning $\Delta \gg \Gamma, \Omega$, such that the excited state $|e\rangle$ can be adiabatically eliminated and the three-level system is effectively reduced to a two-level system with states, $|\vec{p}\rangle|g_1\rangle$ and $|\vec{p} + 2\delta\vec{k}\rangle|g_2\rangle$. Ω_R and δ_R are extracted by measuring the center of mass (COM) motion of the atomic cloud. In addition to transferring the population between the two ground states, the two-photon Raman transition imparts a momentum kick on the atoms, which manifests itself in the COM of the cloud, providing a measure of the ground state population. Fig. 2.3 (a) shows typical Rabi oscillation data, which are fitted to a damped sinusoidal function to determine Ω_R. The expressions for the two-photon Rabi frequency Ω_R and Raman detuning δ_R are

$$\Omega_R = \frac{\Omega_{ci}\Omega_p}{2\Delta}, \tag{2.4}$$

$$\delta_R = \delta + 4\omega_R \left(\frac{\vec{p} \cdot \delta\vec{k} + |\delta\vec{k}|}{|\delta\vec{k}|} \right) - \frac{\Omega_{ci}^2}{4\Delta} + \frac{\Omega_p^2}{4\Delta}, \tag{2.5}$$

where $2\delta\vec{k} = \vec{k_c} - \vec{k_p}$, $\omega_R = \frac{\hbar^2|\delta\vec{k}|^2}{2m_{\mathrm{Yb}}}$, $\vec{k_c}$ and $\vec{k_p}$ are the k-vectors for one of the control beams

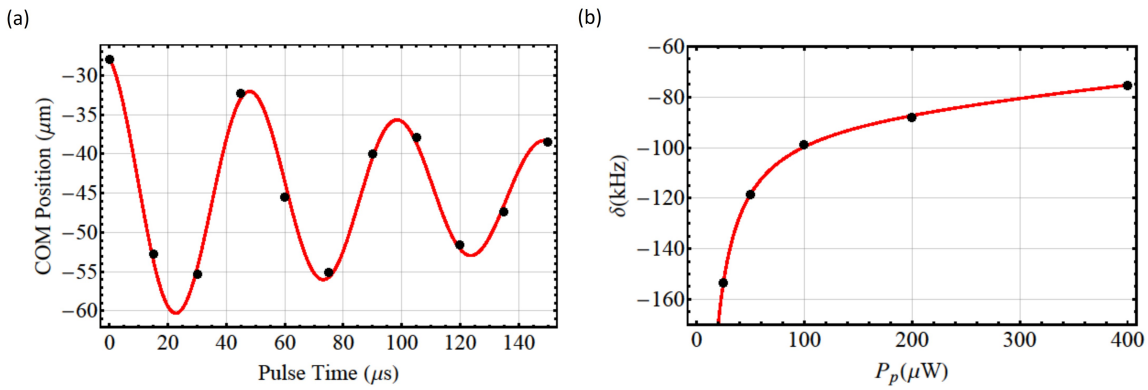

Figure 2.3: Measured data for Rabi frequency calibration. (a) Example data of the center of mass oscillation of the atomic cloud as a function of the Raman pulse time. (b) Measured two-photon resonance δ as a function of the probe beam power P_p

and probe beam respectively.

However, Ω_R can only give the product of Ω_{ci} and Ω_p, but not the proportionality constants between the power and Rabi frequency of the separate beams. In order to find the proportionality constants, we make use of both the relations Eq. 2.4 and Eq. 2.5. Defining $\Omega_p^2 = A_p P_p$, we obtain $\Omega_{ci} = 2\Omega_R\Delta/\sqrt{A_p P_p}$ using Eq. 2.4. Then, we replace Ω_{ci} in Eq. 2.5 with $2\Omega_R\Delta/\sqrt{A_p P_p}$ and the second term in Eq. 2.5 with a fitting parameter ξ. At Raman resonance, $\delta_R = 0$, Eq. 2.5 is rewritten as,

$$\delta = -\xi + \frac{\Omega_R^2\Delta}{A_p P_p} - \frac{A_p P_p}{4\Delta}. \tag{2.6}$$

Experimentally, we first perform a scan to obtain a set of Rabi oscillation data and Ω_R for a chosen set of P_{ci}, P_p with $\Delta = -40$ MHz. Then, we fix Δ, but vary P_{ci} and P_p to keep Ω_R the same, and then scan for the values of δ that satisfy Eq. 2.6 for different P_p as

shown in Fig. 2.3 (b). We fit the measured data as a function of P_p using Eq. 2.6 with A_p and ξ as the fitting parameters. A_{ci} can be derived from Eq. 2.4 using the fitted value of A_p. For the data used in this measurement, A_p, A_{c1} and A_{c2} were found to be 6288, 14201 and 26982 $(\times(2\pi)\,\mathrm{kHz})^2/\mu\mathrm{W}$ respectively. In a typical experiment, P_{c1}= 2857 μW, P_{c2}= 1503 μW and P_p= 527 μW, which gives $\Omega_{c1} = \Omega_{c2} = 35\ \Gamma$ and $\Gamma_p = 10\ \Gamma$. We are able to balance the Rabi frequency of the two control beams to within 2 %.

2.3 Results

2.3.1 Momentum Distribution by Bandmapping

In order to prove the existence of this dark state lattice, we measure the momentum distribution of Yb atoms along the direction of the lattice, by mapping the momentum distribution of the atoms into the spatial distribution with the time-of-flight (TOF) technique. The periodically arranged dark-state barriers give rise to bandgaps between Bloch bands. The bandgaps give rise to unoccupied momentum states resulting in visible band edges after TOF. We perform bandmapping at the end of the experiment by adiabatically ramping down Ω_2 in 0.5 ms (ramping down the barrier height), and then turning off the σ_1 beam, the probe beam and the optical dipole trap. This maps atoms with given quasimomentum in the lattice to real momentum in free space. We then take an absorption image to measure the momentum along $\hat{x}$ and $\hat{z}$ after 12 ms TOF. Since the Yb atoms have been cooled to $T = 300$ nK $= 1.6\ E_R$, which is less than the bandgap between the ground band and the first excited band, the ground band is predominately populated and distinct band edges are visible in the TOF image after band mapping as shown in

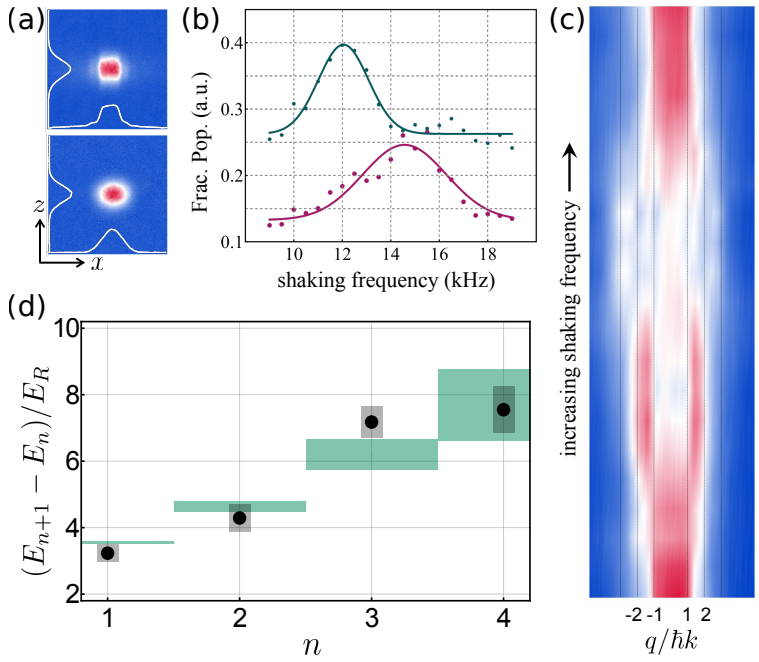

Figure 2.4: (a) The results of band mapping with three beams (upper) and with only Ω_c beams (lower). The white traces show the integrated momentum distribution in each direction ($\hat{x}$ is the lattice direction). (b),(c) Band spectroscopy: in (c), we integrate the momentum distribution in band mapping results over z after shaking and plot this TOF column density vs the shaking frequency; in (b), we plot the fractional population (frac. pop.) excited to the p band (dark green) and d band (magenta) vs shaking frequency. Gaussian fits [colored lines in (b)] are used to determine the center frequency and the width of the transition. (d) Band spacing: $E_{n+1} - E_n$ is plotted vs the band index n of a dark state lattice with Ω_c =70 Γ, Ω_p = 10 Γ, Δ = 22 Γ, and $\delta = 0$, The grey vertical bars show the measurement-inferred transition width, while the green rectangles are expected band spacings and widths from calculations.

upper panel in Fig. 2.4 (a). The lower panel shows the result with no probe beam, where we find a nearly Gaussian distribution in the lattice direction. This proves that the band edges in the upper panel of Fig. 2.4 (a) originate from the spin structure, not a simple ac-stark shift type lattice from the control beams.

2.3.2 Band Structure and Shaking Spectroscopy

Proving the existence of lattice structure is not sufficient to definitively say we have created dark state lattice with subwavelength structure. To do so, we further investigate the band structure of the lattice by shaking spectroscopy, which allows us to measure the energy separation between neighboring Bloch bands. In shaking spectroscopy, atoms are excited from lower to higher bands when the modulation frequency matches the band spacing. In the dark state lattice, the barriers are located at the nodes of the standing-wave $\Omega_c(x)$ field, so the lattice is shaken by modulating the phase of the σ_2 beam with respect to the σ_1 beam using an analog RF phase-shifter on the RF drive to the AOM for the σ_2 beam. After shaking for 200 μs with an amplitude of $\lambda/8$, we perform the band mapping procedure by ramping down the σ_2 beam in 0.5 ms. The atoms in different bands are separated spatially after a TOF enabling us to determine the population in different bands as shown in Fig. 2.4 (c).

For small $\epsilon = \Omega_p/\Omega_c$, the dark state lattice maps to a one-dimensional Kronig-Penney (KP) lattice, which has a characteristic feature of having the n-th band energy scales as $n^2 E_R$. Therefore, the first characteristic feature of the dark state lattice is that the band spacing increases linearly with n. In contrast, in a deep sinusoidal lattice, band spacing

decreases with n. Figure 2.4 (d) plots the frequency-dependent excitation into the first (p) and second (d) excited bands for $\epsilon = 0.14$, extracted from the data in Fig. 2.4 (c). The coupling by shaking the lattice has odd parity, so only transitions between bands with opposite parity are allowed i.e. $s \rightarrow p$ and $p \rightarrow d$. The transition from the s to d band involves a two-step process, $s \rightarrow p$ followed by $p \rightarrow d$. Consequently, this may result in a small systematic shift in resonance frequency as detailed in [1]. The band structure is mapped up to the g band (the fourth excited band). The energy spacings for adjacents bands increase monotonically with n as shown in Fig. 2.4 (d) coinciding with the characteristic band spacings of the dark state lattice. The green rectangles show the theoretical band spacings and widths, calculated from a model that includes both the light shifts from states outside the three-level system and mixing with the bright states [1].

Another distinctive feature of the dark state lattice is that, in the high barrier limit, the band structure becomes almost independent of the barrier strength (the area under the potential for a single barrier), which scales with $1/\epsilon$. Fig. 2.5 (a) shows the band structure at different ϵ for fixed $\Omega_c = 100\ \Gamma$ and different Ω_p. The measured spacings are indeed almost independent of the value of ϵ, even though the probe power varies by an order of magnitude. When ϵ becomes smaller than 0.1, another effect comes into play. The height of V(x) becomes comparable to the energy separation between the dark state $|E_0\rangle$ and the upper bright state $|E_+\rangle$, resulting in a significant mixing between $|E_0\rangle$ and $|E_+\rangle$. The upper panels of Fig. 2.5 (a) show the potentials of the upper bright state (blue) and dark state (green) for three ϵ. This mixing between the dark and bright states modifies the band structure substantially. At a particular value of $\epsilon \approx 0.125$, the tunneling of atoms across the barriers is suppressed due to destructive interference between the normal

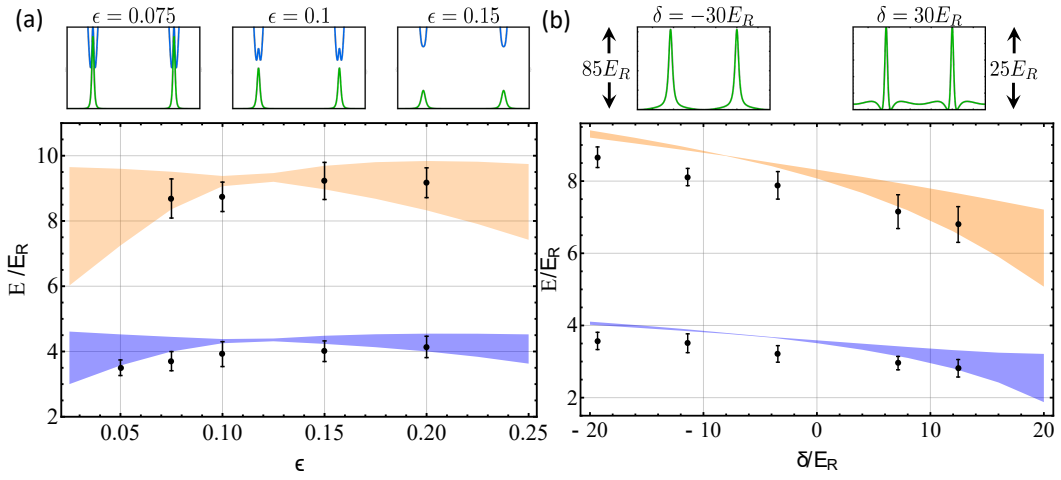

Figure 2.5: Band structure dependence. Energies of the p band and the d band with respect to the s band are plotted. (a) Dependence on ϵ: Ω_c = 100 Γ, Ω_p = 5-20 Γ, Δ= 22 Γ, and δ = 0. The shaded regions are the transition energies predicted from a model including couplings to the bright states. (Upper) Representative potentials for the dark states (green) and bright states (blue). At $\epsilon = 0.075$, the bright and dark states are no longer good basis states because of the strong coupling between them. (b) δ dependence: $\Omega_c = 70$ Γ, $\Omega_p = 10$ Γ, $\Delta = 22$ Γ. (Upper) Calculated dark state potentials for positive and negative δ.

hopping within the dark state and the bright-state assisted hopping resulting in a vanishing bandwidth despite barriers having finite width and height. The shaded regions in Fig. 2.5 (a) are calculations based on a model that includes bright state couplings. The residual discrepancy between theory and experiment is attributed to polarization imperfections, Rabi frequency calibration and limitations of our shaking band spectroscopy.

We also look into the situation in which the dark state condition is not satisfied $\delta \neq 0$. Since the state is no longer completely dark, there exists an additional periodic potential due to the couplings to the population in the excited states as well as neighboring hyperfine states. This additional potential distorts the dark state lattice and its band structure. The band spacings measured as a function of δ agree with the prediction (shaded area) (Fig. 2.5 (b)), with the systematic deviation probably caused by the same factor as in Fig. 2.5 (a).

2.3.3 Dissipation and Lifetime

Finally, we study the dissipation of $V(x)$ filling in the last piece of evidence that we create the desired dark state potential in our system. The narrow dark state barriers $V(x)$ can be viewed as the non-adiabatic correction to the dark state, which couples weakly to the bright states. This coupling to the bright states, which contains some population in the excited state $|e\rangle$, leads to light scattering and thus heating atoms out of the trap. This results in a significant difference in the dependence of lifetime on both the detuning Δ and the laser power of the dark state lattice compared to a regular lattice. In stark contrast to a standard optical lattice arising from ac-Stark shifts, which have a lifetime independent of

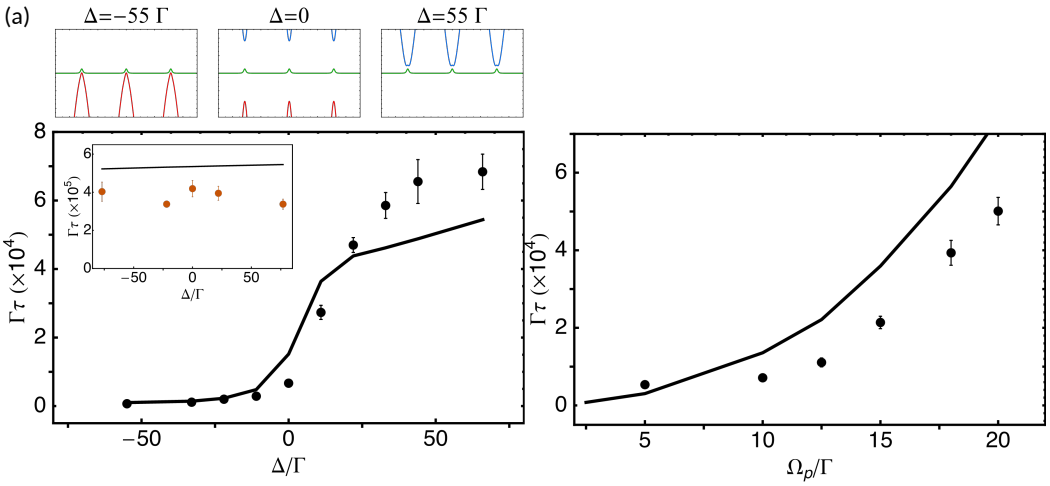

Figure 2.6: Lifetime of dark state lattice τ scaled by the excited state lifetime Γ vs Δ, with $\Omega_c = 70\ \Gamma$, $\Omega_p = 10\ \Gamma$, and $\delta = 0$. (Inset) Lifetime of the dark state in spatially homogeneous control fields, with $\Omega_{c1} = 35\ \Gamma$, $\Omega_{c2} = 0$, $\Omega_p = 10\ \Gamma$, and $\delta = 0$ (Upper three panels) The two bright state potentials $E_-(x)$ (red) and $E_+(x)$ (blue), and the dark state potential (green), at different Δ. (b) Lifetime vs Ω_p in a dark state lattice where $\epsilon = 0.2$ and $\Delta = 0$. The solid black lines are predictions scaled with a factor of 2.2 [except for (a) inset, where no scaling is applied.] The error bars represent 1 standard deviation uncertainty from fitting the population decay data.

the sign of Δ, the lifetime τ of atoms in a dark state lattice is considerably longer for $\Delta > 0$ than for $\Delta < 0$. There are two primary loss mechanisms for the dark state lattice. The first one is due to small admixture of $|E_{\pm}\rangle$, which gives rise to photon scattering by $|e\rangle$ and is insensitive to the sign of Δ. The second loss channel is due to atoms decaying into the untrapped $|E_{-}\rangle$ from the trapped $|E_0\rangle$ due to the non-adiabatic coupling between the two states. This process is highly Δ-dependent due to the Δ-dependent proximity of the bright-state potential, as illustrated in the upper panel of Fig. 2.6. The wave-function density of atoms in $|E_0\rangle$ is negligible near the barriers resulting in considerably lower overlap in wave-function and thus coupling between $|E_0\rangle$ and $|E_{+}\rangle$, resulting in the Δ asymmetry in lifetime. The measured lifetime is plotted as a funciton of Δ in Fig. 2.6 with the calculation results depicted as the black line. For comparison, the measured lifetime in a homogeneous control field when one of the control beams is blocked is shown in Fig. 2.6 (inset). Atoms in this homogeneous dark state are measured to have a lifetime $\simeq 4{\times}10^5/\Gamma$ independent of Δ as expected, and is 70 % of the expected lifetime from the calculation.

The loss mechanism of non-adiabatic bright state coupling also leads to a counter-intuitive dependence of the lifetime on the laser power. Figure 2.6 shows the measured lifetime at constant ϵ as a function of Rabi frequencies. Remarkably, the lifetime increases with Rabi frequencies, in contrast to the case of a regular optical lattice in which the lifetime does not improve by increasing laser power of fixed detuning. For the dark state lattice, an increase in $\Omega_{c,p}$ results in a larger energy separation between the BO potentials, suppressing the non-adiabatic coupling loss between dark and bright states.

2.4 Outlook

Having realized the dark state potential with ultra-narrow barriers, a natural step is to use these barriers to create lattices with lattice spacing smaller than $\lambda/2$, by stroboscopically applying the shifted versions of the lattice, which would significantly increase the characteristic energy scales relevant for interacting many-body atomic systems. Starting with a dark state lattice with a barrier height of 100 E_R and a lattice spacing of $\lambda/2$, by shifting the lattice by a distance $\lambda/(2N)$ at stroboscopic time T/N, we can create a time-periodic potential $V(x,t)$ with a period T [16]. If T is much smaller than the typical timescale of atomic motion, the atoms will experience a time-averaged potential with an effective lattice spacing of $\lambda/2N$ and an effective barrier height of $(100/N)E_R$. To realize this stroboscopic scheme with the dark state potential, we can shift the nodes of $\Omega_c(x)$, where the barriers are located, time-periodically. The details of the realization of a stroboscopic lattice with subwavelength lattice spacing are discussed in chapter 4.

In addition, the spin localization on small length scales can be used to measure the ensemble-averaged wave-function of atoms in an optical lattice and even observe the dynamics of atoms excited into periodic motion. Under the experimental configuration of the dark state lattice, the resulting dark state composition is predominantly $|g_1\rangle$ away from the nodes of $|\Omega_c(x)|$, and $|g_2\rangle$ near the nodes, where $\Omega_p \gg |\Omega_c(x)|$. Much like an STM, the wave-function probability density $|\psi(x)|^2$ can be mapped out by measuring population in $|g_2\rangle$. Following this idea, we have measured the wave-function density and dynamics of atoms in a sinusoidal and a KP lattice as detailed in chapter 3. There are also other possible applications of this dark state potential. For example, such sharp potential barriers

could be useful for the creation of narrow tunnel junctions for quantum gases [17] or for building sharp-wall box-like traps [18]. The dark state lattice is generalizable to 2D and, for example, can be used to study Anderson localization with random strength in the barrier height [19].

Chapter 3: Nanoscale Atomic Density Microscopy

High-resolution microscopy plays an essential role in almost all scientific fields revealing the underlying physics, chemistry, and biology of a variety of systems. In cold atom physics, high-resolution microscopy enables the visualization of numerous quantum phenomena, including the Mott transition [20, 21], quantum correlation [22, 23], and quantum tunneling [24, 25]. However, since the discovery by Ernst Abbe in 1873, it has been known that a far-field light microscope would not be able to resolve objects beyond the diffraction limit. Various techniques have been developed in different fields to overcome this optical diffraction limit. Utilizing the non-linear optical response of the target medium, molecules can be imaged with resolution beyond the diffraction limit [26]. For cold atoms, non-linear optical response in a dark state can be exploited to achieve subwavelength addressing as suggested in the proposals [27, 28] and first demonstrated in the experiment using a thermal gas [29].

This chapter describes the realization of a wave-function density microscope with unprecedented spatial resolution of 11 nm, which is well below the diffraction limit. This superresolution microscope allows us to measure and distinguish the ensemble-averaged probability density of atoms in two different types of lattices. Moreover, the microscope has a temporal resolution of 500 ns, which is high enough to measure wave-function dynamics

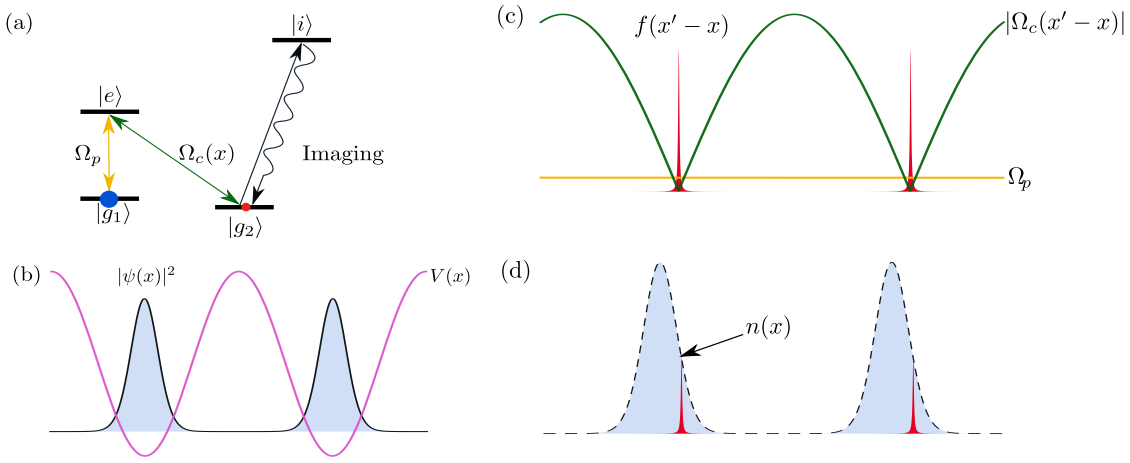

Figure 3.1: Principle of our nanoscale atomic density microscope. (a) Configuration of the control field $\Omega_c(x)$ and probe field Ω_p coupling $|g_1\rangle$, $|g_2\rangle$, and $|e\rangle$ in a Λ-system. Population in $|g_2\rangle$ is measured via a cycling transition connecting the imaging state $|i\rangle$. (b) Probability density $|\psi(x)|^2$ in the lattice of interest $V(x)$. (c) The spin-state composition is transferred to $|g_2\rangle$ near the nodes of $\Omega_c(x'-x)$ with probability given by $f(x'-x)$ (narrow red peaks). The width of $f(x'-x)$ is determined by the relative strength of the two light fields $\epsilon = \Omega_p/\Omega_c$ (see Eq. 3.2). (d) $f(x'-x)$ maps $|\psi(x)|^2$ onto population in $|g_2\rangle$, $n(x)$, which can be selectively measured via state-dependent imaging. By stepping through different positions x and measuring $n(x)$, we can reconstruct $|\psi(x)|^2$.

similar to observing molecular dynamics in biological samples. This chapter has been adapted from a published work [2], in which Sarthak Subhankar is the first author. To avoid overlap, I will be reporting the main results from the paper, while adding some supplementary content that did not make it into the paper due to length constraints.

3.1 General Principle of the Wave-function Density Microscope

The basic idea behind this wave-function density microscope is to transfer narrow slices of the wave-function density of atoms in every unit cell of the lattice into a different hyperfine state. By selectively measuring the population of atoms in that particular hyperfine state sequentially for each slice, we can determine the local probability density of the wave-function in the lattice. The "slicing" is realized using the dark state in a three-level system [27, 29, 30, 31, 32, 33]. The working principle of our wave-function microscope is illustrated in Fig. 3.1. Considering a three-level sysytem with a spatially varying control field $\Omega_c(x)$ and a weak homogeneous probe field Ω_p, there is a dark state decoupled from the excited state:

$$|E_0\rangle = \frac{1}{\sqrt{\Omega_c^2(x) + \Omega_p^2}}(\Omega_c(x)|g_1\rangle - \Omega_p|g_2\rangle). \tag{3.1}$$

Here, we use a standing wave control field, $\Omega_c(x) = \Omega_c \sin(kx)$, and a homogeneous probe field Ω_p with $\Omega_p \ll \Omega_c$, where $k = 2\pi/\lambda$ and λ is the wavelength of the light. Since $\Omega_p \ll \Omega_c$, the dark state composition is predominantly $|g_1\rangle$ away from the nodes, and $|g_2\rangle$ near the nodes where Ω_p becomes larger than $|\Omega_c(x)|$. The non-linear dependence of the Rabi frequencies gives a strong spatial dependence of the spin composition of the dark state and the high resolution of our wave-function microscope. The probability density of $|g_2\rangle$ as shown in Fig. 3.1 has narrow peaks near the nodes,

$$f(x) = \frac{\epsilon^2}{\epsilon^2 + \sin^2(kx)}, \tag{3.2}$$

where $\epsilon = \Omega_p/\Omega_c$. The full width at half maximum (FWHM) of $f(x)$, σ, provides a good metric for the resolution. For $\Omega_c \gg \Omega_p$ (small ϵ), σ is approximately $\epsilon\lambda/\pi$, which can be substantially less than the wavelength of the light and exceeding the diffraction limit. In our experiment, we first prepare atoms into state $|g_1\rangle$ and load them into the lattice (Fig. 3.1 (b)), then we adiabatically transfer a narrow slice of atoms into $|g_2\rangle$ with stimulated Raman adiabatic passage (STIRAP) (Fig. 3.1(c)). The population transferred to $|g_2\rangle$ at different location x, $n(x)$, is

$$n(x) = \int |\psi(x')|^2 f(x' - x)dx'. \tag{3.3}$$

By measuring the population in $|g_2\rangle$ and deconvolving this signal with the probing function $f(x)$, we can reconstruct $|\psi(x)|^2$.

In the measurement of $|\psi(x)|^2$, two competing timescales come into play: the STIRAP time and the relaxation time of the wave-function during the process of measurement. During the slicing process of the wave-function into $|g_2\rangle$, the lattice is turned off, and the lattice wave-function starts to relax. In order to accurately measure the shape of the wave-function, the STIRAP transfer process must be diabatic with respect to the motional degree of freedom of atoms, but still remain adiabatic with respect to the spin degree of freedom. For small ϵ, the shortest duration of the STIRAP is inversely proportional to the Rabi frequencies. For typical trapped atoms experiments, Rabi frequencies can be tens of megahertz. while the motional dynamics is on the order of tens of kilohertz. In this study, the STIRAP time is on the order of a few hundred nanoseconds which is substantially faster than the motional timescale of atoms, which is a few microseconds.

3.2 General Method

The details of the experimental apparatus and cooling sequence have been discussed in previous theses and publications [1, 15, 34, 35]. The three-level system used in this study is similar to the one discussed in chapter 2. The three-level system consists of the same three states, the two ground states, $|g_1\rangle = |^1S_0, F = 1/2, m_F = -1/2\rangle$ and $|g_2\rangle = |^1S_0, F = 1/2, m_F = 1/2\rangle$, and an excited state $|e\rangle = |^3P_1, F = 1/2, m_F = -1/2\rangle$ in ^{171}Yb. The levels are coupled by $\lambda = 556$ nm light using the same laser configuration as in chapter 2.

In this study, we load the atoms into the ground band of two different lattices. The first one is a Kronig-Penney (KP) type lattice of thin barriers, as described in [1] and chapter 2, which is expected to have a ground band wave-function density given by a cosine function, $|\psi(x)| \sim |\cos(kx)|$. The other lattice is a regular sinusoidal lattice based on the ac-Stark shift effect due to the off-resonant coupling between $|g_1\rangle$ and $|^3P_1, F = 3/2, m_F = -3/2\rangle$ lying outside of the three-level system that forms the dark state. This sinusoidal lattice is expected to have a Gaussian ground band wave-function. As in the chapter 2, the atoms are loaded into the lattices by adiabatically turning on the lattice.

Once our wave-function specimen is ready, we implement our microscope as follows. The lattice potential $V(x)$ is turned off by ramping down Ω_{c2} rapidly. Then, we ramp on Ω_p followed by ramping back on Ω_{c2} with a different phase, $\phi_{c2} = x\,(2\pi/\lambda)$ (where ϕ_{c2} is the phase of the RF drive to the AOM). The second ramp of Ω_{c2} flips the internal state of the atoms in the localized region near the nodes of the shifted $\Omega_c(x' - x) = \Omega_c \sin(k(x' - x))$ adiabatically from $|g_1\rangle$ to $|g_2\rangle$. The ramping profiles of these two beams are calculated

to preserve spin adiabaticity (see [33] and appendix in [2]), ensuring atoms follow the spatiotemporal dark state during the ramp. We then turn off all three beams simultaneously to preserve the dark state composition. The population in $|g_2\rangle$ is then measured with state-selective absorption imaging. The above process is repeated for different x in fine steps, allowing us to map out $|\psi(x)|^2$. The experimental sequences used to probe the wave-function density under different configurations are discussed in detail in the appendixes of [2]. There is a special technique that is worth noting here. Since the Fermi energy of our atomic cloud is $\sim 3\ E_R$, a small portion of atoms is loaded to the excited bands, which would complicate our microscope measurements. We resolve this issue by first loading atoms into a KP lattice with $\epsilon = 0.14$ ($\Omega_{c1} = 35\ \Gamma$, $\Omega_{c2} = 35\ \Gamma$, $\Omega_p = 10\ \Gamma$ and $\Delta = 4$ MHz) and hold for 5 ms before loading into the target lattice. Atoms in higher bands of the KP lattice have a significantly shorter lifetime than the ground band and are lost from the trap [13], effectively removing atoms in the higher bands.

Accurate microscopy of the wave-function density requires careful calibration of system. First, we need to have a good calibration of Rabi frequency dependence on laser power, which can be done with the technique discussed in the previous chapter 2.2.3. Second, we need to ensure the slicing into $|g_2\rangle$ is done spin-adiabatically while still being faster than the motional dynamics of atoms. This is accomplished with optimized STIRAP pulses discussed in Sec. 3.3.1. Third and most challenging, we need to preserve the $|g_2\rangle$ composition when turning off the "slicing" light and then measure the atom number in $|g_2\rangle$. Due to the adiabatic following of the dark state, if the turn off of the slicing lasers is not carefully designed to be diabatic, it will merely transfer the slice back into $|g_1\rangle$. This requires a rigorous synchronization of optical pulses and a proper state-selective measurement as

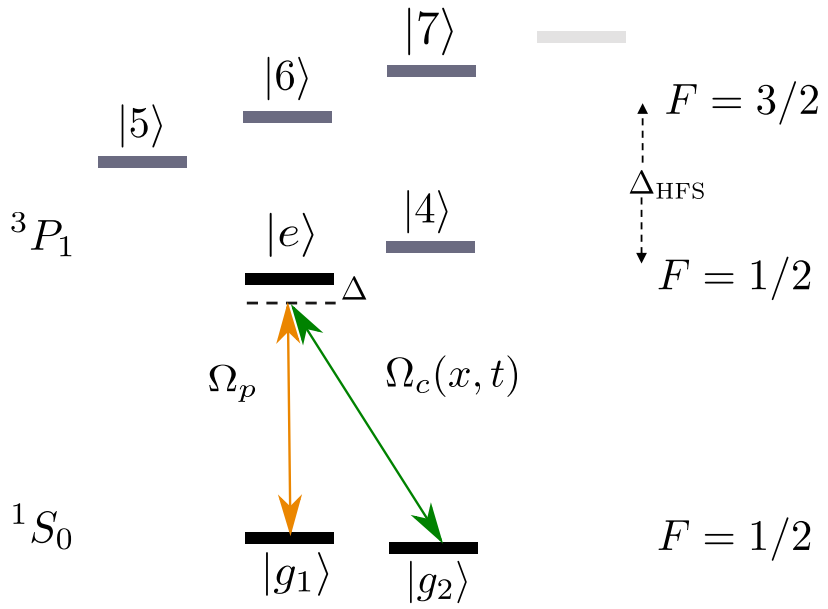

Figure 3.2: Level structure of the $^1S_0$ and $^3P_1$ manifolds in ^{171}Yb: Δ is the single-photon detuning, and $\Delta_{\mathrm{HFS}} \approx 6$ GHz is the $^3P_1$ hyperfine splitting.

detailed in Sec. 3.3.2 and Sec. 3.3.3.

3.3 Experimental Techniques

The preparation stage of Yb has been discussed in detail in [1, 35] and section 2.2. The level configuration and experiment geometry are the same as discussed in section 2.2. A larger magnetic field of 36 mT, instead of 12 mT used in the chapter 2, is used for better isolation of the three-level system.

3.3.1 Optimal Waveform for STIRAP and Hardware Control

As mentioned in the previous section, the STIRAP process, which transfers the atoms near the nodes of $|\Omega_c(x)|$ from $|g_1\rangle$ into $|g_2\rangle$, needs to be fast compared with the motional

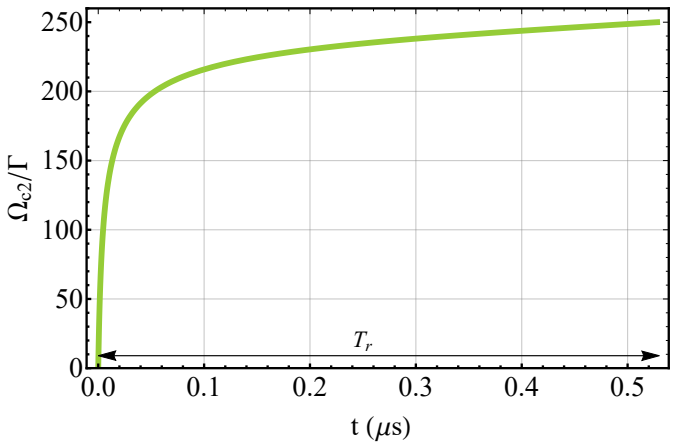

Figure 3.3: The optimal amplitude waveform for $\Omega_{c2}(t)$ for $\Omega_{c1} = 250\ \Gamma$, $\Omega_p = 25\ \Gamma$ calculated using Eq. 3.5. The initial rate of change of $\Omega_{c2}(t)$ is large due to the large value of Ω_{rms} from an imbalance between Ω_{c1} and Ω_{c2} in the beginning. The rate of change slows down notably as the imbalance vanishes.

dynamics of atoms while still be adiabatic with respect to the spin degree of freedom. For an ideal three-level system, the spin adiabatic criterion is $\Omega_{\text{rms}} \gg |\Omega_c\dot{\Omega}_p - \dot{\Omega}_c\Omega_p|/\Omega_{\text{rms}}^2$ [33, 36], where $\Omega_{\text{rms}} = \sqrt{\Omega_c^2 + \Omega_p^2}$ is the energy gap between the dark and bright eigen-states (see Sec. 2.1) and the right-hand side of the expression describes the diabatic coupling between them. We can define an adiabaticity parameter r:

$$\Omega_{\text{rms}} = r\frac{|\Omega_c\dot{\Omega}_p - \dot{\Omega}_c\Omega_p|}{\Omega_{\text{rms}}^2}. \tag{3.4}$$

A larger value of r implies a more adiabatic but slower transfer. In our configuration, $\Omega_c(x)$ and thus $\Omega_{\text{rms}}(x)$ are spatially varying. The adiabaticity requirement is hardest to satisfy near the nodes of $\Omega_c(x)$, where the energy gap between the dark and bright states is the smallest and the spin transfer is most substantial. Therefore, the equation is solved to give an optimal shape of $\Omega_{c2}(t)$ at the nodes of $\Omega_c(x)$ (Ω_{c1} and Ω_p are kept constant in time

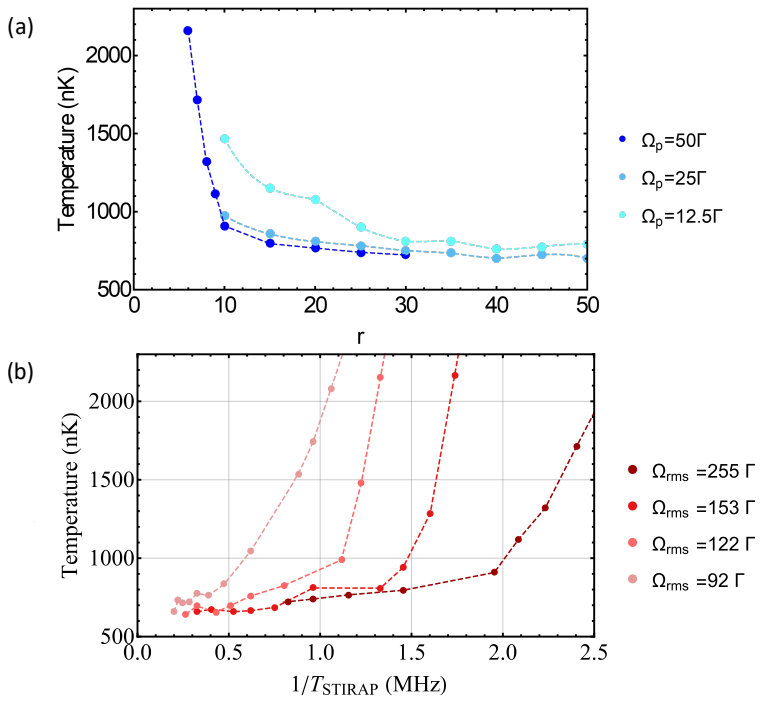

Figure 3.4: (a) The temperature of the atoms after ten complete STIRAP pulses for different values of r and Ω_p and (b) different values of Ω_{rms} and T_{STIRAP}.

here).

$$\Omega_{c2}(t) = \Omega_{c1} - \Omega_p \frac{(\frac{\Omega_{c1}}{\sqrt{\Omega_{c1}^2+\Omega_p^2}} - \frac{\Omega_p t}{r})}{\sqrt{1-(\frac{\Omega_{c1}}{\sqrt{\Omega_{c1}^2+\Omega_p^2}} - \frac{\Omega_p t}{r})^2}}. \tag{3.5}$$

The calculated $\Omega_{c2}(t)$ is shown in Fig. 3.3. The time needed for the ramp is

$$T_{\text{STIRAP}} = \frac{r}{\Omega_p}\frac{1}{\sqrt{1+4\epsilon^2}}. \tag{3.6}$$

For a typical value of $r = 15$, $\Omega_{c1} = 250\ \Gamma$, and $\Omega_p = 25\ \Gamma$, T_{STIRAP} is 0.52 μs, which is smaller than the relaxation time of lattice wave-function. As expected, a larger laser power gives a shorter ramp time for a chosen set of ϵ and r, enabling a more accurate temporal measurement of the wave-function density.

To experimentally determine the minimum value of r required to maintain adiabaticity, we measure the temperature of the atomic cloud after 10 consecutive STIRAP pulses under different values of r and Ω_p. If the adiabaticity is not well satisfied, there will be excitation to $|e\rangle$ causing light scattering, which increases the temperature of the atoms. The scan is performed with only one control beam Ω_{c2} and the probe bema Ω_p. In each pulse, $\Omega_{c2}(t)$ is ramped up from 0 to 250 Γ and ramped back down to 0 following the Eq. 3.5. The measured temperatures of the atomic cloud are shown in Fig. 3.4 (a). Beyond a certain value of r, the temperature becomes insensitive to the increase in r, implying that the STIRAP adiabatic criterion is well-satisfied. This occurs at about $r = 15$ for $\Omega_p = 50\ \Gamma, 25\ \Gamma$.

The value of T_{STIRAP} is also sensitive to the energy gap between the dark and bright states as suggested by Eq. 3.6 and 3.5. Therefore, using larger Rabi frequencies allows us to reduce T_{STIRAP} while maintaining adiabaticity. We study this effect by keeping the ratio of $\Omega_p/\Omega_{c2} = 0.2$ constant while Ω_{rms} is varied. As shown in Fig. 3.4 (b), with larger Ω_{rms}, faster adiabatic ramps can be achieved.

In order to generate the optimally shaped STIRAP pulses, we need to have fine, high-bandwidth control over the amplitude and phase of the light fields Ω_{c1}, Ω_{c2} and Ω_p. This exquisite control is provided by a home-built field-programmable-gate-array- (FPGA; Spartan 6) controlled direct-digital-synthesis- (DDS; AD9910) based RF signal generator designed and built by Carlos Bracamontes Palma. We used three such devices to drive three AOMs for the light fields separately. The phase coherence between the light fields is realized by sharing the same 10-MHz clock source and deriving the light fields from the same laser source. Each RF generator provides an 80-MHz signal with arbitrary amplitude

and phase, which is imprinted onto the light via the AOM. The desired waveform is loaded into the local RAM of the FPGA and is updated at the maximum amplitude update rate of 1/8ns and a phase update rate of 1/4ns. The maximum length of the waveform pulse is approximately 256 μs when updated every 8 ns. This home-built RF generator allows us to have a precise control on the Rabi frequencies, which is crucial for our microscope.

3.3.2 Pulse Alignment in Time Domain

During the probing stage, the population of atoms being transferred to $|g_2\rangle$ by STIRAP is proportional to $n(x) = \int |\psi(x')|^2 f(x' - x)dx'$, and thus contains the important information of $|\psi(x')|^2$ we are trying to measure. Therefore, the ramp-off stage of the laser beams is crucial to preserve the dark-state composition, and thus the information about $|\psi(x)|^2$, generated during the probing stage. Without taking care, simply turning off the coupling lasers would adiabatically undo the "slice" of population into $|g_2\rangle$. The way that we achieve this requirement is to ramp down the beams simultaneously while maintaining a fixed ratio between the Rabi frequencies $\Omega_{ci}(t)/\Omega_p(t)$, where $i = 1, 2$. Because the dark-state composition only depends on the ratio but not the absolute magnitudes of the Rabi frequencies, it is preserved during the ramp-off stage. For the typical values of Rabi frequencies ($\Omega_c = 500\ \Gamma$, $\Omega_p = 50\ \Gamma$), the relative delay between the light fields needs to be less than 20 ns to preserve the dark-state composition. The ramp-off also needs to be diabatic with respect to the mechanical degree of freedom of the wave-function, such that the evolution of the wave-function during the probing is negligible. These two requirements can be satisfied by turning off the laser beams with the RF drives to the

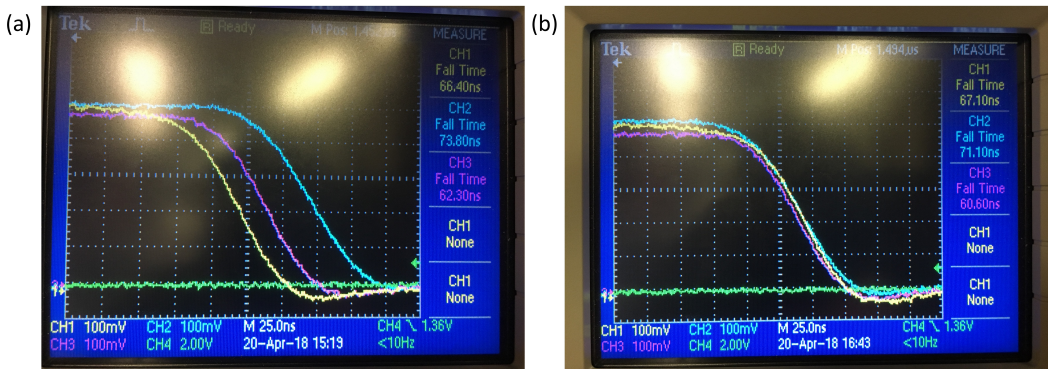

Figure 3.5: Photodiode signals showing the delays between light fields (a) Residual delays with our best physical alignment of the AOM crystals. The remnant delays are compensated by adjusting the cable length carrying the trigger signal giving synchronized pulses are shown in (b).

AOMs simultaneously in 100 ns.

Experimentally, simultaneous turn-off of the light fields between different AOMs is not guaranteed. One major reason is the varying distances between the spot where the laser hits the AOM crystal and the piezoelectric transducer driving the AOM crystal. The sound wave from the transducer travels at a finite speed of approximately 4000 m/s in a typical AOM, which means a difference of 1 mm can result in a delay in response of 250 ns. The finite sound speed also results in $\sim$ 100 ns optical rise time as the sound wave propagates through the laser beam in the crystal. With our best physical alignment of the AOM crystals, we can reduce the delays of the light fields to within 60 ns of each other as shown in Fig. 3.5. The remnant delays can be compensated by delaying the electrical signal to the AOM by adjusting the length of the BNC cable carrying the signal. The speed of light in BNC cable is about 2×10^8 m/s, which is around 2/3 of the speed of light in vacuum.

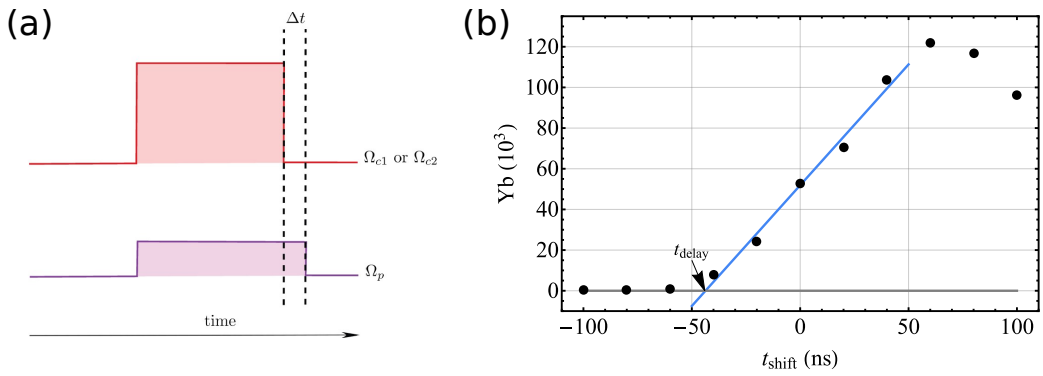

Figure 3.6: (a) Optical pulse sequence used to optimize the temporal overlap between the Ω_{ci} and Ω_p light fields. (b) The population of the atoms in the $|g_2\rangle$ state as a function of t_{shift} with $\Omega_{c1} = 250\ \Gamma$ and $\Omega_p = 50\ \Gamma$.

To measure the turn-off delay, we use a fast photodiode as shown in Fig. 3.5. However, the photodiodes used in the measurement may have significantly different optical distances from the atoms. Synchronized pulses measured at the photodiodes cannot guarantee zero delay of the light fields at the position of atoms. To confirm the light pulses are also synchronized at the position of atoms, we apply the method as shown in Fig. 3.6. Sweeping t_{shift} of the electrical signal, thereby changing $\Delta t = t_{\text{shift}} - t_{\text{delay}}$, we then measure the atom number in $|g_2\rangle$ using state-selective imaging. t_{shift} is varied at picosecond timescales using a delay-pulse generator (SRS DG535). When $\Delta t < 0$, the spin composition is mostly $|g_1\rangle$. But as $\Delta t \geq 0$, the spin composition starts to become $|g_2\rangle$ as shown in Fig. 3.6. By fitting a line to the data, we can extract the time t_{delay} from the x-intercept of the fitted line, when the spin composition starts to change from $|g_1\rangle$ to $|g_2\rangle$. The measured delays, which turn out to be consistent with the values measured using photodiodes, are then compensated via adjusting the BNC cable length.

Another approach to ensure that the dark state composition does not change is to

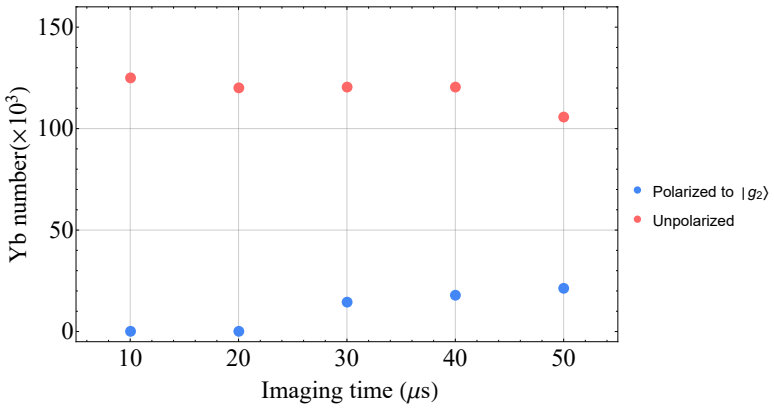

Figure 3.7: Dependence of the Yb number on imaging time under a maximum imaging power of 300 μW. The red points represent the measured number for an unpolarized ensemble, while the blue points represent the measured number of a $|g_1\rangle$-polarized ensemble.

turn off the light fields diabatically with respect to the spin-degree of freedom of the dark-state wave-function. As the Rabi frequencies of the light fields are in the range of hundreds of MHz, the turn-off time must be less than 10 ns. It is challenging to achieve such turn-off times with AOMs, but one could use electro-optical modulators (EOM) instead.

3.3.3 State Selective Imaging

In our experiment sequences, Yb atoms are measured by absorption imaging on the ${}^1S_0 \leftrightarrow {}^1P_1$ transition. State-selective imaging is achieved using the $|g_2\rangle \leftrightarrow |{}^1P_1, F = 3/2, m_F = 3/2\rangle$ closed transistion. The 399 nm imaging beam propagates along $\hat{x}$ with σ^+ polarization with respect to $\vec{B}$. The transistion between $|g_1\rangle$ and $|{}^1P_1, F = 3/2, m_F = 1/2\rangle$, which results in a false positive signal in the Yb number in $|g_2\rangle$, is suppressed by the large magnetic field of 36 mT along $\hat{x}$. The magentic field gives a 440-MHz Zeeman shift between $|{}^1P_1, F = 3/2, m_F = 1/2\rangle$ and $|{}^1P_1, F = 3/2, m_F = 3/2\rangle$, which is much larger than the

linewidth $\Gamma_{^1P_1} = 2\pi \times 27.9$ MHz. As a result, the off-resonant optical pumping effect from $|g_1\rangle$ into $|g_2\rangle$ via $|^1P_1, F = 3/2, m_F = 1/2\rangle$ should be suppressed by a factor over 3000.

Another parameter that we need to consider is the imaging time. As the atom in $|g_1\rangle$ will eventually be pumped into state $|g_2\rangle$ by the off-resonant imaging beam, the imaging time should not be too long. However, a longer imaging time is desirable to improve the signal-to-noise ratio of the image. To find an appropriate imaging time, we investigate the dependence of Yb number detected versus imaging time under an imaging beam resonant to $|g_2\rangle \leftrightarrow |^1P_1, F = 3/2, m_F = 3/2\rangle$ transition. The red dots in Fig. 3.7 show the detected number for an unpolarized Yb ensemble with an equal portion of atoms in $|g_1\rangle$ and $|g_2\rangle$. On the contrary, the blue dots show the detected Yb number for a $|g_1\rangle$-polarized ensemble of Yb, representing the magnitude of the false-positive signal. As the false-positive signal starts to appear at 20 μs as shown in Fig. 3.7 , an imaging time of 10 μs is chosen for the state-selective measurement.

3.4 Results

3.4.1 Calculation of Wave-function Density

In this study, we measure the ensemble-averaged probability density of atoms within the unit cells of an optical lattice. To verify the accuracy of our microscope, we calculate the ensemble-averaged wave-function density of atoms in different 1D optical lattices and the wave-funciton dynamics after a quench in the displacement or lattice depth. Consider

an Yb atom in a 1D optical lattice with a periodic potential $V(x)$.

$$\hat{H}\psi(x) = (-\frac{\hbar^2}{2m_{\mathrm{Yb}}}\frac{\partial^2}{\partial x^2} + V(x))\psi(x) = E\psi(x). \tag{3.7}$$

The eigen-function of atoms in an optical lattice is given by the Bloch ansatz as $\psi(x) = e^{iqx}u_{n,q}(x)$, where $u_{n,q}(x) = u_{n,q}(x + \lambda/2)$, $q \in [-k, k]$ is the quasi-momentum, and n is the band index. To solve for $u_{n,q}(x)$, one numerical approach is to Fourier expand $u_{n,q}(x)$ into plane waves.

$$u_{n,q}(x) = \sum_{m=-m_{\max}}^{m_{\max}} c_{n,q}^{(m)}\, e^{i2mkx}, \tag{3.8}$$

where $k = 2\pi/\lambda$. Putting Eq. 3.8 back into Eq. 3.7, we obtain

$$\sum_{m=-m_{\max}}^{m_{\max}} (\frac{\hbar^2}{2m_{\mathrm{Yb}}}(2mk+q)^2 + V(x))c_{n,q}^{(m)}e^{i(2mk+q)x} = E_{n,q}\sum_{m=-m_{\max}}^{m_{\max}} c_{n,q}^{(m)}\, e^{i(2mk+q)x}. \tag{3.9}$$

By inverse discrete Fourier transform, we can obtain a matrix form of the equation.

$$(\frac{\hbar^2}{2m_{\mathrm{Yb}}}(2mk+q)^2\delta_{m',m} + V_{m'm})c_{n,q}^{(m)} = E_{n,q}c_{n,q}^{(m')}, \tag{3.10}$$

where $V_{m'm} = \frac{1}{\lambda}\int_{-\lambda/2}^{\lambda/2} V(x)e^{-i2(m'-m)kx}dx = \frac{1}{2\pi}\int_{-\pi}^{\pi} V(y/k)e^{-i2(m'-m)y}dy$ is the $2(m'-m)$-th order Fourier coefficient. For a sinusoidal potential, $V(x) = V_0\sin^2(kx) = (V_0/2)(1 - \cos(2kx))$, so the potential $V_0\sin^2(kx)$ only couples plane waves with momentum differing by 0 or 2k. This leads to a matrix form of the equation.

$$\begin{pmatrix} \ddots & -\frac{V_0}{4} & 0 & 0 & 0 \\ -\frac{V_0}{4} & \frac{\hbar^2(q+2k)^2}{2m_{\mathrm{Yb}}} + \frac{V_0}{2} & -\frac{V_0}{4} & 0 & 0 \\ 0 & -\frac{V_0}{4} & \frac{\hbar^2(q)^2}{2m_{\mathrm{Yb}}} + \frac{V_0}{2} & -\frac{V_0}{4} & 0 \\ 0 & 0 & -\frac{V_0}{4} & \frac{\hbar^2(q-2k)^2}{2m_{\mathrm{Yb}}} + \frac{V_0}{2} & -\frac{V_0}{4} \\ 0 & 0 & 0 & -\frac{V_0}{4} & \ddots \end{pmatrix} \begin{pmatrix} \vdots \\ c_{n,q}^{(1)} \\ c_{n,q}^{(0)} \\ c_{n,q}^{(-1)} \\ \vdots \end{pmatrix} = E_{n,q} \begin{pmatrix} \vdots \\ c_{n,q}^{(1)} \\ c_{n,q}^{(0)} \\ c_{n,q}^{(-1)} \\ \vdots \end{pmatrix} . \tag{3.11}$$

In practice, one includes plane waves up to a maximum $m_{\max}$ depending on the accuracy that one wants to achieve. By numerical diagonalization for a given $V(x)$ as a function of the quasi-momentum q, the band energies as a function of q are given by the eigen-values, while the eigen-vectors provide the coefficients $c_{n,q}^{(m)}$ to the Fourier series of $u_{n,q}(x)$. The KP lattice possesses much higher order Fourier components due to its narrow subwavelength features, allowing it to couple plane waves with a much more significant difference in momentum. Typically, a value of $m_{\max} = 52$ is used for our calculation. Moreover, the Fermi energy of our atomic cloud $\sim 3\ E_R$, which is larger than the bandwidth of the ground band, so a uniform distribution of quasi-momentum is assumed in all the calculations in this study.

To calculate the wave-function dynamics after a quench, we need to solve the eigen-system of the Hamiltonian before and after the quench. Assuming the quench is diabatic, the wave-function in the initial Hamiltonian is projected onto the final Hamiltonian and the projection coefficients can be found by the dot product of the eigen-vectors $\hat{c}_{n',q'}^{\ \mathrm{final}\,\dagger} \cdot \hat{c}_{n,q}^{\ \mathrm{initial}}$.

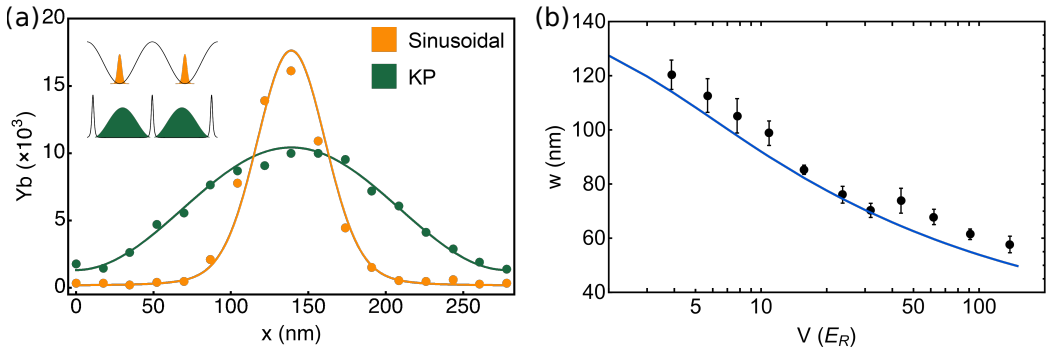

Figure 3.8: Measurements of the ground-state wave-function within the unit cell of an optical lattice with different shapes. (a) The orange points show $n(x)$ for atoms in a sinusoidal lattice measured with $\epsilon = 0.05$. The green points represent $n(x)$ in a Kronig-Penney lattice measured with $\epsilon = 0.1$. Number fluctuations between realizations result in number uncertainties of 5%. The solid lines are calculations using independently measured Rabi frequencies normalized to the same atom number. Inset: Schematic of different lattice potentials and corresponding $|\psi(x)|^2$. (b) FWHM w of $n(x)$ in a sinusoidal lattice as a function of the lattice depth. Black points show experimental data with $\epsilon = 0.05$, and the blue line is a calculation including the 800-ns measurement time. The error bars are 1 standard deviation from the Gaussian fits.

3.4.2 Measurements of the Ground State Wave-function

With the techniques mentioned in the previous section, we are able to use our wave-function microscope to investigate atoms in sinusoidal and KP lattices. Figure 3.8 (a) shows $n(x)$ measured in a 140 E_R sinusoidal lattice using a calculated resolution of 8.8 nm, along with $n(x)$ in a KP lattice with 50 E_R barriers using a calculated resolution of 17.6 nm. The different lattice potentials (sinusoidal vs boxlike KP) give rise to different functional forms of the wave-function in the lattice [inset of Fig. 3.8 (a)]. The expected $|\psi(x)|^2$ is Gaussian for a deep sinusoidal lattice and cosine for a KP lattice. The solid lines are the calculated $|\psi(x)|^2$ using independently measured Rabi frequencies (see Sec. 2.2.3) including both

the resolution due to finite slice width as well as wave-function expansion over the 800-ns measurement time. The wave-function is assumed to evolve freely without any confining potential during the 800-ns measurement in the calculation. Moreover, the Fermi energy of our atomic cloud is $\sim 3\ E_R$, which is larger than the bandwidth of the ground band, so a uniform distribution of quasi-momentum is assumed during the calculation for Fermionic ^{171}Yb.

The good agreement between the measured and calculated wave-function density suggests the STIRAP slicing of atoms into $|g_2\rangle$ and the state-selective imaging work as expected. Particularly, the good agreement on the wings of the Gaussian wave-function in the sinusoidal lattice implies that the optical pumping effect from $|g_1\rangle$ into $|g_2\rangle$ during the state-selective imaging process is negligible. In Fig. 3.8 (b), we show the FWHM w of the ground-band $|\psi|^2$ of the sinusoidal lattice as a function of the lattice depth. The measured values agree well with the calculated width represented by the blue curve. The remaining discrepancy may result from trap inhomogeneities due to the finite Rayleigh range of the Gaussian laser beams causing a reduction in the trap depth. Other sources of discrepancies may be the uncertainty of the Rabi frequencies, and the mechanical effects arising from the non-adiabatic potentials due to the spatially varying dark state [13, 14, 37].

3.4.3 Wave-function Dynamics

In addition to measuring the stationary wave-function density in the ground band of a lattice, the fast STIRAP slicing process allows for observing wave-function dynamics. At our maximum Rabi frequency of $\Omega_c = 2\pi \times 90$ MHz and $\epsilon = 0.05$, we can satisfy the

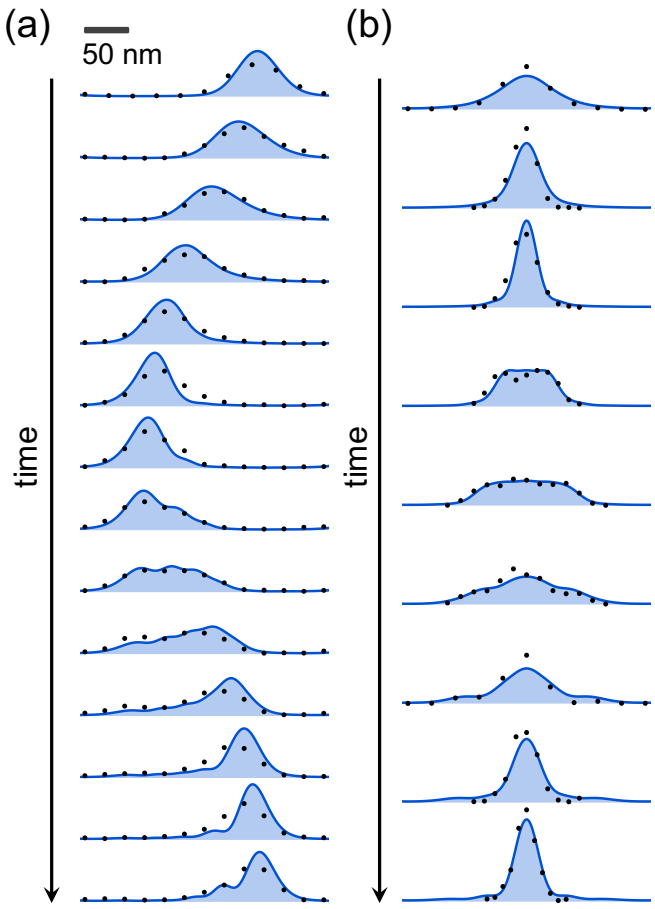

Figure 3.9: Wave-function dynamics within the unit cell of an optical lattice. Sloshing motion (a) and breathing motion (b) are excited in a $140E_R$-deep sinusoidal lattice by a sudden change in either the position or the depth of the lattice. $n(x)$ is plotted at different hold times [1 to 14 μs in steps of 1 μs for (a) and 1.5 to 9.5 μs in steps of 1 μs for (b)] after the quench. The points are experimental data with $\epsilon = 0.05$, and the blue curves represent calculations of $n(x)$ based on the independently measured lattice parameters. Typical number uncertainties are 5% due to shot-to-shot fluctuations.

adiabaticity condition for a STIRAP time of 500 ns, which is faster than the timescale of wave-function dynamics. Figure 3.9 shows the dynamics of the wave-function in a sinusoidal lattice after a sudden shift in the lattice position. The atoms are first adiabatically loaded into a 140 E_R lattice. Then, the lattice position is abruptly changed in 100 ns by 1/4 of the lattice spacing via the phase of the Ω_{c1} lattice beam, which excites a "sloshing" motion. We map out the evolution of the wave-function within the unit cell by holding the atoms in the shifted lattice for incremental periods of time before probing. The observed $|\psi(x)|^2$ agrees well with the calculations as shown in Fig. 3.9.

We also observe the "breathing" motion of the atoms after a sudden change in the lattice depth as shown in Fig. 3.9. The atoms are first adiabatically loaded into the ground band of a shallow lattice with a depth of 6 E_R. The depth of the lattice is then suddenly increased to 140 E_R, which excites a "breathing" motion of the atoms inside a unit cell. As time increases, we see that the $|\psi(x)|^2$ breathes at a frequency characterized by the band energies. At $t = 3.5\ \mu s$ and $t = 9.5\ \mu s$, $|\psi(x)|^2$ is focused to a calculated width $w_0 \simeq 26$ nm.

The good agreement between the measured wave-function dynamics with the calculations demonstrates the temporal resolution of our wave-function density microscope. On the other hand, the other crucial metric for a good microscope is its spatial resolution. We use the focused dynamic wave-function created during the "breathing" motion as the target of comparison to quantify the spatial resolution of our microscope.

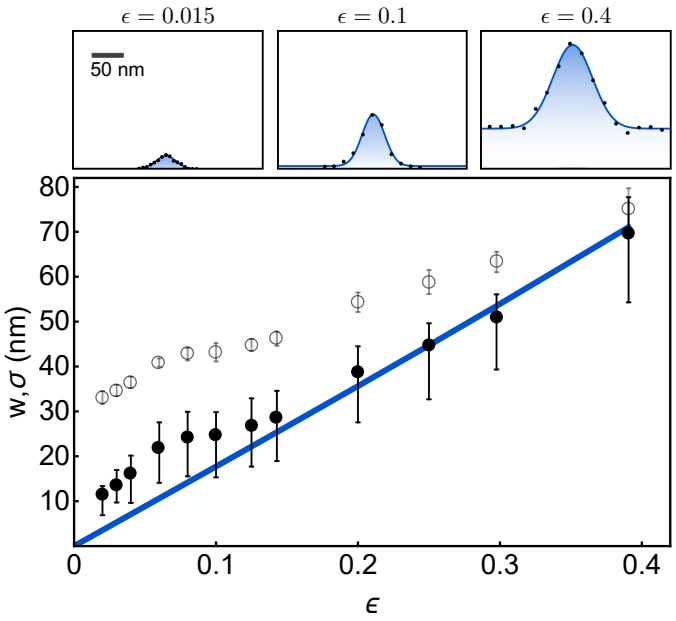

Figure 3.10: Spatial resolution of the microscope. We create a narrow wave-function $|\psi(x)|^2$ (FWHM 26 nm) by exciting the breathing motion of atoms in a deep sinusoidal lattice and measure $n(x)$ at the focus point [see Fig. 3.9] as a function of ϵ. The measured w from a Gaussian fit with a vertical offset to the $n(x)$ (see upper panel for typical wave-function measurements) is plotted against ϵ as the gray open circles, with the error bas showing 1 standard deviation from the fitting. These data are then deconvolved to find the intrinsic resolution σ and plotted as the black closed circles. The errors are dominated by the systematic uncertainties in the width of $|\psi(x)|^2$. The blue curve is the calculated width of $f(x)$ at different ϵ.

3.4.4 Spatial Resolution

We estimate the spatial resolution of our microscope by measuring the narrowest feature that we create with the breathing-mode excitation. This condition occurs at 9.5 μs where the calculated $|\psi(x)|^2$ has the narrowest calculated width $w_0 = 26.2^{+1.6}_{-0.6}$ nm under a Gaussian fit, where the uncertainty arises from the uncertainty in the Rabi-frequency calibrations used to determine the lattice depth. We measure $n(x)$ at this time with different resolutions by varying ϵ, as shown in Fig. 3.10. The measured width w of $n(x)$ is plotted as the open circles, which decrease and approach w_0 as ϵ decreases.

To determine the spatial resolution of our microscope, we extract the FWHM of $\sigma(\epsilon)$ of $f(x)$ for different ϵ by deconvolving $n(x)$ with the calculated wave-function $|\psi(x)|^2$. We use the independently measured values of Rabi frequencies to calculate the dynamics of the wave-function after a quench in lattice depth taking into account the 800-ns expansion time during the lattice-off time in probing. Then, we park at $t = 9.5\ \mu s$ and calculate $n(x, \epsilon) = \int |\psi(x', t = 9.5\ \mu s)|^2 f(x' - x, \epsilon)$ for various ϵ allowing us to obtain the relation between the expected width and the ϵ. By comparing the measured width and expected width, we extract the measured values of resolution σ for different ϵ, which are plotted as the black circles. The solid blue line is the theoretical FWHM width of $f(x)$.

The uncertainties of resolution may come from the uncertainty in the Rabi frequencies and fluctuations in the atom number. In addition to affecting the slicing function $f(x)$, the uncertainties in Rabi frequencies result in a different potential landscape, and therefore a different dynamical wave-function density $|\psi(x, t = 9.5\mu s)|^2$. To account for this effect, we calculate the dynamical wave-function $|\psi(x, t = 9.5\mu s)|^2$ for a possible range of Rabi

frequencies and find the Rabi frequencies that can account for the uncertainties in the measured width w. The upper bound of Ω_c is determined to be 530 Γ, while the lower bound is 480 Γ. We derive the dependence of the expected width against ϵ for the upper and lower bound values of Ω_c respectively, which are then used to determine the error bar on the resolution measurement.

The ultimate resolution is possibly limited by mechanical effects arising from the sharp potential associated with the dark state [1] and the mixing between the dark and bright states [1]. Moreover, as the slice width σ decreases, the total population in $|g_2\rangle$ also decreases, setting a practical limit on the usable resolution, as illustrated in the upper panel of Fig. 3.10. The smallest measured σ reaches $11.4^{+2.0}_{-4.4}$ nm, which could be improved with higher signal-to-noise ratio and Rabi frequencies.

Here, we have demonstrated superresolution imaging of atomic wave-function density with a spatial resolution of $\lambda/50$ and a temporal resolution of 500 ns. This imaging technique can be adapted to other systems as long as they host a three-system, including alkali atoms which are commonly used in other cold atom experiments. As demonstrated in Sec. 3.4.2, the subwavelength resolution of the microscope allows us to distinguish the different atomic wave-functions trapped in lattices with different subwavelength structures. A similar but different technique is demonstrated in [38]. Such a resolution will be critical in the study of optical lattices with lattice constants $\lambda/(2N)$ created through stroboscopic techniques [16]. In the next section, I will discuss the realization of a subwavelength-spaced optical lattice from the KP lattice. The wave-function microscope turns out to be a useful tool to study the properties of the stroboscopic lattice when excess heating during the stroboscopic process deteriorates the information in the momentum space. Particularly,

the temporal resolution allows us to measure the rapid dynamic evolution of the wave-functions in periodically driven Floquet systems [39].

Chapter 4: Realization of a Stroboscopic Optical Lattice with Subwavelength Spacing

Ultracold atoms trapped in periodic optical potentials provide wide-ranging opportunities to study many-body physics in highly controllable systems [40, 41]. In all cases, the characteristic single-particle energy scale is set by the recoil energy, $h^2/(8md^2)$, where m is the mass of the atom and d is the spatial period of the lattice. Although temperatures in such systems can be quite low, it is still challenging to reach temperatures well below the relevant many-body physics energy scales, which can be exceedingly small. Increasing the recoil energy can potentially increase both single-particle and manybody energy scales through tighter confinement, which may aid in creating systems well into the regime where many-body ground-state physics is observable. An inherent obstacle to smaller lattice spacing is the optical diffraction limit, which prevents lattice periodicities below $d = \lambda/2$, where λ is the wavelength of the light forming the lattice. In chapter 2, we have demonstrated the realization of the dark state potential with ultra-narrow barriers, one natural step is to stroboscopically shift the barriers to create an effective lattice with sub-wavelength confinement.

In this chapter, I discuss a way to realize a time-averaged optical lattice for cold atoms with a subwavelength spacing using the dark state potential [3] by stroboscopically shifting

the lattice. Because the dark state potential arises from the rapid spatial variation in the spin composition of the dark state near the nodes [1, 13, 14], the stroboscopic shifting needs to be both spin-adiabatic and motional diabatic. I will show that both requirements can be satisfied simultaneously by carefully designing the pulse shapes. To prove the validity of the time-averaging description, we make use of the nanoscale wave-function density microscope to observe the $\lambda/4$-periodicity of the ground state wave-function density of atoms in the stroboscopic lattice. We also investigate the Floquet-induced loss channel and the dependence of the lifetime of atoms on the Floquet frequency ω_F. We find Floquet heating to be a significant problem that must be considered for applications requiring long lifetimes. The discussion in this chapter is adapted from a published work [3].

4.1 General Principles and Methods

The basic idea of the stroboscopic scheme of realizing an effective potential with subwavelength lattice spacing of $\lambda/(2N)$, where N is an integer greater than 1, is illustrated in Fig. 4.1. We start from a progenitor lattice with a standard lattice spacing of $\lambda/2$, but narrow subwavelength barriers [1, 13, 14] as shown in Fig. 4.1 (a). To generate a $\lambda/(2N)$ lattice, this progenitor lattice is shifted by a distance of $\lambda/(2N)$ at a time step of T/N, where T is the period of a complete shifting cycle. Provided that T is much smaller than the typical timescale of the atomic motion, the atoms experience an effective time-averaged potential as shown in Fig. 4.1 (b). The process of time-averaging a dynamically applied potential cannot create an effective potential landscape with higher spatial Fourier components than the underlying progenitor lattice. This implies that in order to create

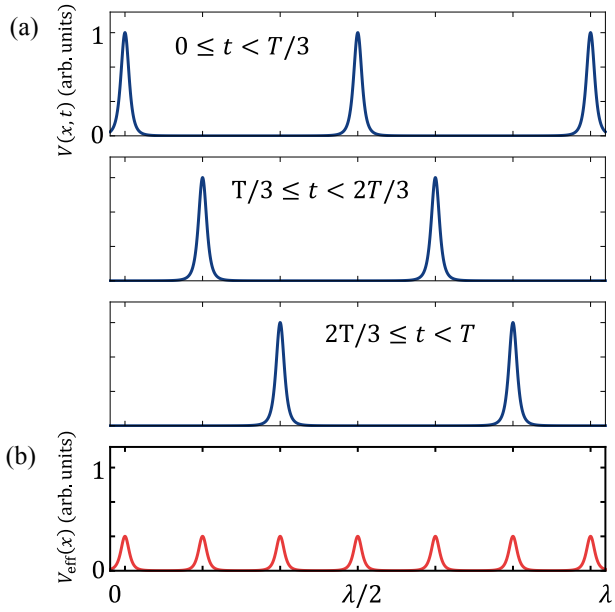

Figure 4.1: The stroboscopic approach to creating a time-averaged effective potential with a lattice spacing of $\lambda/6$ by dynamically pulsing KP potentials with $\lambda/2$ spacing.

landscapes with subwavelength periodicity, we need to start from a progenitor lattice that has subwavelength features.

In this work, we make use of the Kronig-Penney-like (KP-like) potential originated from the non-linear optical response associated with the dark state in the three-level Λ-system of ^{171}Yb [1, 13, 14]. This non-linear optical response generates the high-order spatial frequencies necessary for the stroboscopic technique, and results in the narrow barriers as shown in Fig. 4.1. The generation and properties of the KP lattice are discussed in detail in chapter 2. However, the spin adiabaticity required to maintain the dark state during the stroboscopic cycle imposes additional constraints.

Therefore, two timescales come into play in the realization of our stroboscopic lattice. First, the time scale of atomic motion sets a lower bound on the Floquet frequency ω_F,

beyond which the band structure becomes unstable and severe heating limits the lifetime. Second, the dark-state nature of the KP lattice sets an upper bound to ω_F. As the KP potential arises from a spatially varying dark state, switching on and off such a potential requires atoms to adiabatically follow the spatiotemporal dark state at all times. Because the potential is turned on and off many times in this time-averaging scheme, the spin-adiabaticity requirement needs to be very well satisfied during the whole stroboscopic process to suppress related losses. Therefore, in the next section, I will discuss how to ensure adiabatic following by carefully designing the pulse shape for the ramping and shifting process, implementing stimulated Raman adiabatic passage (STIRAP) in ^{171}Yb. In the following sections, my discussion and the parameters refer to the specific case of $N = 2$ which is experimentally demonstrated in our experiment [3].

4.1.1 Optimizing STIRAP pulse shape

In the stroboscopic realization of the effective potential, the progenitor potential needs to be shifted in steps periodically. The progenitor potential in our system consists of the KP potential, which arises from the rapid variation in the spin composition of the dark state in ^{171}Yb over a narrow spatial region. This rapid variation in spin composition originates from our configuration of control beams and probe beam as shown in Fig. 2.1 in the previous chapter. The control field $\Omega_c(x,t) = \Omega_{c1}e^{ikx} + \Omega_{c2}(t)e^{-i(kx+\phi(t))}$, where $k = 2\pi/\lambda$ and $\phi(t)$ is the relative phase difference between the two fields, which couples $|g_2\rangle$ and $|e\rangle$, is composed of two counterpropagating lattice beams. The maximum value of $\Omega_{c2}(t)$ is constrained to be equal to $\Omega_{c1} = \Omega_{c0}/2$, in which case it gives rise to a standing wave

$\Omega_{c0}e^{-i\phi(t)/2}\cos(kx+\phi(t)/2)$. We control the strength and the position of the KP potential using $\Omega_{c2}(t)$ and $\phi(t)$. A homogeneous probe field $\Omega_p e^{iky}$, coupling $|g_1\rangle$ and $|e\rangle$, travels perpendicular to the control beams. The control and probe fields couple the two ground states, $|g_1\rangle$ and $|g_2\rangle$, to give a dark state $|E_0\rangle = (1/\sqrt{(\Omega_c(x,t))^2+\Omega_p^2})(\Omega_c(x,t)|g_1\rangle - \Omega_p|g_2\rangle)$ Near the nodes of $\Omega_c(x,t)$, where $\Omega_p > \Omega_c(x,t)$, the dark state composition changes from mostly $|g_1\rangle$ to $|g_2\rangle$ at the nodes, giving rise to the narrow repulsive KP potential barriers.

To shift the KP potential, we need to displace the nodes of $\Omega_c(c,t)$ accordingly. However, we cannot simply keep the KP potential on and abruptly jump the phase of Ω_{c2}, as atoms in the dark state cannot follow this sudden change adiabatically and will be projected to the lossy bright states, resulting in significant heating. Therefore, we need to find a way that allows us to shift the KP lattice while keeping the atoms in the spatiotemporal dark state during the stroboscopic shifting process. To do so, we need to erase the spin texture before shifting the lattice, particularly the rapid spin-flip from $|g_1\rangle$ to $|g_2\rangle$ near the nodes of $\Omega_c(x)$, by carefully designed ramp shapes of the light fields. Three inequalities quantify the sufficiency requirements for the adiabaticity at single-photon resonance [36, 42].

$$|\frac{\partial\alpha(x,t)}{\partial t}| \ll \Omega_{\text{rms}}(x,t), \tag{4.1}$$

$$\int_{-T/2}^{T/2} |\frac{\partial}{\partial t}(\frac{\partial\alpha(x,t)/\partial t}{\Omega_{\text{rms}}(x,t)})|dt \ll 1, \tag{4.2}$$

$$\int_{-T/2}^{T/2} \frac{|\partial\alpha(x,t)/\partial t|^2}{\Omega_{\text{rms}}(x,t)}dt \ll 1, \tag{4.3}$$

where $\tan(\alpha(x,t)) = \Omega_p(t)/\Omega_c(x,t)$, $\Omega_{\text{rms}}(x,t) = \sqrt{|\Omega_p(t)|^2+|\Omega_c(x,t)|^2}$. Note the definition of α in this chapter is different from chapter 2. Equation 4.1 describes the local adiabatic

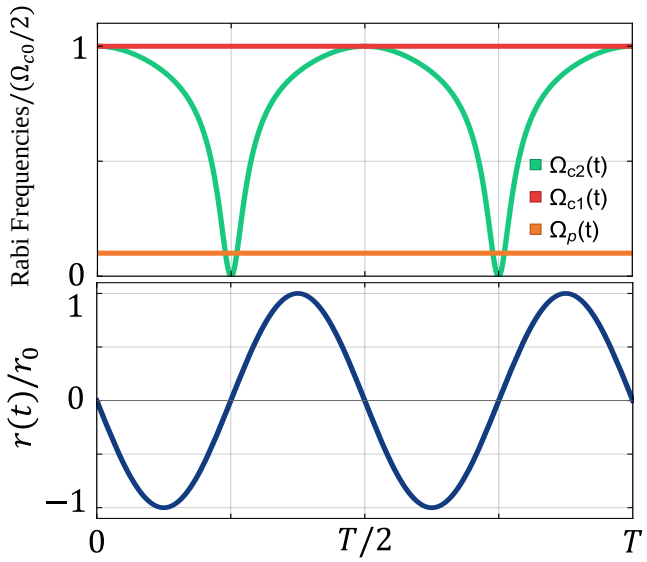

Figure 4.2: Rabi frequencies and $r(t)$ of control and probe beams during adiabatic ramps. $|r(t)|$ is smallest when the Ω_{c2} is closest to $\Omega_{c1} = \Omega_{c0}/2$, as $\Omega_{c2}(t)$ cancels Ω_{c1} at the nodes of $\Omega_c(x)$. Therefore, a small value of $|r(t)|$ and a more adiabatic ramp are needed due to a small energy gap between bright and dark states.

criterion stating that the energy gap between the dark and bright states [1], which is set by the $\Omega_{\text{rms}}(x,t)$, needs to be larger than the coupling between them ($|\partial\alpha(x,t)/\partial t|$). Equation 4.2 requires the ramping pulses to be smooth while both Eq. 4.2 and Eq. 4.3 set bounds on their rise time and fall time. We parameterize the inequalities with an adiabaticity parameter,

$$r(x,t) = \frac{\partial\alpha(x,t)/\partial t}{\Omega_{\text{rms}}(x,t)}, \tag{4.4}$$

$r(x,t)$ quantifies the local spin-adiabaticity. A smaller value of $r(x,t)$ implies a more spin adiabatic ramp of the light fields. Note the definition of r in this chapter is different from chapter 3.

To determine the pulse shapes of the light fields during the ramp, we consider the

spatial position, x_h, where the spin adiabaticity criterion is hardest to be satisfied, i.e., the nodes of $\Omega_c(x)$, since the energy gaps between the dark and bright states are the smallest at the nodes and the internal state of the atoms at the nodes must completely flip from $|g_1\rangle$ to $|g_2\rangle$. Specifying $r(x_h, t)$ allows us to determine the functional form of the pulse shapes of the light fields using the Eq. 4.1. To satisfy the three adiabaticity criteria Eq. 4.1-Eq. 4.3, $|r(x_h, t)|$ needs to be less than 1 and differentiable. Therefore, we consider a convenient analytic form of $r(t) = r(x_h, t)$ that has a continuous first derivative (Fig. 4.2 (b)) [42],

$$r(t) = -r_0 \sin(2\omega_F t), \tag{4.5}$$

where ω_F is the Floquet frequency of the $\lambda/4$ stroboscopic lattice, and $r_0 \ll 1$.

There are multiple ways to erase the spatial spin texture and give a spatially homogeneous spin composition [42, 43]. The particular scheme that we adopt is to turn off $\Omega_{c2}(t)$ adiabatically while keeping Ω_{c1} and Ω_p constant. As the imbalance between Ω_{c1} and $\Omega_{c2}(t)$ increases, the value of Ω_c at the nodes increases and becomes larger than Ω_p flipping the atom near the nodes from $|g_2\rangle$ to $|g_1\rangle$, resulting in a spatially homogeneous dark-state spin composition consisting mostly $|g_1\rangle$. Solving the local spin adiabaticity equation Eq. 4.1 with Eq. 4.5 at the nodes, we obtain the functional form of $\Omega_{c2}(t)$ that we use to create the stroboscopic lattice,

$$\Omega_{c2}(t) = \frac{\Omega_{c0}}{2} - \frac{\Omega_p \sin^2(\omega_F t)}{\sqrt{1 + 4\epsilon^2 - \sin^4(\omega_F t)}}, \tag{4.6}$$

where Floquet frequency $\omega_F = \Omega_p r_0 \sqrt{1 + 4\epsilon^2}$ and $\epsilon = \Omega_p / \Omega_{c0}$. The Rabi frequencies of the control and probe beams are shown in Fig. 4.2 (a).

While the function $r(t)$ we use to derive the functional form of $\Omega_{c2}(t)$ satisfies the local adiabaticity criterion Eq. 4.1, we also need to prove the other two requirements, Eq. 4.2 and Eq. 4.3, are satisfied as well. The stronger version of the second inequality Eq. 4.2 states:

$$|\frac{\partial}{\partial t}(\frac{\partial\alpha(x,t)/\partial t}{\Omega_{\text{rms}}(x,t)})|_{\max}\ t_r \ll 1, \tag{4.7}$$

where t_r is the period of $r(t)$. Putting in Eq. 4.5

$$\implies 2\pi r_0 \ll 1. \tag{4.8}$$

Meanwhile, the stronger version of the third inequality equation Eq. 4.3 states:

$$|\Omega_{\text{rms}}(x_h,t)r^2|_{\max}\ t_r \ll 1, \tag{4.9}$$

where $|\Omega_{\text{rms}(x_h,t)}|_{\max} = \Omega_p\sqrt{1+(\frac{1}{2\epsilon})^2}$ when $\Omega_{c2}(t)=0$ and $t_r = T/2 = \pi/\omega_F = \frac{\pi}{\Omega_p r_0\sqrt{1+4\epsilon^2}}$,

$$\implies \frac{\pi r_0}{2\epsilon} \ll 1. \tag{4.10}$$

In our experiment, we typically use $0.02 \le r_0 \le 0.2$ and $\epsilon = 0.1, 0.16$, so at least part of the parameter space that we work in should completely satisfy the spin adiabaticity criteria. Since the Floquet frequency ω_F is tied to the value of r_0 by $\omega_F = \Omega_p r_0\sqrt{1+4\epsilon^2}$, the spin adiabaticity criteria, in fact, sets an upper bound on the Floquet frequency window. However, it is important to note that the lifetime of the stroboscopic lattice is also affected

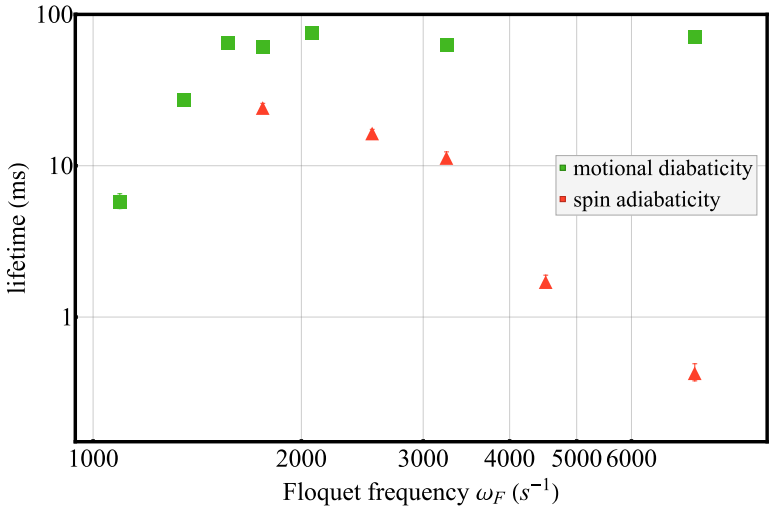

Figure 4.3: Lifetimes of atoms at different ω_F under different Rabi frequency configurations. Green squares: $\Omega_{c0} = 500\ \Gamma$ and $\Omega_p = 0$, where the spin degree of freedom is decoupled and the loss is due solely to the failure of motional diabaticity at low ω_F. Red triangles: $\Omega_{c1} = 0$, $\Omega_{c2} = 250\ \Gamma$, and $\Omega_p = 80\ \Gamma$, where the spatial potential is homogeneous and the loss is due solely to the failure of spin adiabaticity at high ω_F.

by the motional diabaticity requirement and momentum-dependent loss channels arising from the Floquet-induced coupling with higher excited bands.

To find the upper bound of Floquet frequency ω_F, we study the reduction in the fidelity of STIRAP as a function of ω_F for a spatially homogeneous dark state to remove the effect of motional diabaticity from this measurement. This is done by setting $\Omega_{c1} = 0$, $\Omega_p = 80\ \Gamma$, while $\Omega_{c2}(t)$ is pulsed to a maximum value of $250\ \Gamma$ following the expression 4.6. The reduction in STIRAP fidelity manifests as heating and loss due to the decreasing spin adiabaticity at larger ω_F (red triangles in Fig. 4.3). At high Floquet frequency ω_F, the spin adiabaticity criteria are not satisfied due to the larger value of r_0 used, setting an upper bound on the usable ω_F window.

In this section, I describe how to homogenize the spin composition by conscientiously

designing the ramping pulses according to the three spin adiabaticity criteria. Furthermore, we find the upper bound of the usable frequency window by studying STIRAP of a spatially uniform dark state. In the next section, I will discuss how to determine the lower bound of the usable frequency window set by the motional diabaticity requirement.

4.1.2 Study of motional diabaticity

The motion diabaticity sets the lower bound of the usable Floquet frequency range of the stroboscopic scheme. Beyond the limit, the atoms, instead of experiencing the time-averaged potential, can respond to the stroboscopic shifting of the progenitor lattice resulting in excitation to higher bands and heating. To study the effect of motional diabaticity, we optically pump the atoms into $|g_1\rangle$ and load them into a stroboscopically applied ac Stark shifted lattice, which does not involve the spin degree of freedom, unlike the KP lattice. This is done by setting $\Omega_p = 0$ with $\Omega_{c1} = 250\ \Gamma$, while $\Omega_{c2}(t)$ is pulsed to a maximum value of 250 Γ following the Eq. 4.6. At low ω_F, the atoms are affected by the turning on and off, and phase shifting of the sinusoidal ac Stark shift potential, which causes heating and loss (green squares in Fig. 4.3). As shown in figure 4.3, there is a frequency window within which both motional diabaticity and spin adiabaticity requirements are satisfied. In the next section, I will discuss the way to adiabatically load the Yb atoms into the stroboscopic lattice with lattice shifting and pulse shaping.

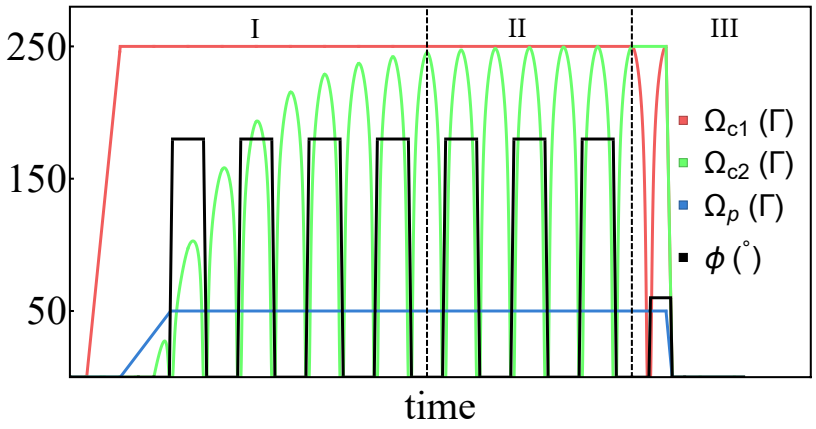

Figure 4.4: Rabi frequencies of different light fields and the relative phase ϕ between Ω_{c1} and Ω_{c2} during three stages. The Floquet period is not shown to scale; the minimum number of Floquet cycles during the ramp-on of Ω_{c2} is 40.

4.2 Experiment

We prepare the Yb cloud as described in previous chapters. Starting with the initial cloud of $\approx 2 \times 10^5$ atoms, we adiabatically turn on the KP barriers while performing stroboscopic shifting and pulsing to halve the lattice spacing and cancel the sinusoidal lattice on the background (Stage (I) in Fig. 4.4). We ramp on Ω_{c1} (red trace in Fig. 4.4) followed by Ω_p (blue trace in Fig. 4.4), transferring atoms into a spatially homogeneous dark state. Then we turn on $\Omega_{c2}(t)$ (green trace in Fig. 4.4) in 200 μs (minimum number of Floquet cycles used during the ramp ≈ 40), while maintaining the stroboscopic shifting and pulse shaping. The phase $\phi(t)$, which controls the position of the progenitor lattice, is only changed when the dark-state spin composition is spatially homogeneous, i.e. $\Omega_{c2}(t) = 0$. After $\Omega_{c2}(t)$ reaches $\Omega_{c1} = \Omega_{c0}/2$, we keep the stroboscopic lattice for a variable number of Floquet cycles (Stage (II) in Fig. 4.4). Time-averaging this lattice applied at two positions

results in an effective potential $V_{\text{eff}}(x)$ shown in Fig. 4.5 (b), which includes the effect of the pulse shapes, with an effective barrier height $\approx 7E_R$. The sinusoidal component of the potential averages to a spatially invariant offset. After that, we measure the average probability density of the atoms in the ground band of the stroboscopic lattice (Stage (III) in Fig. 4.4) using nano-resolution microscopy described in chapter 3 and [2].

4.3 Measurements and Results

After the loading stage, we measure the ensemble-averaged probability density $|\psi(x,t)|^2$ of atoms in the ground band of $V_{\text{eff}}(x)$ using our wave-function density microscope [2] with FWHM resolution of 25 nm. By comparing the measured wave-function density with the calculation, we confirm the subwavelength $\lambda/4$-spacing of the effective lattice and observe the micromotion of the wave-function density of atoms within the Floquet cycle. We also measure the momentum distribution of the atoms via absorption imaging after the time of flight (TOF), allowing us to study the momentum-dependent loss channels arising from the Floquet-induced coupling with higher excited bands.

4.3.1 Wave-function Density and Micromotion Dynamics

Figure 4.5 (c) shows $|\psi(x,t)|^2$ averaged over a Floquet period $T = 2.4\ \mu s$ ($\omega_F = 2\pi \times 410$ kHz) for atoms in $V_{\text{eff}}(x)$ with a $\lambda/4$ lattice spacing, and Fig. 4.5 (d) shows $|\psi(x,t)|^2$ at different times within a Floquet cycle. The Floquet frequency ω_F chosen falls in the frequency window in Fig. 4.3 that simultaneously satisfies both the spin adiabaticity and motional diabaticity requirements. By averaging the data over a Floquet period, we

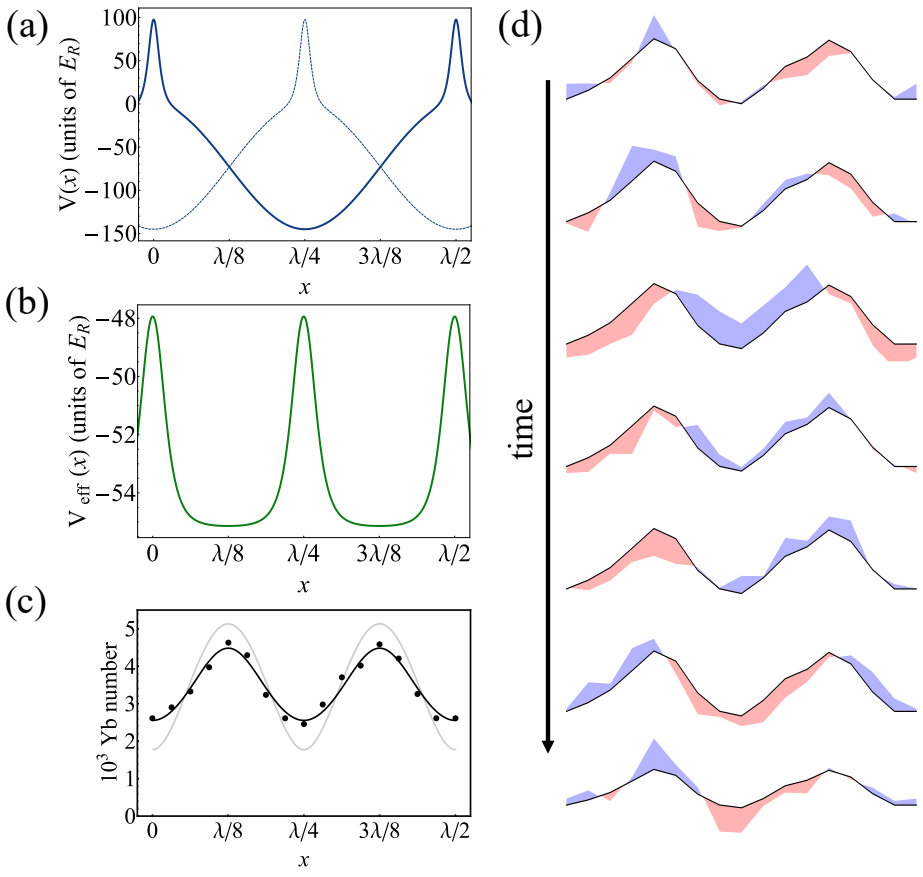

Figure 4.5: (a) The stroboscopically applied potential, shown here for $\Omega_c = 500$ Γ and $\Omega_p = 50$ Γ, is composed of KP barriers on top of a sinusoidal potential. The dashed line represents the potential shifted by $\lambda/4$. (b) The time-averaged effective potential $V_{\text{eff}}(x)$. (c) The black points are the measured $|\psi_{\text{avg}}(x)|^2$ of atoms in $V_{\text{eff}}(x)$. Number fluctuations between realizations result in number uncertainties of 5%. The black line is the calculation based on independently measured lattice parameters. The gray line is the calculated $|\psi_{\text{avg}}(x)|^2$ in the lattice without the relaxation during the measurement. (d) The micromotion dynamics at different times within a Floquet period. The blue (red) shaded areas represent regions in which $|\psi(x,t)|^2$ is higher (lower) than $|\psi_{\text{avg}}(x)|^2$, which is shown as a solid black line.

eliminate the effect of micromotion and obtain the averaged wave-function density $|\psi_{\text{avg}}(x)|^2$ [black dots in Fig. 4.5 (c)] in the ground band of the effective potential. The black curve represents the ground-band probability density calculated from the time-averaged potential, including the quasimomentum averaging, the effect of finite resolution of the microscope, and the relaxation of the wave-function during the measurement. The good agreement between the data and calculation shows that time-averaging is a good description of the effective potential. The calculated wave-function in the lattice without the relaxation during the measurement is plotted in gray. Moreover, we resolve the micromotion in real space within a Floquet period by comparing $|\psi(x,t)|^2$ with $|\psi_{\text{avg}}(x)|^2$ as shown in Fig. 4.5 (d). The blue (red) shaded areas represent regions in which $|\psi(x,t)|^2$ is higher (lower) than $|\psi_{\text{avg}}(x)|^2$. We observe that micromotion has the same time periodicity as the Floquet drive, as expected.

4.3.2 Momentum-dependent Loss Channel

A characteristic feature of a Bloch-Floquet band structure is the existence of avoided crossings at particular lattice momenta arising from coupling with high-lying states [44], which for large Floquet frequency are approximately plane waves with high momenta. We measure the momentum distribution of the atoms in $V_{\text{eff}}(x)$ at different ω_F by taking an absorption image after ramping down the lattice in 100 μs followed by a TOF of 3 ms. The atomic populations at high momenta in Fig. 4.6 indicate the mixing of low-momentum and high-momentum states due to Floquet coupling, which give rise to avoided crossings in our system. We use a Gaussian fit to determine the center momentum of the excited

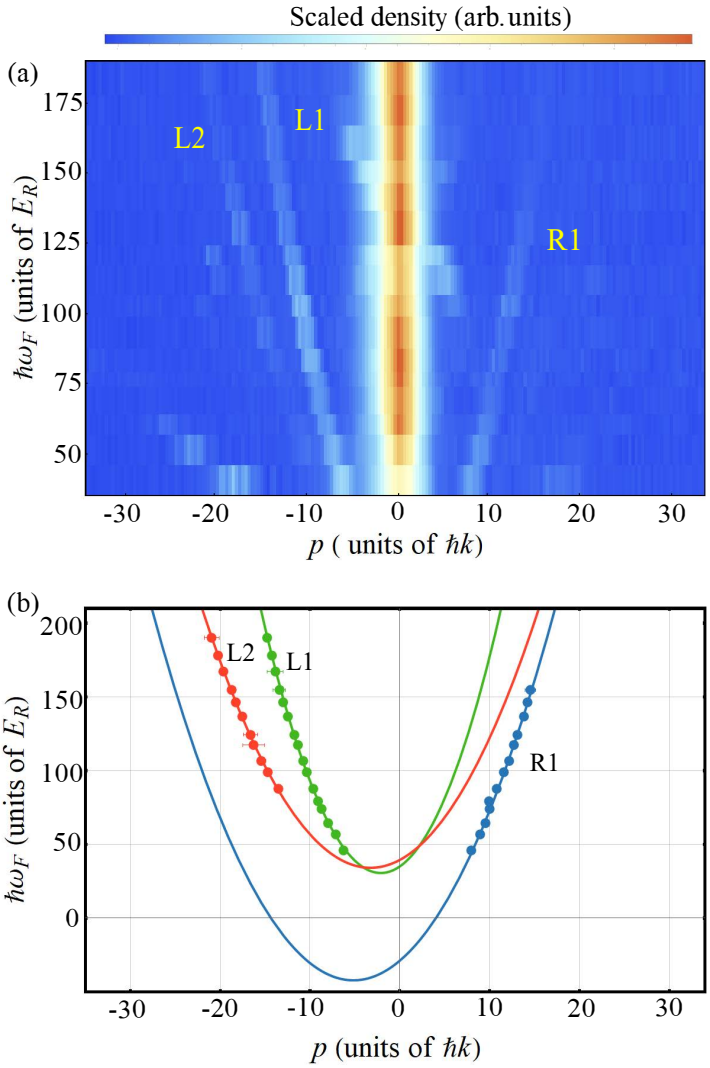

Figure 4.6: (a) Integrated TOF column density at different Floquet frequencies ω_F. The atomic populations at high momenta indicate the presence of avoided crossings. The widths of the populations at avoided crossings are primarily due to the physical dimensions of the atomic cloud. (b) The Floquet frequency ω_F is plotted versus the center momentum of the populations in (a) determined using Gaussian fits. Different series of avoided crossings are labeled and colored (L1: green, L2: red, R1: blue) and their fitted quadratic functions are drawn in solid lines respectively. The error bars are one standard deviation of the Gaussian fits.

populations with respect to the ground band. The Floquet frequency ω_F is plotted against the center momentum (Fig. 4.6) for the three most prominent peaks (L1: green, L2: red, R1: blue). To first order, the avoided crossings can be understood as arising from the intersection of Floquet-dressed high-lying bands, which are shifted in energy by integral multiples of ω_F, and the low-lying occupied bands of $V_{\text{eff}}(x)$, which are relatively flat. To determine the integral multiple of ω_F for the band coupling, we fit the peak positions with a quadratic function $\hbar\omega_F = (p-p_0)^2/N + \hbar\omega_0$, where p is the momentum, N is an integer, p_0 and ω_0 are fitting parameters, and the momentum and energy are in units of $\hbar k$ and E_R. For the L1 series, a good agreement with the data is found for $N = 1$, indicating this series is due to coupling between bands with an energy difference of $\hbar\omega_F$. For the L2 and R1 series, $N = 2$ gives the best fit, indicating second-order coupling between bands that differ in energy by $2\hbar\omega_F$. (The other visible peaks do not extend over a sufficient range to accurately determine their curvatures.) The fraction of atoms in the high-momentum states decreases at higher Floquet frequency, suggesting weaker coupling to higher bands. The asymmetry in the avoided crossings with respect to $p = 0$ is due to the fact that we are driving just the Ω_{c2} control beam, which gives rise to a vector gauge potential [42].

4.3.3 Lifetime study

In Sec. 4.1.1 and 4.1.2, I discuss the two limiting factors for the usability and lifetime of our stroboscopic lattice, motional diabaticity and spin adiabaticity, on the low and high frequency regime respectively. However, as suggested in Sec. 4.3.2, there are other factors contributing to the loss in a stroboscopic time-averaged lattice. We measure the

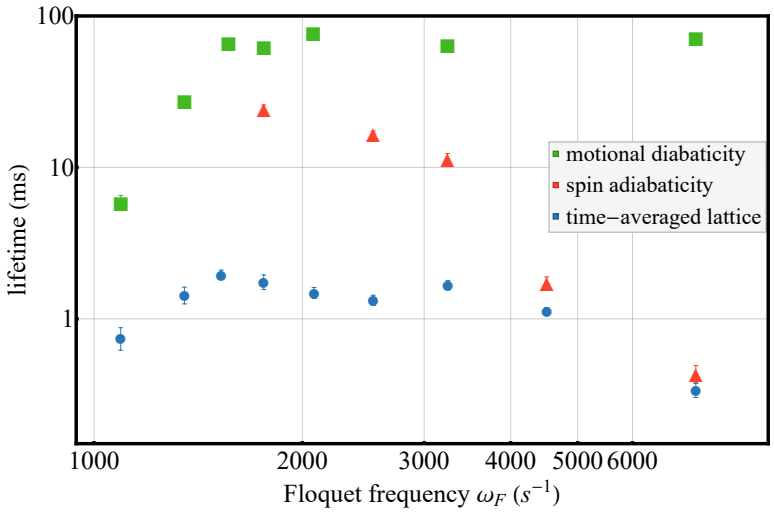

Figure 4.7: Lifetimes of atoms at different ω_F under different Rabi frequency configurations. Green squares: $\Omega_{c0} = 500\ \Gamma$ and $\Omega_p = 0$, where the spin degree of freedom is decoupled and the loss is due solely to failure of motional diabaticity at low ω_F. Red triangles: $\Omega_{c1} = 0$, $\Omega_{c2} = 250\ \Gamma$, and $\Omega_p = 80\ \Gamma$, where the spatial potential is homogeneous and the loss is due solely to the failure of spin adiabaticity at high ω_F. Blue circles: $\Omega_{c0} = 500\ \Gamma$ and $\Omega_p = 80\ \Gamma$, where we show the lifetimes of atoms in the $\lambda/4$-spaced lattice, $V_{\text{eff}}(x)$. The short lifetimes in the stroboscopic lattice are attributed to the Floquet-induced coupling and the off-resonant couplings to state outside of the three-level system.

frequency-dependent lifetime of atoms loaded into $V_{\mathrm{eff}(x)}$ for different ω_F (blue circles in Fig. 4.7). The reduction in spin adiabaticity accounts for the decrease in the lifetime of atoms in V at high ω_F, while the drop in lifetime at the low-frequency end can be explained by motional diabaticity. However, we observe comparatively short lifetimes even in the frequency window within which both requirements are satisfied. The short lifetimes observed in the stroboscopically applied KP lattices can be attributed to a few factors. First, couplings to the spatially and temporally dependent bright states reduce lifetimes in subwavelength-spaced lattices even for a perfect three-level system, through couplings with higher Floquet bands (as shown in Fig. 4.6) and off-resonant couplings with bright states [42]. In principle, these couplings can be reduced by using larger Rabi frequencies. However, lifetimes are also limited by the breakdown of the three-level approximation at large Rabi frequencies due to admixing of states outside the three-level system (Fig. 3.2). This manifests as a dynamically varying and spatially dependent two-photon detuning (arising from $\Omega_c(x,t)$), which reduces the fidelity of STIRAP [33]. This competing requirements prevent us from benefiting from larger Rabi frequencies.

4.4 Conclusion

The realization of a stroboscopic optical lattice with sub-wavelength spacing completes the story of three related studies: (1) A dark state potential with sub-wavelength width barriers. (2) A wavefunction density microscope making use of sub-wavelength spin localization. (3) Stroboscopic shifting the sub-wavelength barriers to give an effective potential with sub-wavelength lattice spacing. Further improvement of the $\lambda/4$-spaced

lattice would require compensation of the two-photon detunings or the identification of other atomic systems with a more favorable (isolated) three-level system [45]. The lattice demonstrated here is limited by the off-resonant coupling to $|^3P_1, F{=}3/2, m_F{=}{-}3/2\rangle$, which is only detuned by the hyperfine splitting from the three-level system being used. Better candidates may make use of isolated electronic levels, which are detuned by much larger optical separations. For example, in ^{174}Yb, the $(6s6p)\,^3P_0$ state and one of the states in the $(6s6p)\,^3P_2$ level could be used as the ground states, while one of the $(6s7s)\,^3S_1$ states could be used as the excited state, with an appropriate choice of polarization to select the three states. In a more isolated three-level system the main limitation would be the available laser power needed to meet the Rabi frequency requirements. In addition to longer lifetimes, higher Rabi frequencies would allow for lattices with smaller spacings [42]. Our work can be extended to 2D and additional dynamic control over the two-photon detuning—which makes subwavelength traps possible [45]—allows for construction of arbitrary time-averaged potential landscapes not limited by diffraction.

Chapter 5: Introduction for RbYb Tweezer Arrays Experiment

In the past decade, single neutral atoms trapped in optical lattices or tweezer arrays have emerged as a compelling and scalable platform for quantum simulation and quantum computing. Atomic physicists have been gathering various techniques in their toolbox for building a neutral atom-based quantum processor, including high-resolution imaging of single atoms [21, 46], single-atom addressing and control [47, 48, 49, 50, 51], and trapping atoms in re-configurable optical tweezer arrays and lattices [37, 52, 53, 54]. To utilize these neutral atoms for quantum simulation and quantum information, it is necessary to introduce controllable interactions between atoms. This can be achieved by coherently exciting the target atoms to a highly-excited Rydberg state, introducing a strong van der Waals interaction [55, 56, 57, 58, 59]. This van der Waals interaction can be switched on and off with lasers, avoiding the decoherence due to the crosstalk between qubits when multi-qubit action is unnecessary. In recent years, Rydberg-based neutral atom platforms have demonstrated the capability and potential for many applications, including quantum simulations of various many-body systems [60, 61, 62, 63, 64, 65, 66] and high-fidelity multi-qubit quantum gates [51, 67, 68, 69, 70, 71] illustrating its potential as a quantum computing platform.

On the other hand, the demonstrations of impressive capabilities and potential of

neutral atom platforms have relied on single atomic elements. A natural extension to multi-species systems should provide us with more degrees of freedom. A common trend of today's neutral atom array experiments is to increase the number of trapped atoms while maintaining high-fidelity control, long coherence time, and low crosstalk between atoms. For single-species platforms, there is an inherent challenge due to the scattered photons from nearby atoms during slow and destructive fluorescence-based imaging, making it difficult to achieve quantum measurement on selected atoms without causing decoherence in atoms nearby, which is a necessary component for quantum error-correction [72, 73] and controlled dissipation in general. One way to circumvent this problem is to use two-species of atoms; one acts as the data qubit and the other acts as the ancillary qubit. Similar ideas have been widely adopted in trapped ions systems [74, 75]. The information can be transferred from the data qubit to the ancillary qubit, and then the ancillary qubit can be measured with negligible decoherence effect on the data qubit due to a large separation of the resonant wavelengths. Such measurement is critical for the implementation of error-correction codes [73, 76, 77]. Moreover, the capability to independently load, trap, control, and image the two species of atoms may enable a continuous operation of an atomic array without any measurement downtime due to atom loading and initialization [78].

Furthermore, multi-species platforms [78, 79] provide an extra knob for tuning the interactions between atoms during the quantum simulation and computation [80]. In previous demonstrations, this interaction strength tunability comes from the separation dependence or the angular dependence of Rydberg interaction [65, 81], imposing geometrical constraints on the possible spatial configuration for quantum simulations. By selecting appropriate elements and Rydberg states, substantial differences in inter-and intra-species

interactions can be realized, providing flexibility to control the interaction between atoms for quantum simulations and enabling the realization of multi-control or multi-target gates with asymmetric Rydberg blockade [82]. We can also designate different physical qubits with different tasks according to their intrinsic properties to leverage the advantageous properties of each qubit type. This capability is potentially useful for building a hybrid quantum device [75, 83, 84].

In this chapter, due to the critical role of Rydberg interaction in our experiment, I will first discuss some properties of atoms in the Rydberg states. Since the properties of Rydberg atoms have been discussed at length in multiple review articles and books [55, 85, 86, 87], I shall only give a brief discussion of the properties relevant to our experiment. Then, I discuss Rydberg-Rydberg interaction and Rydberg blockade, which play a critical role in neutral atom quantum simulation and computation. Finally, I will motivate the building of a dual-species Rydberg tweezer arrays experiment with Rb and Yb.

5.1 Universal Properties of Rydberg Atoms

Rydberg states are the highly-excited states of atoms, typically with the principal quantum number $n > 25$. Because the electron in a Rydberg atom is excited to a weakly bound orbit far from the nucleus, Rydberg atoms exhibit some exaggerated properties compared to ground state atoms. Moreover, these properties have characteristic scalings with effective principal quantum number $n_{\text{eff}} = (n - \delta_{lj}(n))$, where $\delta_{lj}(n)$ [85] is the quantum defect for the state with the principal quantum number n, the orbital angular momentum l and the total angular momentum j. These scalings are insensitive to the atomic species and

are universal as the Rydberg electron is far away from the nucleus and inner electron shells. Table 5.1 summarizes the scaling of Rydberg state properties with the effective quantum number n_{eff}. It also includes the values for $5S_{1/2}$ ground state and $43S_{1/2}$ Rydberg state to illustrate the substantial differences in the various properties. In the following paragraphs, I will discuss those properties relevant to our experiment [55, 86].

Property	Scaling	Rb $5S_{1/2}$	Rb $43S_{1/2}$
Binding energy $E_{n_{\text{eff}}} = -\frac{R_M}{n_{\text{eff}}^2}$	n_{eff}^{-2}	4.18 eV	8.56 meV
Level spacing $E_{n_{\text{eff}}} - E_{n_{\text{eff}}+1}$	n_{eff}^{-3}	2.5 eV	417.36 μeV(100GHz)
Orbit radius $\langle r \rangle$	n_{eff}^{2}	5.632 a_B	2384.2 a_B
Polarizability α	n_{eff}^{7}	-79.4 mHz/(V/cm)^2	-17.7 MHz/(V/cm)^2
Lifetime (spontaneous decay) τ	n_{eff}^{3}	$5P_{3/2} - 5S_{1/2}$:26.2ns	42.3 μs at 300 K
Dipole moment $\langle 5P\|\|er\|\|nS \rangle$	$n_{\text{eff}}^{-1.5}$	4.227 ea_B	0.0103 ea_B
Dipole moment $\langle nP\|\|er\|\|nS \rangle$	n_{eff}^{2}	-	1069 ea_B
van der Waals coefficient C_6	n_{eff}^{11}	6.8×10^{-7} Hz(μm)^6	-2.3×10^9 Hz(μm)^6

Table 5.1: Summary of the scaling of Rydberg states with respect to the effective principal quantum number n_{eff}. The values for $5S_{1/2}$ ground state and $43S_{1/2}$ Rydberg state are given for comparison [86].

The first property of Rydberg states relevant to our experiment design is their energies. Because the Rydberg states are highly-excited, a direct single-photon excitation usually requires laser light in the deep UV region (Rb: 297 nm, Yb: 198 nm), which is difficult to produce and work with. Therefore, the excitation to Rydberg states is usually accomplished with a two-photon excitation scheme. For Rb, we use light at 420 nm ($(5S_{1/2}, F = 2) \leftrightarrow (6P_{3/2}, F = 3)$) and 1013 nm ($(6P_{3/2}, F = 3) \leftrightarrow nS, nD$). For Yb, we use light at 556 nm ($^1S_0 \leftrightarrow {}^3P_1$) and 308nm ($^3P_1 \leftrightarrow nS, nD$). Large single-photon detunings

are needed to suppress the spontaneous decay from the intermediate state (detail see Sec. 6.5). In addition, the small dipole matrix element for the intermediate-Rydberg transition ($\propto n_{\text{eff}}^{-1.5}$) implies that a sufficiently strong laser source is required to achieve a few cycles of Rabi oscillation within the lifetime of the Rydberg state. Recently, single-photon Rydberg excitation from a metastable clock state has been demonstrated in Sr [51], where the metastable clock state is defined as the qubit state. Since a large detuning to the intermediate state is not needed, the single-photon excitation can be much faster and has no intermediate state scattering. Similar scheme can be applied to Yb in our system.

In order to realize high-fidelity Rydberg excitation, the combined laser linewidth of the two-photon transition needs to be narrower than the natural linewidth of the Rydberg state, which is of the order of tens of kHz. However, the free-running linewidth of a typical laser source can be hundreds of kHz. Therefore, the Rydberg lasers need to be spectrally narrowed and locked to a highly stable reference. This is done by locking to an ultra-stable cavity with a cavity linewidth of a few tens of kHz via the Pound-Drever-Hall (PDH) [88, 89] technique, which allows transferring the mechanical stability of the cavity to the laser frequency and spectrally narrowing down the laser frequency below the cavity linewidth (for details see Sec. 6.5.1).

On the other hand, the combined effect of large dipole moments and small energy differences between neighboring levels of Rydberg atoms leads to a salient feature of Rydberg atoms, which is their high sensitivity to electric fields. For Rydberg states, the energy spacing between neighboring levels scales with n_{eff}^{-3}, and the dipole matrix elements between neighboring principal quantum numbers scale as n_{eff}^{2}. Therefore, the polarizability of the Rydberg state $|n, l, j, m_j\rangle$ scales as $\sim d^2/(E_n - E_{n+1}) \propto n_{\text{eff}}^{7}$. This implies that the

highly-excited Rydberg states are extremely sensitive to electric fields. For example, an electric field of 0.002 V/cm is sufficient to give a Stark shift comparable to the inverse lifetime of the Rydberg state $70S_{1/2}$. Therefore, stable and accurate control of the electric field is required if the Rydberg state is involved in the experiment. For this purpose, we have incorporated eight electrodes near the center of the science chamber, where the atoms are trapped, to provide a control on the local electric field experienced by the atoms (see Sec. 6.2.2 for details).

Finally, the most important property of Rydberg states is the strong van der Waals interaction between Rydberg atoms. Two atoms in the same Rydberg state $|r\rangle$ do not experience a resonant dipole-dipole interaction, since the expectation value of the electric dipole moment vanishes for atoms in their eigenstates. However, Rydberg atoms can interact significantly through a second-order effect mediated through nearby intermediate Rydberg states $|r'\rangle$ and $|r''\rangle$, which results in the van der Waals interaction between Rydberg pair state $|rr\rangle$, $V_{vdw} = C_6/R^6$. The van der Waals coefficient C_6 has a dependence $\propto \frac{\langle rr|\hat{d}_1\cdot\hat{d}_2|r'r''\rangle\langle r'r''|\hat{d}_1\cdot\hat{d}_2|rr\rangle}{\Delta}$, where Δ is the energy defect, $\Delta = E_{|r',r''\rangle} - E_{|rr\rangle}$. As the dipole matrix element scales as n_{eff}^2 and the energy defect scales as n_{eff}^{-3}, $C_6 \propto \frac{(n_{\text{eff}}^2 n_{\text{eff}}^2)^2}{n_{\text{eff}}^{-3}}$ scales as n_{eff}^{11}. For $|\text{Rb}, 50S_{1/2}\rangle$, C_6 is -15 GHz$(\mu m)^6$, corresponding to an interaction strength of 15 MHz at a separation of 10 μm. By applying small electric fields, the energy difference between the pair states $|rr\rangle$ and $|r'r''\rangle$ can be nullified, $\Delta = 0$, to reach the so called Forster resonance through the Stark effect [90, 91, 92]. At Forster resonance, the $|rr\rangle$ and $|r'r''\rangle$ become degenerate, and the atoms experience a dipole-dipole interaction. This capability to tune coherent interactions is one of the key components in quantum simulation.

Due to the strong and long-range interactions between Rydberg atoms, which can be

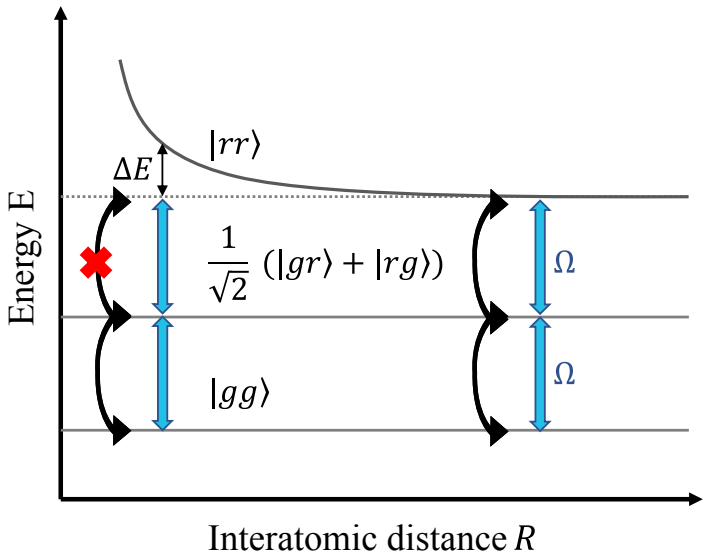

Figure 5.1: Illustration of Rydberg Blockade. When $R > R_b$, the interaction between the two atoms, ΔE, is negligible, so the transition to $|rr\rangle$ is allowed. However, as $R < R_b$, the interaction energy ΔE shifts the transition out of resonance, blocking to the excitation to $|rr\rangle$. This is called the Rydberg Blockade.

of a few tens of MHz at a separation of a few microns, excitation of multiple Rydberg atoms is prohibited within a certain volume of an atomic ensemble [56, 57, 58, 59]. To simplify the problem, we consider the situation of two atoms with a separation of R as shown in Fig. 5.1. A laser that is tuned on resonant with the transition from ground state $|g\rangle$ to the excited state $|r\rangle$ drives the two atoms from the ground states $|gg\rangle$ to a symmetric single-excited state $(|gr\rangle + |rg\rangle)/\sqrt{2}$. However, the transition from the singly excited state to the doubly excited state $|rr\rangle$ is shifted off-resonance by ΔE due to the mutual interaction between Rydberg atoms. If $\Delta E \gg \Omega$, the transition to the multi-excited state is suppressed. This energy condition can be translated into a condition on interatomic spacing, namely that the excitation is blockaded if $R < R_b$, where R_b is a critical distance called the Rydberg

blockade radius [55, 86]. This blockade radius sets the tweezer spacing in Rydberg tweezer experiments. Atoms trapped in two separate tweezers need to be closer than this distance to be Rydberg blockaded. This imposes a constraint on the beam waist of the tweezer. For example, the van der Waals coefficient C_6 of $|\mathrm{Rb}, 50S_{1/2}\rangle$ is -15 GHz $(\mu m)^6$, the blockade radius $R_b \approx (C_6/\Omega)^{1/6}$ is about 5 μm for $\Omega = 1$ MHz. Therefore, the diameter of the tweezer beam $d = \frac{2\lambda}{\pi \mathrm{NA}}$, where λ is the wavelength of the tweezer light and NA is the numerical aperture of the objective lens, needs to be smaller than 5 μm. For a tweezer wavelength of 850 nm, which we plan to use for trapping Rb atoms, the NA of the objective lens needs to be larger than 0.54 to give a focused beam diameter less than 1 μm.

The Rydberg blockade provides the fundamental mechanism to realize a high-fidelity two-qubit gate in neutral atom platforms in which the excitation of the first atom to a Rydberg state conditions the excitation of the other atom. There are various schemes to perform multi-qubit gates using Rydberg-mediated interaction. Details can be found in the references [55, 68, 68, 82, 93, 94].

5.2 Motivation for the Two-species Rydberg Tweezer platform

In recent years, neutral atom arrays have emerged as a competitive quantum architecture and have made significant experimental progress on increasing the qubit number [64, 66], coherence [69, 95], and high-fidelity state preparation and control [51, 67, 68]. There has been increasing interest in extending the neutral atom platform from single atomic species to multiple atomic species [78, 79], which may solve some inherent challenges in single-species systems, similar to the situations in trapped-ion systems [74, 75, 83, 96].

Moreover, multiple qubit modalities allow us to leverage the advantageous properties of each qubit type and provide the flexibility to control the interaction between atoms for quantum simulations.

5.2.1 Challenges in QND Measurments

Any quantum architecture is unavoidably subjected to decoherence and other quantum noise. Unlike the transistors in classical computers, qubits have a much smaller error margin and are fragile to any noise. As we push the limits on system sizes, the system becomes more susceptible to noise, and there is an increasing need for active error correction. One of the challenges in realizing quantum error correction on neutral atom platforms is to perform lossless quantum non-demolition (QND) measurement on a single atom with low crosstalk to nearby atoms [72]. State detection in atom arrays is typically done by imaging the fluorescence photons scattered from a cycling transition [72, 97, 98, 99]. Error-correction requires local state detection on selected qubit sites, which could be done by tightly focused imaging beams. However, the crosstalk to nearby atoms is still significant even with a tightly focused beam. To get a sense of the magnitude of the crosstalk, we can estimate the probability of the scattered photon being absorbed by a neighboring atom and the probability to be detected on the Electron-multiplying CCD (EMCCD). The resonant cross-section for photon absorption is $\sigma = \frac{3}{2\pi}\lambda^2$. Assuming an interatomic separation of $d = 5\mu$m, this results in an absorption probability by a nearby atom $p_{\text{crosstalk}} \approx \sigma/(4\pi d^2) \approx 0.001$ for Rb D2 transition (780 nm). For the probability of being detected by an EMCCD, assuming a NA of 0.5 for the photon collection lens and the combined efficiency for the optical

circuit and the EMCCD to be 0.5, which is extremely optimistic, $p_{\text{detect}} \approx 0.04$. Therefore, $p_{\text{crosstalk}}/p_{\text{detect}} \approx 2.5\%$, which implies for every photon detected by the EMCCD, there will be a chance of 2.5% for unwanted photon absorption by nearby atoms. In reality, the situation is even worse as tens of photons are typically needed for state detection [100, 101, 102] and the absolute collection efficiency is usually well below 0.5.

One solution to this crosstalk problem is to make use of dual-species architecture as suggested in [72, 79]. In our Rb Yb system, Yb atoms can be assigned as the processing qubits for computation and Rb atoms are used as the auxiliary qubits for state measurement. The quantum state in the Yb atom can be transferred to proximal Rb atoms by an inter-species Rydberg mediated gate. The information can then be read out via resonance fluorescence with Rb D2 transition. The large separation in resonance wavelength between Rb and Yb gives a strong suppression of the unwanted crosstalk.

In addition, a dual-species platform will allow for a continuous operation mode without any off-time as demonstrated in [79], where one atomic element was loaded into tweezers while maintaining the array of the other element without additional losses. Most neutral atom arrays experiments rely on fluorescence-based projective detection of qubit state, which requires scattering a large number of resonant photons. This fluorescence imaging is slow, in the order of a few tens of ms, and may lead to atom loss due to light-assisted collisions. The operations need to be halted during the imaging. Reloading from MOT may be needed to replenish the lost qubits. This downtime will increase significantly as the system size increases. With a dual-species platform, the quantum information in the processing qubit can be first mapped with a gate to proximal auxiliary qubits of another species which can be read out via fluorescence imaging. The substantial separation in

resonant wavelengths will suppress the loss of processing qubit. After the measurement, the quantum state of the processing qubit can be reset via a simple optical pumping. The computing sequence on the processing qubit can be restarted again and the lost auxiliary qubit can be replenished without affecting the operations on the processing qubits.

5.2.2 Multiqubit Gate

Apart from mitigating the crosstalk between neighboring qubits, the use of multi-species atoms provides new degrees of freedom, particularly the flexibility to control the intra- and inter-species interaction strength. This extra tuning knob is very useful in realizing multi-qubit gates that involve both multiple control qubits and target qubits simultaneously. Although a two-qubit gate is sufficient to give a universal gate set [76] that can perform any possible operation on a quantum computer, the use of a multi-qubit gate can provide significant speedups for quantum algorithms [103, 104] and quantum error correction [73, 76].

Many schemes have been proposed to achieve multi-qubit Rydberg gates with asymmetric blockade [105, 106, 107], in which there is a large separation of scales between different types of Rydberg interactions. This allows the control-control and target-target interaction to be substantially smaller than the control-target interaction. In most schemes, asymmetric blockade relies on the difference in interaction strength between strong dipole-dipole interaction and weaker van der Waals interaction. However, the use of dipole-dipole interaction may result in many-body resonances and antiblockade, resulting in a reduction in gate fidelity [108, 109].

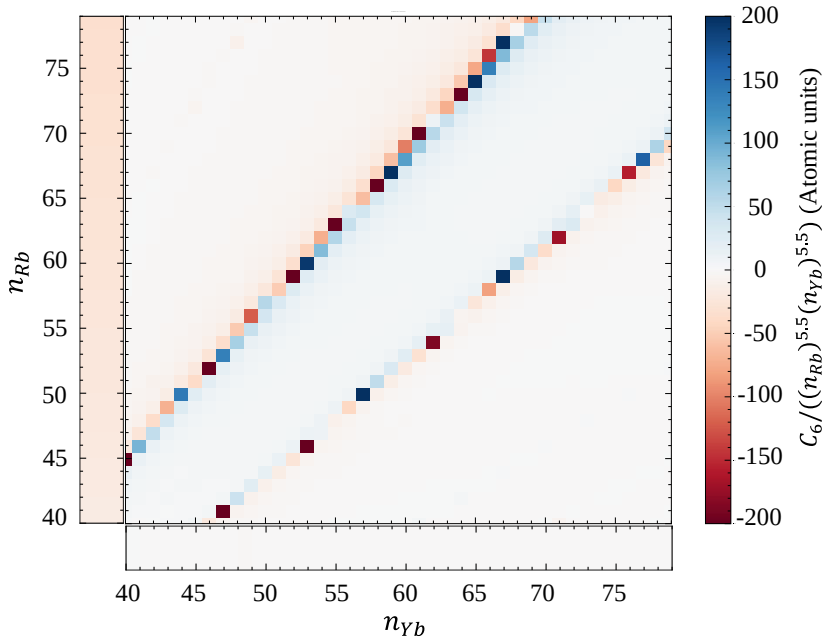

Figure 5.2: C_6 coefficients for pair state $|n_{\mathrm{Rb}}\,^2S_{1/2}, n_{\mathrm{Yb}}\,^1S_0\rangle$. The values are in atomic units and re-scaled by the principal quantum numbers, $n_{\mathrm{Rb}}^{5.5}\, n_{\mathrm{Yb}}^{5.5}$. The color bars along the y- and x-axis show the intraspecies C_6 coefficients for $|n_{\mathrm{Rb}}\,^2S_{1/2}, n_{\mathrm{Rb}}\,^2S_{1/2}\rangle$ and $|n_{\mathrm{Yb}}\,^1S_0, n_{\mathrm{Yb}}\,^1S_0\rangle$ rescaled by n_{Rb}^{11} and n_{Yb}^{11} respectively. There are combinations of n_{Rb} and n_{Yb} that give significantly larger inter-species interaction than the intra-species ones. For example, $|n_{\mathrm{Rb}} = 70, {}^2S_{1/2}\rangle$ and $|n_{\mathrm{Yb}} = 61, {}^1S_0\rangle$ give $C_6^{\mathrm{Rb-Yb}} = 34237.31$ GHz$(\mu\mathrm{m})^6$, $C_6^{\mathrm{Rb-Rb}} = -862.654$ GHz$(\mu\mathrm{m})^6$, and $C_6^{\mathrm{Yb-Yb}} = -3.84$ GHz$(\mu\mathrm{m})^6$.

In our Rb Yb system,asymmetric blockade can be achieved with the anomalously weak van der Waals interaction of the $^1S_0$ series Rydberg states of Yb, which can be orders of magnitude smaller than the interspecies van der Waals interaction between Rb and Yb with similar principal quanutm numbers (see Fig. 5.2). Therefore, we can use Rb and Yb to play the role of the control atom and the target atom. By selecting the right pair of Rydberg states for Rb and Yb, we can have a strong van der Waals interaction between the control and target atoms, but weak interaction between control atoms or between target

atoms.

Furthermore, in a hybrid architecture of multiple qubit modalities, different physical qubits are designated with different tasks according to their intrinsic properties to avoid crosstalk and leverage the advantageous properties of each qubit type. For example, in trapped ions experiments, multiple species of ions are often used such that one species acts as an auxiliary qubit to enable sympathetic cooling, state control, and measurement of another main ion species [74, 75, 83, 96]. In our Rb Yb system, the Fermionic isotope of Yb, ^{171}Yb, consists of electronic ground states with $J = 0$. The absence of electronic angular momentum and hyperfine coupling makes the ground state qubits, which are encoded in the $I = 1/2$ nuclear spin, much less sensitive to noises including magnetic field fluctuations, differential light shifts and Raman scattering [69, 110]. This makes ^{171}Yb an ideal qubit.

Chapter 6: Experimental Setup

In this chapter, I describe the experimental apparatus for the RbYb Rydberg arrays experiment. Since the platform is still under active construction, I will focus on the parts that have been completed. Additionally, I wish to share the knowledge and techniques that we have learned during the building of the apparatus in the hope that they may be helpful for future graduate students.

6.1 General Principle

Figure. 6.1 shows the render of our vacuum system from different viewing angles. Before going into the details of individual parts of our system, I shall give a general picture of the functions of different sections of the vacuum system, which consists of three main sections: (1) a Yb 2D-MOT; (2) a steel chamber connecting the Yb 2D-MOT and the glass cell; (3) a glass cell as the science chamber. The whole vacuum system sits on a translatable carrier system (Lintech), which allows us to slide the vacuum system out of the optical setup without affecting the alignment of the optics. In the Yb 2D-MOT, 399 nm laser beams resonant with $({}^1S_0 \leftrightarrow {}^1P_1)$ transition travel along the arms of the cross and are retro-reflected at the ends to capture hot Yb atoms from the oven as shown in Fig. 6.11 and 6.12. Hot Yb atoms are captured by the 2D-MOT and cooled in the transverse

direction to give a narrow tube of Yb atoms, as shown in Fig. 6.13 (b). The trapped Yb atoms in the 2D-MOT are pushed by the 399 nm laser beam (detail see Sec. 6.3.2) through a differential pumping tube in front of a gate valve. The Yb 2D-MOT section sits on a tilt platform (Newport TGN160) with a tilt angle range of $\pm 2.86°$, designed to compensate for the gravitational sag of the Yb atomic beam during its path to the glass cell. A NEG-ion pump (SAES NEXTorr D 100-5) is connected to the Yb 2D-MOT, where we have a typical pressure of $\sim 10^{-10}$ Torr with a Yb oven temperature of 400 °C. Yb atoms are pushed by the 399 nm push beam through the steel chamber to the glass cell, where they are first captured in a blue 3D-MOT (399 nm) and then cooled in a green 3D-MOT (556nm, $(^1S_0 \leftrightarrow {}^3P_1)$). The steel chamber in the middle contains eight Rb dispensers from SAES (RB/NF/4.8/17) as the source of Rb atoms (detail see Sec. 6.3.1). There is an ion pump (Gamma Vacuum 75S-CV) connected to the top of the chamber and a getter pump connected to the side of the chamber (SAES CapaciTorr Z100) allowing us to reach a pressure of 4×10^{-11} Torr measured at the ion pump when the dispenser is inactive. The Rb atoms in the steel chamber can diffuse to the glass cell, where they are trapped and cooled in a 3D-MOT. In the future, we plan to use light-induced atom desorption (LIAD) to desorb neutral Rb atoms from the glass cell surface to act as a source of Rb. However, this has not been implemented yet.

In the following sections, I shall discuss the details of the main components.

6.2 Vacuum System

6.2.1 Glass Cell and Chamber Design

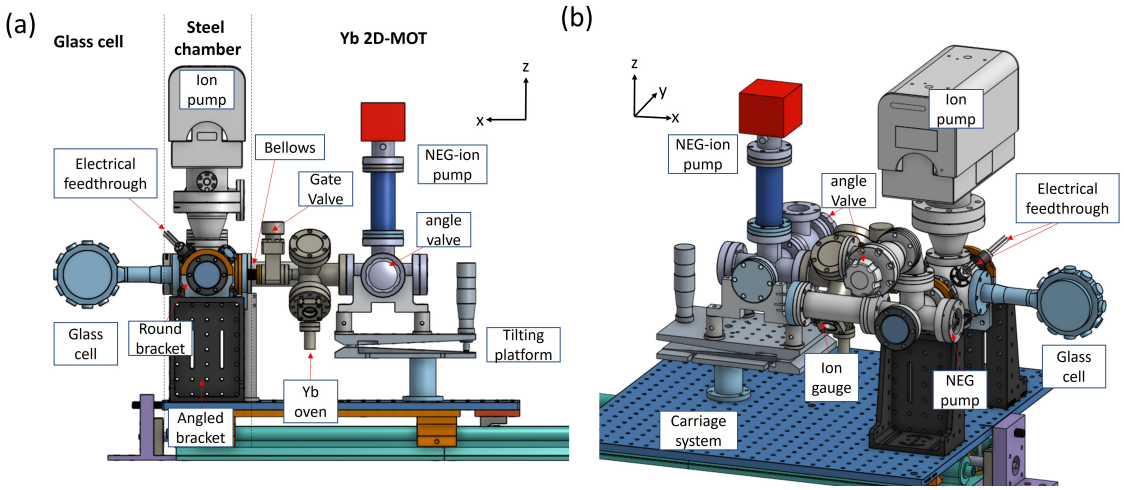

Figure 6.1: (a) Side-view of the vacuum system. Note the coordinate system here is referenced throughout the chapter. (b) Render of the system from another angle.

In this section, I focus on the two main parts of our vacuum system: the steel chamber connecting the Yb 2D-MOT, and the glass cell, which is our science chamber. The details of the Yb 2D-MOT are discussed in sec. 6.3.2.

In the center of our apparatus, there is a steel spherical cube vacuum chamber (Kimball Physics, MCF275-ExpCube-C6A8), which links the Yb 2D-MOT source to our science cell. This steel chamber is crucial for our vacuum setup. It is connected to vacuum pumps to maintain the vacuum in the glass cell, holds the Rb dispensers as our Rb source, and holds the mechanical support for our eight electrodes for electric field control inside the glass cell. Figure 6.2 shows a cross-section of the steal chamber. The spherical steel

chamber has six 2.75" ConFlat (CF) flanges on top, bottom, and equally spaced around the sides, and eight 1.33" CF flanges around the 2.75" CF flanges.

The 2.75" CF flange on the negative x-direction is connected to a CF flanged edge-welded bellows (Kurt J. Lesker, MEW0750251C1) via a zero-length reducer (Kurt J. Lesker, RF275X133). The bellows provides a physically flexible UHV connection to the Yb 2D-MOT source on a tilting platform. The top 2.75" CF flange is connected to a 75 L/s ion pump (Gamma Vacuum, 75S-CV) via a 4.50" to 2.75" CF conical reducer flange (Accu-Glass Products Inc., Part Number: 200561). The two 2.75" CF flanges on the sides are connected to two close couplers (Kimball Physics, MCF275-ClsCplr-C2-1400). The steel chamber is supported using a pair of right-angle brackets (Thorlabs, AP90RL) and 2.75" round brackets (Kimbal Physics, MCF275-ExtBrkt-R) (see Fig. 6.1) holding two 2.75 " double-sided flanges (Kimball Physics, MCF275-MtgFlg-C2) mounted to the close couplers. An additional stainless steel post is attached to the steel chamber via a washer plate to counteract rotating torque. One of the 2.75" double-sided flanges is connected to a 5-way cross (Kurt J. Lesker, C5-0275) to which we attach a NEG pump (CapaciTorr Z 100), an ion gauge (Kurt J. Lesker, G8130T), a viewport (Kurt J. Lesker, VPZL-275DUNM), and an angle valve (NorCal) for connecting to a turbopump.

Figure 6.2 shows a cross-sectional view of the steel chamber. Inside the steel chamber, we have the two sets of Rb dispensers fastened to the electrodes of two separate electrical feedthroughs, a copper feedthrough (Kurt J. Lesker, Part Number: EF0343052) and a molybdenum feedthrough (Kurt J. Lesker, Part Number: EF0344052). The two electrical feedthroughs are installed on two 1.33" CF flanges of the steel chamber. Additionally, we have a custom-made 304L stainless steel holder and clamp to grip the alumina rods and

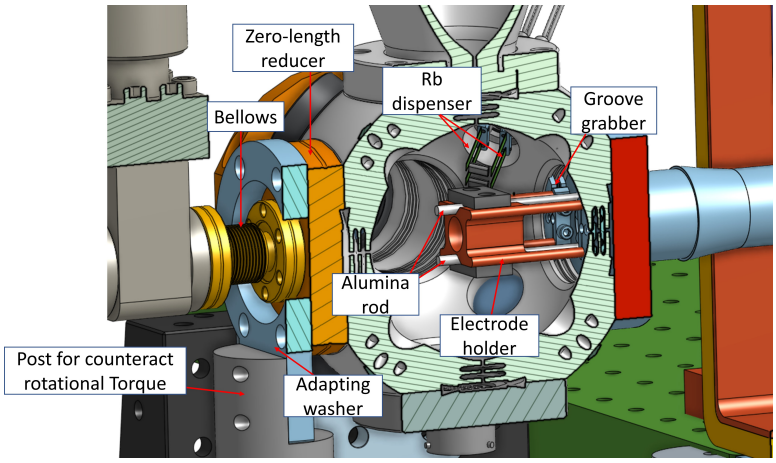

Figure 6.2: Cross-sectional view of the steel chamber

MACOR rings, which provide mechanical support for the electrodes inside the glass cell. The stainless steel holder is mounted on a pair of 2.75" groove grabbers (Kimball Physics, MCF275-GrvGrb-CB03). All the unused 1.33" CF flanges are attached with viewports (Kurt J. Lesker, VPZL-133DUNM)

An essential task for the steel chamber is to mount the dodecagonal glass cell (custom-made by Precision Glassblowing), where we trap Rb and Yb atoms and carry out experiments (see Fig. 6.1). There is a broad range of wavelengths, ranging from 308 nm to 1013nm, used in our experiment, and there is no anti-reflection (AR) coating that covers all the wavelengths. Instead, the glass cell surfaces have randomly distributed nano-scale, subwavelength structures providing excellent broadband AR properties that suppress reflections to 0.1 % or below, with wide angular acceptance and a high power damage threshold (TelAztec). This technique is called Random AR (RAR). These RAR-treated surfaces requires special attention, since they cannot be cleaned using standard cleaning techniques for thin-film AR coating. The RAR surfaces are most effectively cleaned by

rinsing with methanol or isopropyl alcohol according to the manual. Nevertheless, we have not carried out any cleaning by ourselves.

6.2.2 Electrodes and Electric Field Control

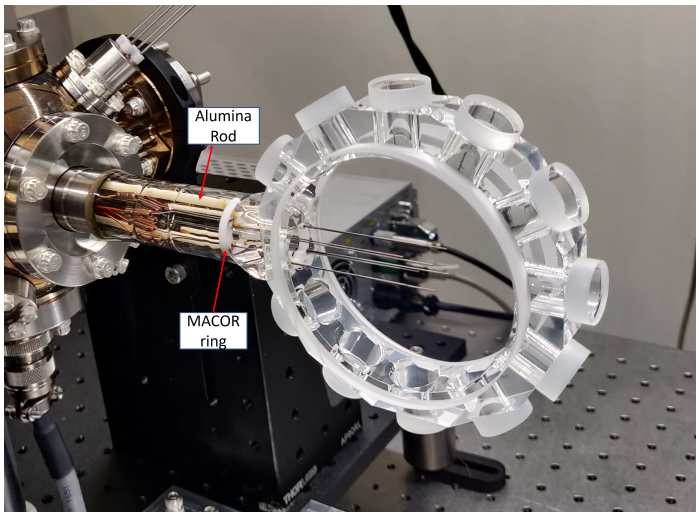

Figure 6.3: Image of the electrodes inside the glass cell. The dark brown "stains" at the contact points between the tungsten rods and the white MACOR ring are in fact UHV epoxy.

As mentioned in Sec. 5.1, the large dipole moments of Rydberg states make them extremely sensitive to electric fields. Therefore, it is necessary to have active control of the local electric field near the atoms. At the same time, we need to preserve optical access for the high-NA optics. For this purpose, we use four pairs of tungsten rods as electrodes and place them close to the center of the glass cell, where atoms are trapped. Each pair consists of two tungsten rods, with one of them being longer than the other by 1 cm. The ends of the shorter rods are aligned to the center of the glass cell. The tungsten rods have a diameter of 0.02" to preserve optical access for high-NA optics. However, the small diameter makes

the tungsten rods susceptible to cantilever deflection under gravity. For a 10 cm tungsten rod with a 5 mm diameter, the free end would bend down by 1.2 mm compared with the fixed end. As a result, the electrodes in our setup are supported by MACOR[1] rings the last of which is placed as close to the atom position as possible (see Fig. 6.3) to prevent cantilevering effect. The MACOR rings are epoxyed to alumina rods held by a custom-made stainless steel support (see Fig. 6.2). The tungsten rods are glued to the MACOR rings with UHV epoxy (Accu-Glass Products, Inc., Part number: 111785). The electrodes are connected to a 19-pin feedthrough (Accu-Glass Products, Inc. MiL-C-26482) with a 19-way UHV PEEK cable assembly (Accu-Glass Products, Inc., Part number: 110230). The Kapton on the wires was stripped and then connected to the tungsten rods with inline barrels (Kurt J. Lseker, Part Number: FTAIBC041). The pinout of the wiring is shown in Fig. 6.4. During the vacuum system assembly, the electrodes were checked to ensure no electrical short, but two pairs of electrodes were found to be shorted after baking and pumping. However, this problem has not been rectified to avoid breaking the vacuum.

Electrode	Voltage
1,3	$V_1 = -V_3$
2,4	$V_2 = -V_4$
5,6,7,8	$V_5 = V_6 = V_7 = V_8 = -2\Delta V$

Table 6.1: Grouping of electrodes and their voltage values.

We performed COMSOL simulations to determine the voltage that we need to apply to each electrode to create a locally homogeneous electric field assuming no stray field (see appendix A for details). The simulation was performed under the assumption there was no

[1]MACOR is a machinable insulating ceramic material.

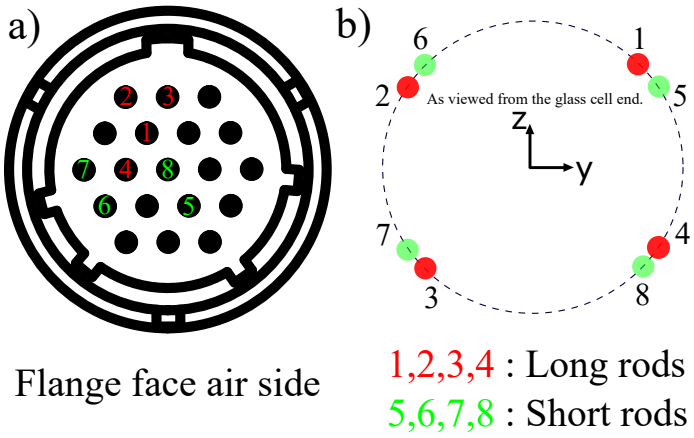

Figure 6.4: The layout of electrode wiring. The origin of the electric field simulation result is defined at the symmetric axis of the glass cell. The x-axis is pointing out of the page. The ends of the shorter tungsten rods set the x=0 plane.

short between electrodes. To generate a homogeneous field near the atoms, the electrodes are arranged into different groups (see table 6.2.2). For an electric field (E_x, E_y, E_z) at the origin (see Fig 6.4), the voltages required can be calculated using the equations below:

$$\begin{pmatrix} V_1 \\ V_2 \end{pmatrix} = \begin{pmatrix} 2E_L\cos(\theta_L) & 2E_L\cos(\theta_L+\pi/2) \\ 2E_L\sin(\theta_L) & 2E_L\sin(\theta_L+\pi/2) \end{pmatrix}^{-1} \cdot \begin{pmatrix} E_y \\ E_z \end{pmatrix} \tag{6.1}$$

and

$$\Delta V = \frac{E_x}{4(E_{Lx} - E_{Sx})} \tag{6.2}$$

where $E_L = 0.292$ (V/cm)/V, $\theta_L = 4.04$ rad, $E_{Lx} = -0.0617$ (V/cm)/V, and $E_{Sx} = 0.0617$ (V/cm)/V. The details of the calculation can be found in appendix A. For example, to get an electric field of ($E_x = 1$ V/cm, $E_y = 3$ V/cm, $E_z = 2$ V/cm), we need to apply ($V_1 = -V_3 = -5.88$ V, $V_2 = -V_4 = 1.87$ V, $V_5 = V_6 = V_7 = V_8 = -2\Delta V = 4.05$ V) to the

electrodes. Figure 6.5 shows the simulated electric field.

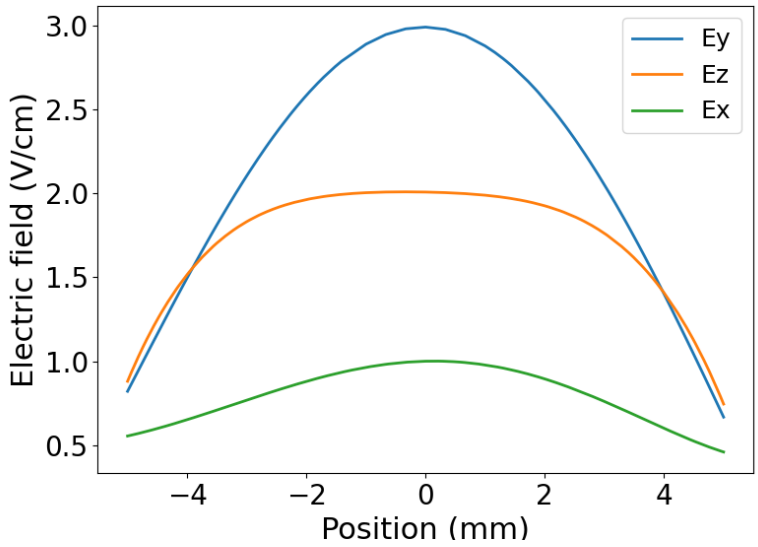

Figure 6.5: The simulated electric field near the origin for ($V_1 = -5.88$ V, $V2 = 1.87$ V, $V_3 = 5.88$ V, $V_4 = -1.87$ V, $V_5 = V_6 = V_7 = V_8 = 4.05$ V).

6.2.3 Magnetic Field Coils

The magnetic field control system in our setup consists of six independent coils. Figure 6.6 shows the geometry of the coils together with the coil housing. The coils are connected to separate current supply modules (KEPCO BOP20-20M: MOT and shim 2 coils, KEPCO BOP72-6M: shim 1 coils) for independent magnetic field control. All the coils are air-cooled to conserve optical access and reduce the technical overhead in water cooling. Air-cooled magnetic coils are possible with our setup, since the glass cell is much smaller in size compared with the typical steel science chambers in cold atom experiments enabling us to place the coils much closer to the atoms. Therefore, we can provide similar

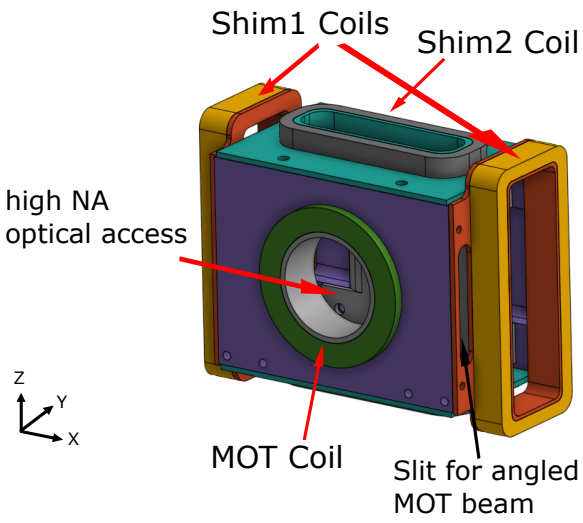

Figure 6.6: The geometry of the coils and the coil housings. There are six coils arranged symmetrically. The slits on the side allow us to send in MOT beams at a shallow angle for Rb and Yb 3D-MOT.

magnetic field gradients with a smaller amount of current. We expect that less than 1mT of magnetic field is needed for our future experiments, relieving the demand for water-cooled coils with large current supplies. According to calculations, a current of 15 A through the MOT coils (green in Fig. 6.6) results in around 10 W ohmic heating in the coil, which we empirically determine to be the limit of air cooling.

Coil	Layer	Turns/layer	Total turns	Field (mT/A)	FG ((mT/cm)/A))
MOT	5	9	45	0.28	0.22
Shim1	3	8	24	0.046	0.023
Shim2	4	5	20	0.033	0.020

Table 6.2: Design parameters of the coils. The magnetic field strength is calculated at the center of the glass cell. FG is the magnetic field gradient per current simulated at the center of the glass cell under the anti-Helmholtz configuration with opposite currents running in the pair of coils.

The coil housings are made of PEEK, which provides high strength and is thermal resistant. Kapton-insulated 12AWG copper wire was wound around the coil housing, and a thermally conductive but electrically insulating epoxy (Cotronics Corp. DURAPOT 865) was applied to every layer of wire to cement the wire in place. Due to difficulties in winding the rectangular coils, we designed a jig to hold the copper wire in place and maintain the tension during the winding. During the epoxy curing, a clamp was applied to ensure the copper wire was tightly packed. The design parameters of the coils are listed in Table 6.2.

The magnetic field simulation was performed using a free Mathematica add-on, Radia, from ESRF. The quadrupole magnetic field required during the MOT stage is generated by the two MOT coils in the anti-Helmoholtz configuration with currents running in opposite directions in the two coils. With a 20 A current in each coil, the MOT coils are expected to give a 4.4 mT/cm magnetic field gradient at the center of the glass cell, which should be sufficient for both Rb and Yb MOT. Since all the coils have separate current supplies, a nearly uniform field in an arbitrary direction can be produced by running currents in the MOT, shim1, and shim2 coil pairs in the Helmholtz configuration.

6.2.4 Vacuum Pump-down and Baking

During the construction of the vacuum system, several measures were taken to ensure that a high vacuum environment required for the tweezer arrays experiment could be achieved. In our vacuum system, various pieces of custom CNC-machined parts are placed inside the vacuum, including the electrode holder with clamps, the dispenser holders with clamps, alumina rods, and MACOR rings for electrode support. Since they may contain

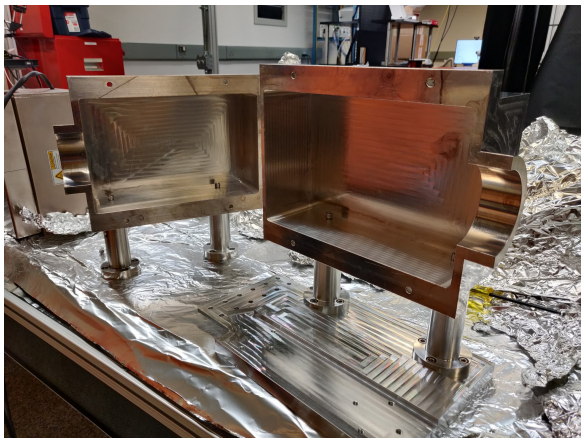

Figure 6.7: Photo of the protecting shell for the glass cell during baking.

residual grease and dirt from machining, the CNC-machined parts were sonicated with distilled water and detergent. After drying on clean UHV aluminum foil, they were sonicated with acetone and then isopropanol. In addition, the screws used in the in-vacuum parts, the tungsten electrodes, the tools and the jigs for assembly were cleaned using the same procedure. For larger parts that cannot be sonicated, they were rinsed with similar steps. One particular CNC-machined part that is worth mentioning here is the protecting shell for the glass cell (Fig. 6.7). As the surface of the glass cell is untouchable, we designed a "clamshell" protector that allows us to wrap heating tape around the body of the cell to bake the enclosed glass cell.

In addition, we prebaked the vacuum parts at 400 °C with a roughing turbopump for two weeks, including the steel chamber, the close couplers, the electrode holder with clamps, the dispenser holders with clamps, the tungsten electrodes, the alumina rods, the MACOR rings, the "clamshell" protector, the screws for in-vacuum components. After the prebake, the vacuum apparatus was assembled, and the glass cell was enclosed in the

protecting shell. The steel chamber and the protecting shell were wrapped with heating tape and insulated with aluminum foil. However, the Yb 2D-MOT section was not baked, and the gate valve at the connection was closed during the bake. The Yb 2D-MOT section was already under vacuum and had, in fact, been under vacuum for years, since it is the same 2D-MOT source used in the previous experiment. Multiple thermocouples were placed at different locations to ensure there were no large temperature gradients across the apparatus. In the first attempt, silicone rubber heating tape, which was claimed to work up to 232 °C, was used. However, the silicone heating tape started to smoke at around 100 °C. In the end, the silicone heating tape was replaced with fiberglass-insulated heating tape at the risk of contaminating the glass cell surface with fibers. The vacuum apparatus was baked at around 200 °C for more than two weeks.

After the first cooldown, it was found that the ion pump, which was salvaged from the RbYb mixture experiment, had a leakage current issue, resulting in significant differences in measured pressure under different ion pump voltages. The old ion pump was replaced with a new one, fixing the leakage current problem. We also took the chance to replace the CF tee connecting the old ion pump with a conical reducer flange to increase the conductance and add the 5-way cross that allows us to include a NEG pump and an ion gauge. After the second bake, a vacuum pressure around 4^{-11} Torr is attained.

6.3 Atomic Sources and Magneto-optical Traps

The accommodation of two different elements, Rb and Yb, poses complications in the design of the atomic sources and the magneto-optical traps for separately cooling and

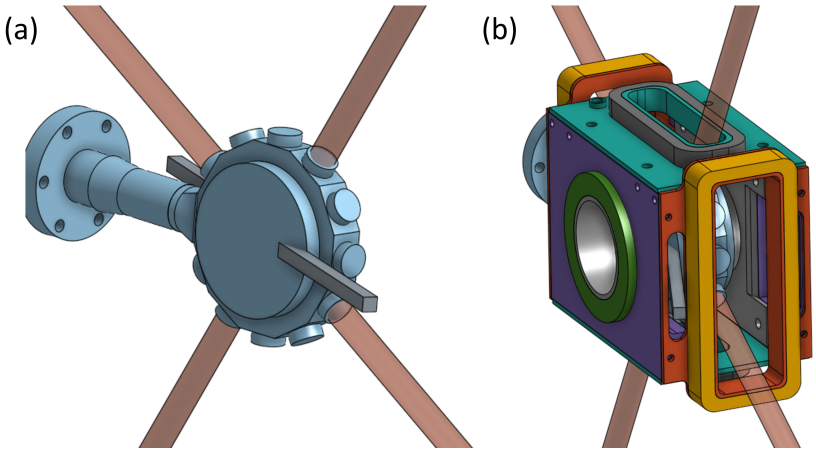

Figure 6.8: Render of the 3D-MOT beam geometry. (a) The two red circular beams are the standard retro-reflected MOT beams. The grey square beams represent the third MOT beam incident at a shallow angle. Different colors of MOT beams for Rb and Yb are combined before being sent to the glass cell to conserve optical access. (b) The third MOT beam passes through the slits on the coil housings.

trapping Rb and Yb. For Yb, we use a 2D-MOT source, which first captures thermal Yb atoms from an oven and then delivers a cold atomic beam to the 3D-MOT with a push beam, inherited from the previous RbYb mixture setup. For Rb, we use Rb dispensers to provide a thermal vapor of Rb. The slowly moving atoms in the tail of the Boltzmann distribution can be trapped directly by a 3D-MOT. The use of a dispenser source avoids the implementation of a Rb Zeeman slower or a Rb 2D-MOT. In order to load atoms into the optical tweezer, we need to first cool and trap atoms in a 3D-MOT. For the Rb 3D-MOT, the MOT beams consist of cooling light ($|5S_{1/2}, F = 2\rangle \leftrightarrow |5P_{3/2}, F = 3\rangle$ cycling transition) and repump light ($|5S_{1/2}, F = 1\rangle \leftrightarrow |5P_{3/2}, F = 2\rangle$ repump transition) (see Fig. 6.14), which are first combined and then split into three separate MOT arms by a fiber combiner/splitter (Canadian Instrumentation Research Ltd., now Evanescent Optics,

Inc.). Yb atoms sourced from the blue 2D-MOT (399nm ${}^1S_0 \leftrightarrow {}^1P_1$) are sent to a two-color, blue (399nm ${}^1S_0 \leftrightarrow {}^1P_1$) and green (556nm ${}^1S_0 \leftrightarrow {}^3P_1$), 3D-MOT with a blue push beam. The blue MOT ($\Gamma_{{}^1P_1} = 2\pi \times 29$ MHz) provides a large capture velocity during initial loading, while the green MOT ($\Gamma_{{}^3P_1} = 2\pi \times 183$ kHz) gives a substantially smaller Doppler temperature ($\sim 4\mu$K) at the end of the loading stage. To conserve optical access to the glass cell, different colors of MOT beams for Rb and Yb are combined before being sent to the glass cell, so the MOT beams use only two pairs of windows in total. Figure 6.8 shows the geometry of the three circularly polarized MOT beams. In the x-z plane, we have two standard retro-reflected MOT beams orthogonal to each other. However, the third MOT beam needs to be sent in through the slit of the MOT housing at a shadow angle (see Fig. 6.8), as the optical access is preserved for the high-NA objectives.

6.3.1 Rb Dispenser Source and 3D MOT

Our Rb source consists of two sets of commercially available Rb dispensers (SAES RB/NF/4.8/17) attached to a copper electrical feedthrough (Kurt J. Lesker, Part number: EFT0343052) and a Molybdenum electrical feedthrough (Kurt J. Lesker, Part number: EFT0344052) respectively. The Rb dispenser comprises a mixture of rubidium chromate with a reducing agent. When heated by running an electric current through it, the chromate reacts to relieve free Rb vapor, while the reducing agent also acts as a getter material to irreversibly absorb the chemically active gases created during the reduction reaction to prevent them from contaminating the chamber. Each set of Rb dispensers contains four dispensers, two of them are connected in series as a pair, and then two pairs are connected

in parallel, as shown in Fig. 6.9. The dispensers are fastened to the feedthrough electrodes with custom-made holders and clamps (304L stainless steel and electropolished) with 0-80 set screws.

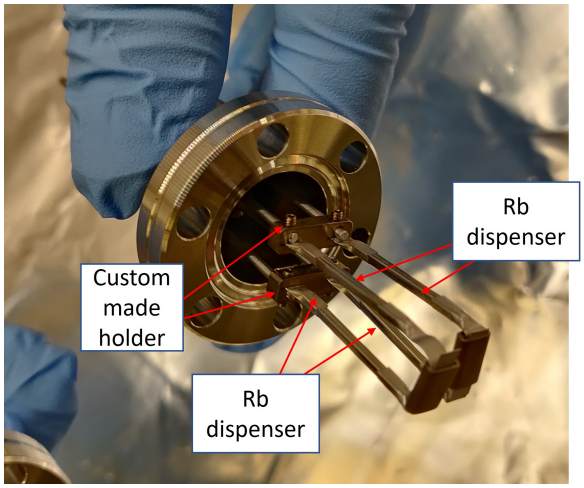

Figure 6.9: Photo of the electrical feedthrough with one set of Rb dispensers

The Rb dispensers need to be conditioned before use to release the physisorbed species weakly bound onto their surface. Therefore, we ran a current of 4A per set of dispensers, i.e. 2A per dispenser, for 12 hours and then increased the conditioning current to 6A per set for additional 6 hours during the low-temperature bake of the setup.

To control the evaporation rate of Rb vapor during the experiment, we designed a computer-controlled circuit board[2] to regulate the current flowing through the dispensers. The current from an external DC power supply flows through the dispensers and then through a MOSFET, followed by a sensing resistor on the board, and finally into ground. A micro-controller (Teensy 3.2) measures the current with the sensing resistor and sends a control voltage to the MOSFET gate to regulate the current. The circuit can vary the

[2]https://github.com/JQIamo/Rb-Dispenser-pwr-supp

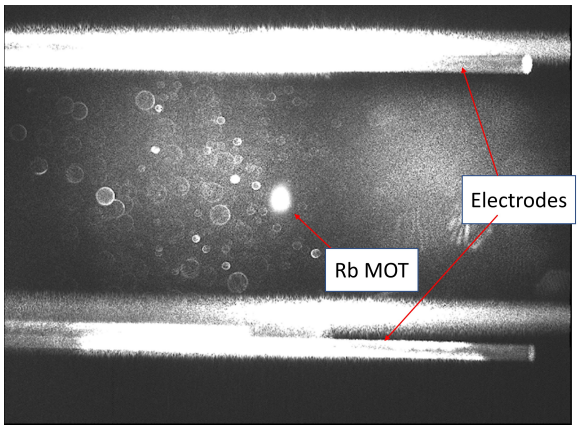

Figure 6.10: Photo of the Rb MOT. The glowing disks around the MOT are due to scattering by dust on the glass cell surfaces.

current in a timescale of 200 μs. Pull-down resistors are added as a safety measure to avoid current railing.

Figure 6.10 shows the image of the Rb MOT created, showing that the Rb dispensers and Rb 3D-MOT are working as expected. However, the optical setup for the Rb 3D-MOT beams is still under active upgrade, so the details of the optics and optimized loading parameters are not discussed in this thesis.

6.3.2 Yb 2D-MOT and 3D-MOT

The Yb 2D-MOT is inherited from our RbYb mixture setup, which worked robustly during my time in the Atlantic building. Therefore, we decided to transplant the Yb 2D-MOT part into our new RbYb Rydberg tweezers platform. Before taking apart the 2D-MOT from the old setup, we closed the gate valve to maintain the vacuum inside, and then moved it to our new laboratory in the basement and immediately powered the SAES pump attached (SAES NEXTorr D 100-5) up again. This allowed us to keep the vacuum

inside the 2D-MOT chamber at the level of 10^{-11} Torr before we installed it into our new setup.

The Yb 2D-MOT source vacuum chamber is shown in Fig. 6.11. The original design, which is based on a Lithium source [111], was made by Creston Herold and Varun Vaidya. Yang Wang and Sarthak Subhankar replaced the free-space MOT beams with a fiber-coupled cage mount system, which greatly improved the optical alignment stability. The detailed vacuum chamber design of the 2D-MOT can be found in Creston, and Varun's thesis [34, 35]. The 2D-MOT chamber is constructed from a custom-made 5-way 2.75" CF cross with two additional 1.33" CF flanges from Nor-Cal [34, 35]. There are washer plates [34] on the four 2.75" viewports allowing us to attach the cage mount system for the 2D-MOT beams. Yb is loaded into a half-nipple indicated in Fig. 6.11(a) and is typically heated to around 400 °C to give a thermal atomic flux. Even though the Yb oven has been positioned to avoid line-of-sight of the viewports, coating of Yb on the windows was observed during the reconstruction of the 2D-MOT beam arms. The severity of coating is not the same on the two arms of the 2D-MOT. Therefore, different laser powers are distributed on the two arms (2D-MOT1: 44mW after fiber; 2D-MOT2: 30mW after fiber. see Fig 6.11(b)). The quadrupole magnetic field required to operate the 2D-MOT is provided by a pair of permanent bar magnets (each composed of six magnets, KJ Magnetics BX062), giving a field gradient of 4.8 mT/cm.

Compared with the legacy setup mentioned in [34, 35], there are a few differences in the current setup. First, the separation between the 2D-MOT to the 3D-MOT capture region is larger in the current setup, which is approximately 40 cm. The longer travel distance leads to two complications in delivering atoms to the 3D-MOT. The first

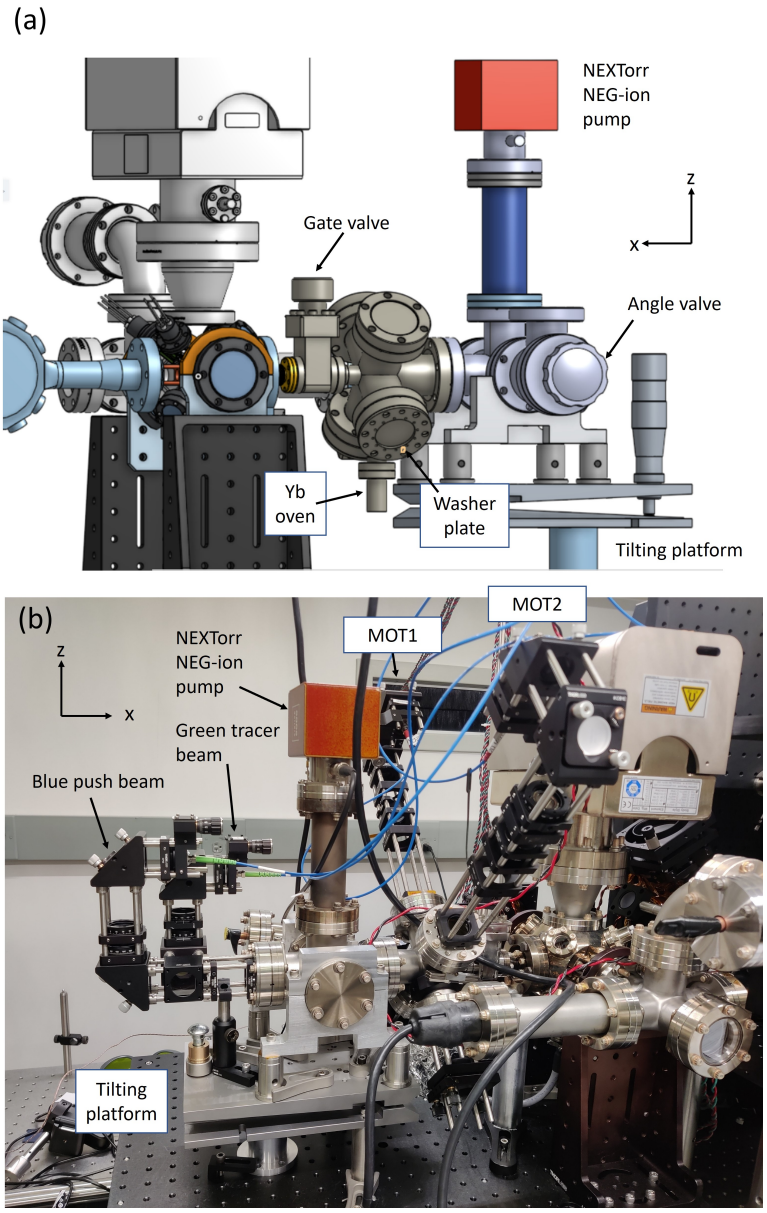

Figure 6.11: Yb 2D-MOT design. (a) Render of the Yb 2D-MOT chamber. (b) Photo of the Yb 2D-MOT with the cage-mounted 2D-MOT arms, the green tracer beam and the blue push beam.

complication is the gravitational sag. Considering an atom leaving the 2D-MOT with a velocity of 10 m/s along the longitudinal axis, it will drop by 8 mm over the course of its trajectory, which is not negligible given an approximately 1 cm beam diameter of the 3D-MOT beam in the current setup. Therefore, the 2D-MOT module sits on a tilting platform (Newport TGN160) with a tilting range of $\pm 2.86°$. If the shooting angle of the atoms is tilted up by one degree, the gravitational fall during the travel to the 3D-MOT is reduced to 1 mm under the same departure speed of 10 m/s from the 2D-MOT. Another complication comes from the finite Doppler temperature of atoms ($\sim 700\mu K$) in the blue 2D-MOT, resulting in a Boltzmann distribution of initial velocities in the transverse plane perpendicular to the pushing direction. This transverse bloom was not an issue in the old setup, since the 3D-MOT beam had a diameter of more than an inch, and the separation between the 2D-MOT and 3D-MOT was significantly shorter. However, in the current setup, the 3D-MOT beams have much smaller diameters ($\sim$ 1 cm) and the atoms have to travel a longer distance to reach the 3D-MOT, making the current setup susceptible to the transverse bloom. Assuming the expansion speed of the atomic cloud in the transverse direction is $\sqrt{\hbar\Gamma_{^1P_1}/m_{\mathrm{Yb}}} = 0.26$ m/s, the cloud will expand to a diameter of 2 cm which is comparable to the 3D-MOT beam diameter.

In the first few trials of realignment of the 2D-MOT beams and the push beam, we were unable to get any fluorescence signal with a green 3D-MOT in the glass cell with similar laser powers and laser frequencies as the legacy setup. We also tried intercepting the atomic beam with a 399 nm probe light to see if the atoms were able to pass through the differential pumping tube hole, but we could not see any signal. Since there are many degrees of freedom involved and the additional complications mentioned in the previous

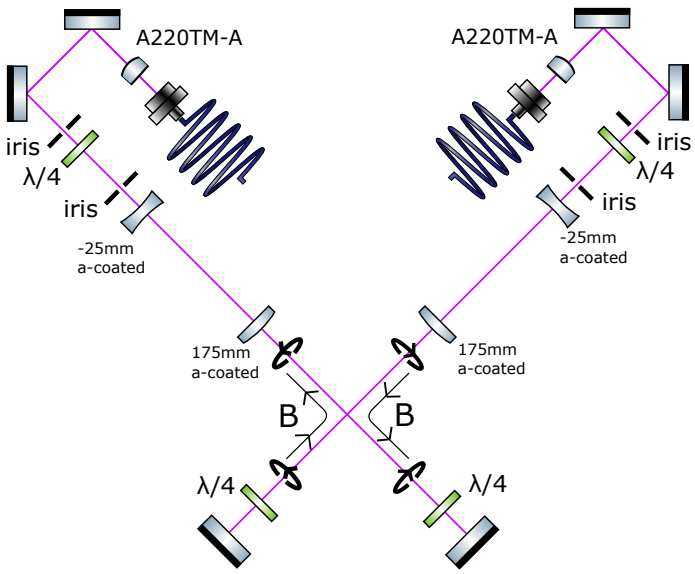

Figure 6.12: Schematic of Yb 2D-MOT optics

paragraph, we have made some changes to the 2D-MOT setup, which enabled us to observe a Yb 3D-MOT in the glass cell at the end. The first change we made was constructing a blue (399nm) 3D-MOT. The blue 3D-MOT provides a higher capture velocity than the green MOT for the same power and beam size. The capture velocity was estimated to be 49 m/s for a blue 3D-MOT and 3 m/s for a green 3D-MOT. This higher capture velocity allows us to replace the green push beam in the original design with a blue push beam, which can provide the atoms with a larger acceleration and thus a higher travel speed, thereby partly mitigating the gravitational sag and transverse bloom. To have a quantitative comparison, we performed a Monte-Carlo simulation of the trajectory of atoms coming out of the 2D-MOT under different push beam powers for both blue and green push beams. We calculated the probability of atoms reaching the 3D-MOT capture volume without hitting the wall of the differential pumping tube and the neck of the glass cell. Furthermore, the portion

Blue push beam and blue 3D-MOT			
Power (mW)	Enter 3D-MOT (%)	Trapped (%)	Tilting angle (°)
0.1	2.6	2.6	1
1	4.4	3.1	1
10	5.4	1.9	0
20	5.7	1.7	0
Green push beam and green 3D-MOT			
Power (mW)	Enter 3D-MOT (%)	Trapped (%)	Tilting angle (°)
0.1	0.3	0.3	1
1	1	0.4	0
10	2.5	0.2	0
20	3.4	0.2	0

Table 6.3: The percentages of atoms reaching the 3D-MOT capture volume and being trapped in the 3D-MOT. The atoms reaching the trap region with a speed lower than the capture speed were considered trapped and the tilting angle was chosen to maximize the trapping probabilities. Real design parameters were used in the simulation. The ensemble of atoms were assumed to have a Boltzmann distribution of velocity in the plane perpendicular to the push beam due to the Doppler temperature ($\sim 700\,\mu$K) of the blue 2D-MOT. The trapped atoms were also assumed to be randomly distributed in the 2D-MOT tube with a normal distribution, $\sigma_x = 1$ cm, $\sigma_y = \sigma_z = 1$ mm. The push beams were assumed to be blue-detuned by a linewidth Γ.

of atoms that had a speed smaller than the capture speed of the 3D-MOT was found and considered to be trapped in the 3D-MOT. The results are tabulated in table 6.3.

The use of a blue push beam also makes the alignment of the 2D-MOT beams and the push beam less challenging. The output direction of the atomic beam depends critically on the balance of transverse 2D-MOT beams, especially near the exit. In the original setup, a slight imbalance was sufficient to deflect the atoms off-axis due to the large scattering force of blue MOT beams compared with the green push beam. A blue push beam can exert a comparable force along the longitudinal direction, permitting a more attainable alignment. Additionally, we rebuilt the cage-mount fiber-coupled optics for the 2D-MOT

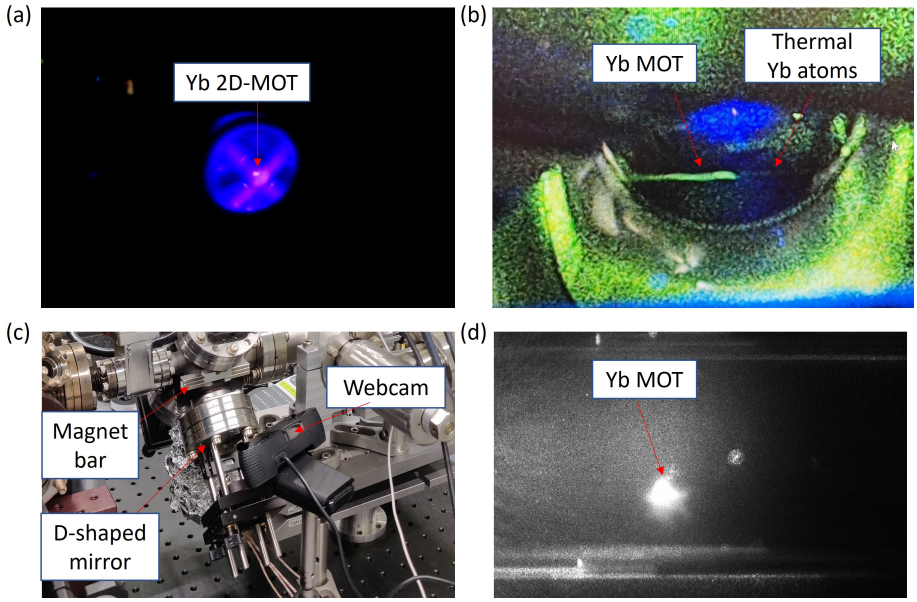

Figure 6.13: (a) Image of the Yb 2D-MOT along the push beam direction. The cross-shaped fluorescence in the background is from the MOT beams and untrapped Yb atoms. (b) Image of the Yb 2D-MOT shined by the green tracer beam. The high-density Yb atoms give a bright fluorescence signal, but the untrapped thermal Yb atoms can also give a faint fluorescence signal. (c) Image of the setup for looking at the 2D-MOT from the side. (d) Image of the Yb trapped in the blue 3D-MOT.

beams as dust-burnt optical elements and fibers severely corrupted the beam profiles. The schematic for the new optical setup is shown in Fig. 6.12.

The realignment of the 2D-MOT beams and the push beam was non-trivial, I shall describe the steps that we took to achieve the Yb 3D-MOT in the glass cell. For the alignment of the 2D-MOT beams, the two irises after the aspheric lens allow a zeroth-order alignment of the 2D-MOT beam normal to the center of the viewport before being expanded by the telescope setup afterward. Due to different degrees of Yb coating on the windows of the 2D-MOT arms, different laser powers were distributed on the two arms (2D-MOT1: 44mW after fiber; 2D-MOT2: 30mW after fiber. see Fig 6.11). After the

zeroth-order alignment of the 2D-MOT beams, the fluorescence signal of the 2D-MOT beam was monitored along the push beam direction with a webcam. (Some webcams do not have a blue light filter and can image the blue 2D-MOT.) The 2D-MOT appeared as a bright pink spot (see Fig. 6.13(a)), which was off-centered from the differential pumping tube hole initially. By shining a laser pointer from the opposite side through the hole to act as a target, the spot was then aligned to the differential pumping tube hole by moving the bar magnets while keeping the spot as bright as possible.

After that, the push beam optics module shown in Fig. 6.11(b), which combined a green (556nm) tracer beam and a blue (399 nm) push beam, was installed. The blue push beam and the green tracer beam were aligned using two irises before the viewport. At this point, the green tracer beam made its way through the differential pumping tube hole and hit the center of the glass cell, but a slight adjustment was made using the window of the glass cell as a reference. By first overlapping the Yb atoms in the blue 2D-MOT with the green tracer beam, we used the green beam as a reference to make sure the blue push beam also hit the atoms in the 2D-MOT. A D-shaped mirror was installed near the viewport of the exit cross arm (see Fig. 6.13(c)) without cutting the 2D-MOT beam. By using a dichroic to block the blue fluorescence light from the blue 2D-MOT, we monitored the green fluorescence light from the Yb atoms (see Fig. 6.13(b)). The fluorescence signal from a thermal cloud of Yb was strong enough to be observed by eyes with an intensity of $I/I_{\text{sat}} \approx 30000$. (The transition was significantly power broadened under this intensity, which caused fluorescence of a large fraction of Doppler broaden atoms.) However, the high atomic density in a 2D-MOT gave a much stronger signal allowing us to distinguish Yb atoms trapped in the 2D-MOT from the thermal cloud. While monitoring the signal

from the side, the bar magnets and 2D-MOT beams were moved to get to a position where the 2D-MOT was appropriately intercepted by the green tracer beam. After realigning the blue push beam to the green tracer beam, the green tracer beam was turned off, and the blue push beam was turned on to deliver atoms to the 3D-MOT. A push beam power of 0.1 mW ($I/I_{\mathrm{sat}} = 0.4$) was used to push the atoms to the blue 3D-MOT. Figure 6.13(d) shows the Yb atoms trapped in the blue 3D-MOT. We also tried using a green tracer beam to push atoms instead, but it required substantially larger laser power ($\sim$ 18 mW) to give a similar signal level in the blue 3D-MOT.

Although the blue 3D-MOT provides a larger capture velocity than a green 3D-MOT, it comes with a cost of higher Doppler temperature (blue 3D-MOT: 700 μK; green 3D-MOT: 4 μK), which is proportional to the linewidth of the transition. A higher temperature of atoms induces difficulties in loading atoms into tweezers, performing high-fidelity gate operations, and high-fidelity lossless fluorescence imaging. Therefore, it is desirable to transfer the Yb atoms from a blue 3D-MOT to a green 3D-MOT in the loading sequence, which has not been implemented yet. The optical setup for the 3D-MOT is still under active development, so the details of the 3D-MOT and optimized loading parameters are not discussed in this thesis.

6.4 MOT Laser Systems and Optical Circuits

As we are going to work on the same atomic species, Rb and Yb, as in the previous experiment, we reused most of the laser locking systems developed in the past, which have proved their reliability over the years, in the hope that this can reduce the technical

overheads that we will encounter. Nevertheless, since we no longer use an Rb Zeeman slower as the Rb source and the original 556 nm 3D-MOT laser from Menlo is down, we modified the original optical layouts for the MOTs as detailed in the following section.

6.4.1 Magento-Optical Trap Lasers

6.4.1.1 Rb 3D-MOT lasers

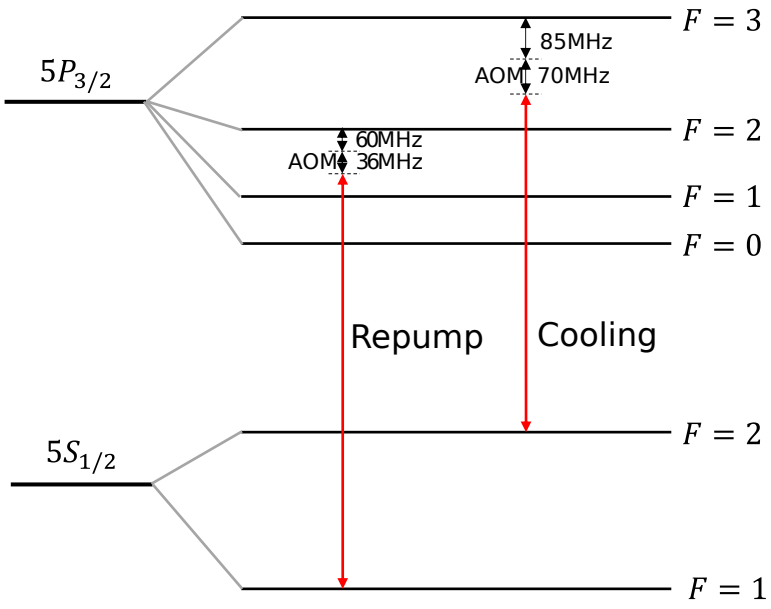

Figure 6.14: Relevant energy levels of the cooling and repump light for Rb 3D-MOT.

There are three separate 780 nm lasers for Rb: A master laser (Newport Vortex II), which is locked to an Rb absorption line (^{85}Rb, $F = 3 \leftrightarrow F' = 3 - 4$ crossover); A cooling laser (Toptica DL pro) for ($F = 2 \leftrightarrow F' = 3$) cycling transition; A repump laser (Toptica DL pro) for ($F = 1 \leftrightarrow F' = 2$) repump transition. Figure 6.14 shows the energy levels relevant to the cooling and repump light for Rb 3D-MOT. The master laser is locked via a

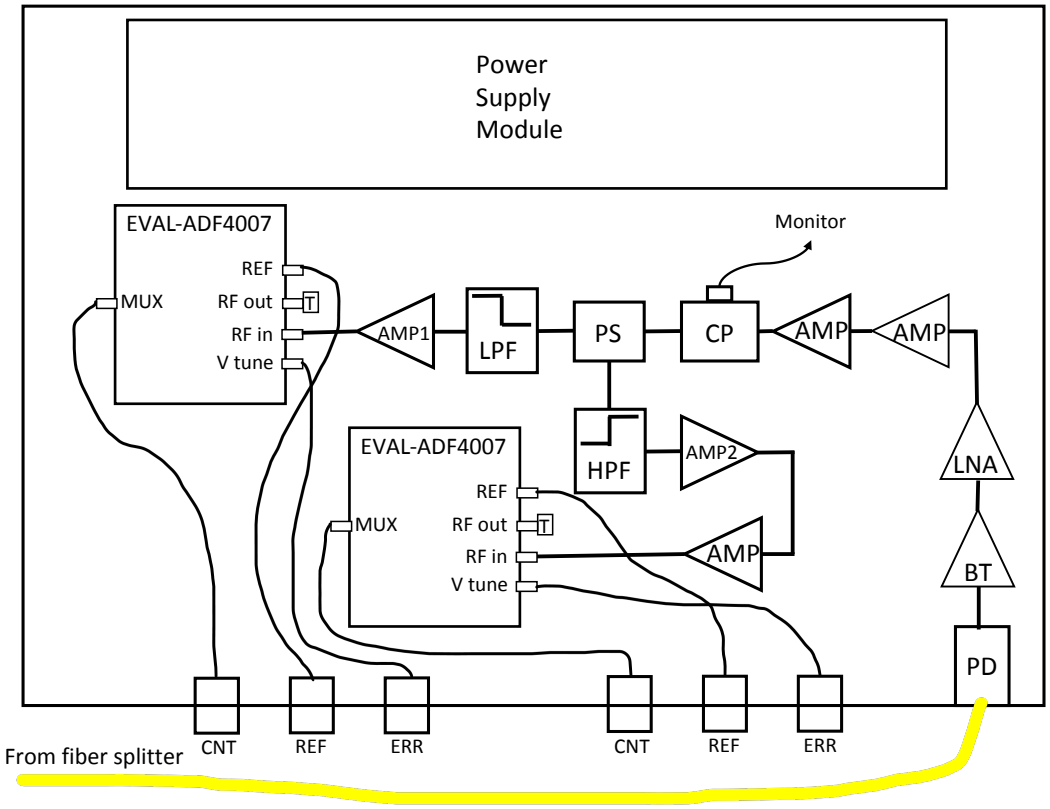

Figure 6.15: Rb beatnote electronics schematic. Following schematic from bottom right-PD: fiber-coupled fast photodiode (Newport 818-BB-45F), BT: bias-tee (Mini-Circuits ZX85-12G-S+), LNA: low-noise amplifier (Mini-Circuits ZX60-83LN-S+), AMP: amplifer (Mini-Circuits ZX60-6013E-S+), CP: directional coupler (Mini-Circuits ZHDC-16-63-S+), PS: power splitter (Mini-Circuits ZFRSC-123-S+), LPF: low-pass filter (Mini-Circuits SLP-2400+), HPF: high-pass filter (Mini-Circuits VHF-2700+), AMP1: amplifier (Mini-Circuits ZX60-4016E-S+), AMP2: amplifier (Mini-Circuits ZX60-8008E-S+), T: 50 Ω terminator.

Doppler-free saturated absorption lock with an optical setup as shown in Fig. 6.16, and it serves as a stable frequency reference for the Rb cooling and repump laser in the beatnote lock. The Rb master laser is also used as a reference to lock the fundamental light of the 399 nm laser at 798 nm for Yb through a transfer cavity lock [112]. Figure 6.16 and 6.18 show the optical schematics for the cooling and repump lasers accordingly. Most cooling and repump beam power is sent to and combined on a fiber splitter/combiner (Canadian Instrumentation Research Ltd., now Evanes- cent Optics, Inc.) for the Rb 3D-MOT. The two inputs are combined and split into six main outputs and two monitor outputs. Only three outputs are used for our retro-reflecting Rb 3D-MOT.

For the laser frequency locking, a small portion of the three 780 nm laser beams is combined through a single-mode fiber splitter (Fiber Optic Network Technology Co.), which combines and divides four inputs equally onto four outputs. One output is sent to a Thorlab Fabry-Perot cavity that allows us to monitor the mode quality on an oscilloscope. Another output from the fiber splitter is coupled directly to a fast fiber-optic photodetector (Newport 818-BB-45F, 12.5 GHz bandwidth) for beatnote locking. The free space photodiode used in the previous setup (Hamamatsu G4176-03) has a tiny sensing area ($\sim$ 0.04 mm^2), which is typical for fast diodes, making the setup extremely sensitive to the alignment. The use of a fiber-coupled photodiode solves the issue of loss of beatnote signals due to misalignment from the fiber launch to the photodiode. The master-cooling ($\approx$ 1.1 GHz) and the master-repump ($\approx$ 5.5 GHz) signals are then amplified, frequency separated, and sent to two independent PLL boards (Analog Devices EVAL-ADF4007)(see Fig. 6.15). A 16 dB directional coupler (Mini-Circuits ZHDC-16-63-S+) is installed to enable real-time monitoring of the beatnote signals. In the PLL board, the input signal is divided by an

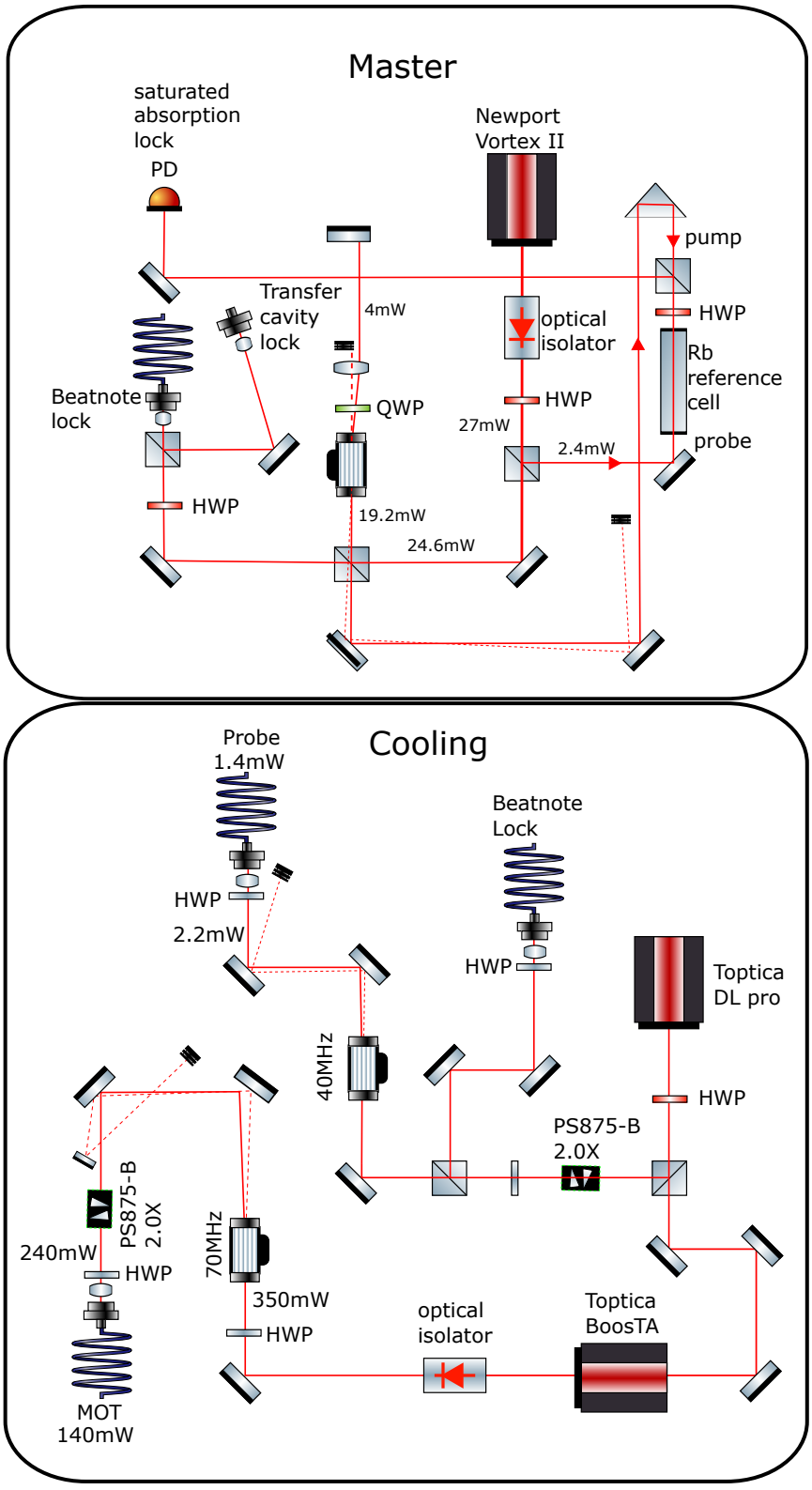

Figure 6.16: Rb master and cooling optics schematic.

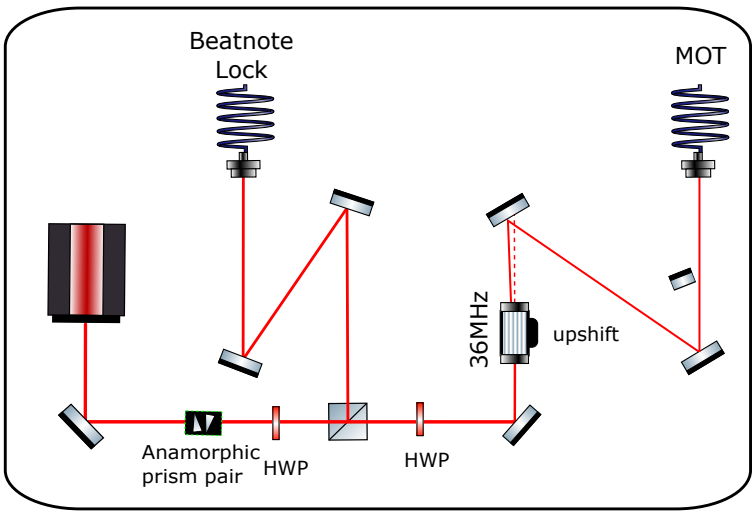

Figure 6.17: Rb repump optics schematic.

integral factor (cooling: 16, repump: 64) set by the jumpers and then compared with an external reference provided by a dynamically adjustable commercial DDS (Novatech 409B). The PLL board has a permanent reference divider of two, so we send in a reference signal of 139.727 MHz for the cooling beam and 172.132 MHz for the repump beam. The MUX outputs of the PLL boards give the divided input signals, which are monitored on RF frequency counters (MFJ Enterprises MFJ-888). The "V tune" outputs are sent to external lock boxes for frequency stabilization. When the laser is locked properly, the frequency displayed on the RF counter should be stable to 100 Hz. A schematic for the beatnote electronics is shown in Fig. 6.15.

6.4.1.2 Yb MOT Lasers

The Yb 2D-MOT, which traps and cools thermal Yb atoms from the oven, uses the 399 nm light as the 2D-MOT beams and the push beam. The 399 nm push beam launches

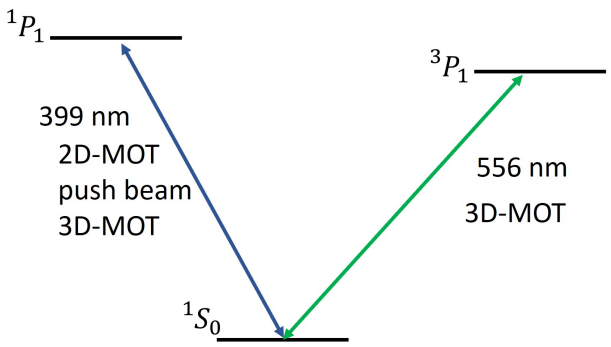

Figure 6.18: Relevant energy levels for 399 nm and 556 nm MOT light in Yb.

the Yb atoms toward the 3D-MOT in the glass cell. The Yb 3D-MOT system contains two colors of light: The blue light (399 nm), which addresses the broad ($^1S_0 \leftrightarrow {}^1P_1$, $\Gamma_{^1P_1} = 2\pi \times 29$ MHz) transition, provides a large capture velocity for atoms. The green light (556 nm), which couples the narrow ($^1S_0 \leftrightarrow {}^3P_1$, $\Gamma_{^3P_1} = 2\pi \times 182$ kHz) inter-combination transition, provides a 4.4μK Doppler temperature and, therefore, a cold atomic ensemble. Yb atoms are first captured in the blue MOT and then transferred to the green MOT for further cooling.

A Toptica TA-SHG pro system generates the 399 nm light. Before being amplified by a tapered amplifier and frequency-doubled, a small portion of the fundamental 798 nm seed light is sampled and sent to a Thorlabs scanning Fabry-Perot interferometer (Thorlabs SA200-5B) for the transfer cavity lock [112]. The Rb master (780 nm), which is locked to an atomic transition line, is sent to the same scanning interferometer to act as a frequency reference. The scanning interferometer serves as a mediator to transfer the frequency stability of the locked Rb master laser to the 798 nm fundamental light through the transfer cavity lock scheme [112]. Figure 6.19 shows the optical layout for distributing the 399 nm

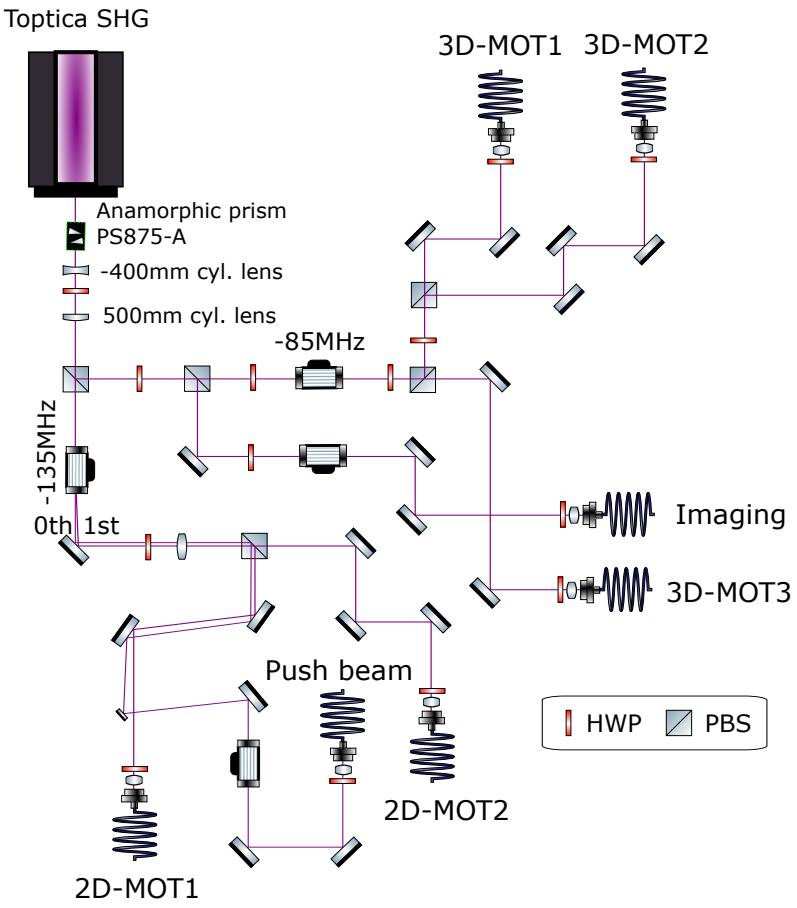

Figure 6.19: A schematic of the optical system for 399 nm light.

light into various beams for different purposes.

The 556 nm light is used to create the green 3D-MOT and the Ryberg excitation through a two-photon process using $^3P_1$ as the intermediate state. The 556 nm laser system is seeded by a 1112 nm NKT Photonics laser ($\sim$ 10 mW). A Quantel fiber amplifier then amplifies the 1112 nm light from the NKT seed to approximately 1W. The amplified 1112 nm light is then sent to a Toptica SHG system, where it is frequency-doubled to give approximately 400 mW of 556 nm light. Figure 6.20 shows the schematic of the 556 nm

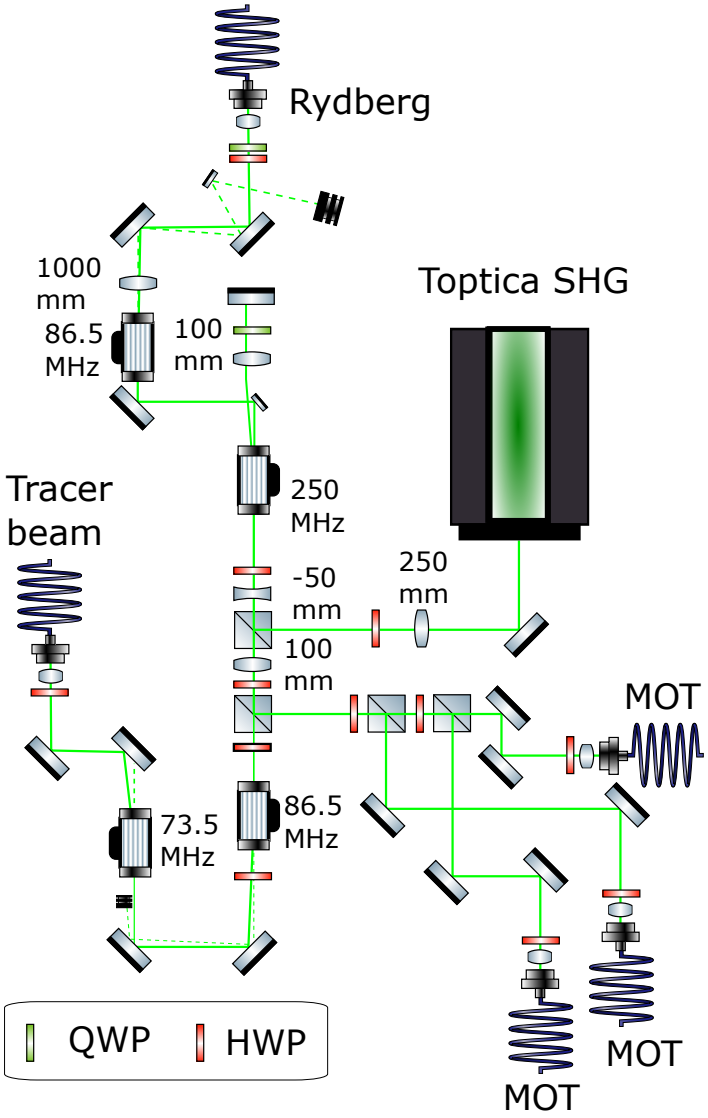

Figure 6.20: A schematic of the optical system for 556 nm light.

optical system. The 556 nm laser is offset locked using a Pound-Drever-Hall (PDH) lock to a variable frequency sideband put on the main laser frequency [89, 113]. The details of locking 556 nm laser can be found in the following section.

6.5 Rydberg lasers

To excite atoms from the ground states to Rydberg states, we will use two-photon excitation via an intermediate state. The reason for not using a single-photon transition is that the excitation from the ground state to the Rydberg state requires light with an extremely short wavelength (Rb: 297 nm, Yb: 198nm). In a two-photon excitation transition, the effective Rabi frequency is given by $\Omega_{\text{eff}} = \frac{\Omega_1 \Omega_2}{2\Delta}$, where Ω_1 and Ω_2 are the Rabi frequencies of the ground-intermediate and intermediate-Rydberg transitions, and Δ is the single-photon detuning from the intermediate state. However, the involvement of an intermediate state leads to a finite probability of spontaneous decay $\Gamma\Omega^2/\Delta$ from the intermediate state for a large detuning. To suppress the spontaneous decay from the intermediate state, a large detuning from the intermediate state $\Delta \gg \Gamma_{\text{intermediate}}$ is usually used, which in turn reduces the effective Rabi frequency to the Rydberg state. Therefore, high Rydberg laser intensities are needed to perform high-fidelity Rydberg excitation with MHz-level Ω_{eff} for quantum computation and simulation purposes.

Figure 6.21 shows the relevant atomic levels and lasers for Rb, where a 420 nm light couples the ground state manifold to the intermediate state manifold ($(5S_{1/2}, F = 2) \leftrightarrow (6P_{3/2}, F = 3)$) with a single-photon detuning Δ_{Rb}, and a 1013 nm light couples the intermediate state to a Rydberg state. The $(6P_{3/2}, F = 3)$ level is chosen as the

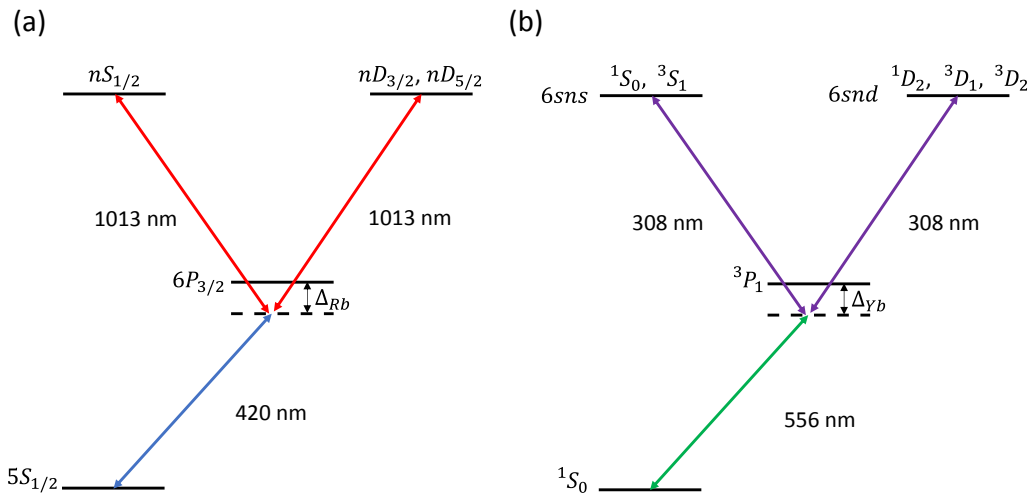

Figure 6.21: Relevant energy levels in Rydberg excitation in (a) Rb, (b) Yb.

intermediate level for two reasons: The first reason is $(6P_{3/2}, F = 3)$ level has a smaller natural linewidth ($2\pi \times 1.4$ MHz) than the Rb D2 line ($2\pi \times 6$ MHz), thereby reducing the spontaneous decay from the intermediate state.; The second reason is to reuse an existing 423 nm laser from the previous RbYb mixture setup. The 420 nm light is generated by a Toptica TA-SHG pro laser inherited from the previous RbYb mixture experiment. The 420 nm laser can provide up to 1W of light with a maximum TA current of 4800 mA. The 1013 nm light is seeded by a Toptica DL pro laser and then amplified to 10 W by the Azurlight fiber amplifier. The larger amount of available laser power in the intermediate-Rydberg arm is preferred in order to compensate for the smaller dipole matrix element of intermediate-Rydberg transition compared with the ground-intermediate transition. All the relevant laser wavelengths for Rb and their functions are summarized in Fig. 6.22.

For Yb, the excitation to Rydberg states is done using $^3P_1$ as the intermediate state. In principle, the $(^1S_0 \leftrightarrow {}^3P_1)$ transition is dipole forbidden due to $\Delta S = 1$, but the

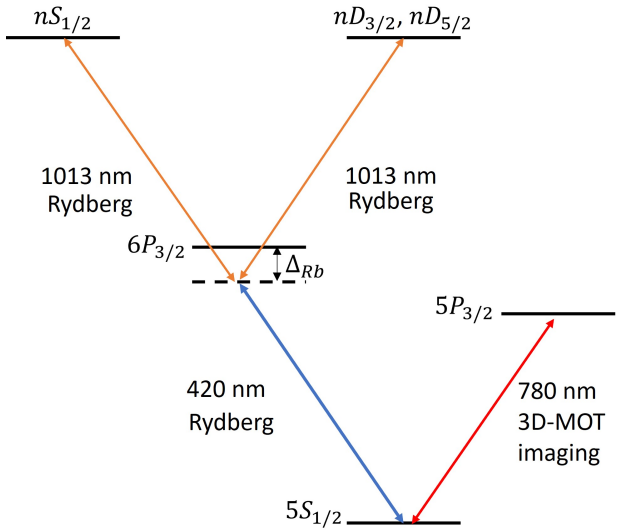

Figure 6.22: Relevant laser wavelengths for Rb and their functions.

singlet-triplet mixing between ${}^1P_1$ and ${}^3P_1$ allows the intercombination transition between $({}^1S_0 \leftrightarrow {}^3P_1)$ and gives a natural linewidth of $\Gamma_{{}^3P_1} = 2\pi \times 182$ kHz. The relatively small natural linewidth of this intercombination transition alleviates the problem of spontaneous decay from the intermediate state. Therefore, instead of the $({}^1S_0 \leftrightarrow {}^1P_1)$ transition, we use the $({}^1S_0 \leftrightarrow {}^3P_1)$ transition. Figure 6.21 shows the relevant atomic levels and lasers for Yb, where a 556 nm light couples the ground state manifold $({}^1S_0)$ to the intermediate state manifold $({}^3P_1)$ with a single-photon detuning Δ_{Yb}, and a 308 nm light couples the intermediate state to a Rydberg state. The 556 nm laser system is seeded by a 1112 nm NKT Photonics laser ($\sim$ 10 mW). A Quantel fiber amplifier then amplifies the 1112 nm light from NKT seed to approximately 1W. The amplified 1112 nm light is then sent to a Toptica SHG system, where it is frequency-doubled to give approximately 400 mW 556 nm laser. The 308 nm laser is provided by a Toptica TA-FHG system. The system consists of an external cavity diode laser for the fundamental 1232 nm light, an external Raman fiber

amplifier, and two cascaded second-harmonic generation stages (SHG pro) to frequency-quadrupled the fundamental light to give 500 mW of 308 nm light. All the relevant laser wavelengths for Yb and their functions are summarized in Fig. 6.23.

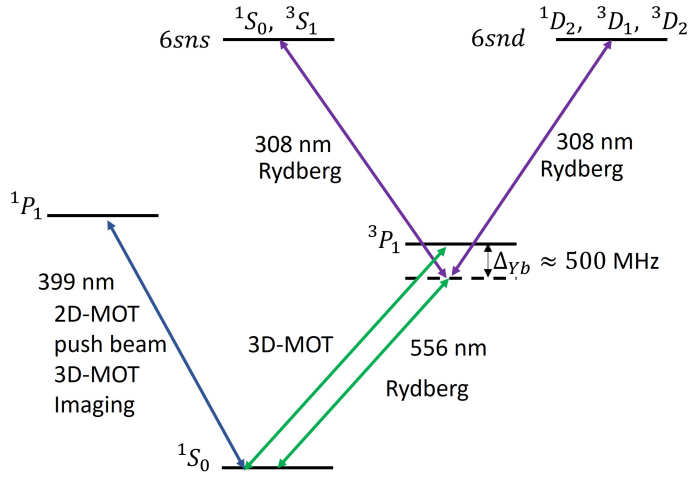

Figure 6.23: Relevant laser wavelengths for Yb and their functions.

6.5.1 Laser Frequency Locking: PDH and Sideband Locking

As discussed in Sec. 5.1, Rydberg states can have a lifetime on the order of a few hundred microseconds, which is significantly longer than the low-lying excited states. As a result, the natural linewidth of the ground-Rybderg transition can be of the order of a few kHz, which is substantially lower than the free-running linewidth of a typical laser, which is on the order of a hundred kHz. Therefore, it is desirable to lock the laser frequency and bring the laser linewidth down to kHz level or even below, so that we can take advantage of the small linewidth of the Rydberg states for high-fidelity gates. In our setup, this is achieved by locking our Rydberg lasers to a high-finesses ultra-low-expansion (ULE) cavity

via PDH-locking to an optical sideband [113], which is a variant of a standard Pound-Drever-Hall (PDH) lock [88, 89].

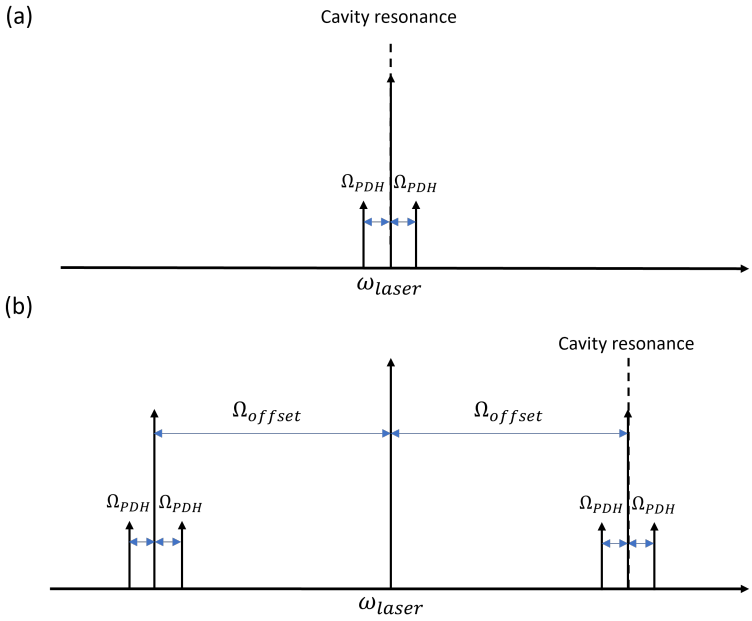

Figure 6.24: Modulation structures for (a) conventional PDH locking, and (b) electronic sideband locking. The dashed vertical line indicates the cavity resonance. In a conventional PDH lock, the laser frequency is locked to the cavity resonance. In the sideband locking scheme, the induced sideband is locked to the cavity resonance and the laser frequency can be adjusted by tuning Ω_{offset}.

In a Pound-Drever-Hall (PDH) lock [88, 89] the laser frequency is stabilized by the mechanical stability of the cavity, such that the round-trip optical path of the cavity equals an integral multiple of the laser wavelength. The resonance frequency spacing of the longitudinal mode of the cavity, i.e. the free spectral range (FSR), is usually of the order of a few hundreds of MHz to a few GHz and is defined as $\nu_{\text{FSR}} = c/(2L)$, where c is the speed of light and L is the length of the cavity. There is usually a gap between the cavity resonance frequency and the target frequency, which can be bridged using acousto-

optic modulators (AOMs) or electro-optic modulators (EOMs). For commercially available AOMs, the center frequency shift ranges from 30MHz to 2.5GHz with high diffraction efficiency for models up to 200MHz, but the tunable range is relatively narrow (±10%) around the center frequency. In EOMs, serrodyne phase modulation can give a maximum efficiency of 60% with a tunable range around a GHz [114, 115].

Alternatively, the electronic sideband locking scheme,[113, 116, 117, 118] which is a modified version of the PDH scheme, can be used. The frequency gap between the cavity resonance and the target frequency can be bridged by introducing a sideband on the laser light with an offset frequency Ω_{offset} allowing locking the carrier frequency of the laser to an arbitrary frequency between the optical resonances of the cavity (see Fig. 6.24). Similar to the standard PDH scheme, the laser is modulated by an RF signal, $V_{\text{EOM}}(t)$, in an EOM. The RF drive signal has a tunable carrier frequency of Ω_{offset} (usually has a range of a few GHz to cover the FSR) and is phase-modulated at a frequency Ω_{PDH} (typically a few MHz) with a modulation depth of β_{PDH}.

$$V_{\text{EOM}}(t) = V_0 \sin(\Omega_{\text{offset}} t + \beta_{\text{PDH}} \sin(\Omega_{\text{PDH}} t)). \tag{6.3}$$

This gives first-order sidebands at $\pm\Omega_{\text{offset}}$ accompanied by an additional set of sidebands with a spacing of Ω_{PDH} as shown in Fig. 6.24. When the sideband of the modulated light at Ω_{offset} is brought close to the resonance of the cavity, the usual PDH error signal can be obtained by demodulating the reflected signal from the cavity at Ω_{PDH}. Therefore, the sideband at Ω_{offset}, instead of the carrier, is tied to the cavity resonance. The offset frequency Ω_{offset} can be tuned to move the laser frequency. This scheme has the advantage

of requiring only a small portion of the laser power to be picked off for sideband locking, and thus the usable laser output power is not limited by the efficiency of AOMs or EOMs.

In principle, the required phase-modulated RF signal $V_{\mathrm{EOM}}(t)$ can be generated from a direct digital synthesis (DDS) chip with phase modulation capability. However, this approach will require high-speed parallel programming and communication, which will involve the use of FPGA, bringing complexity to the design. Quadrature amplitude modulation (QAM) allows us to separate the fast offset signal Ω_{offset}, which can be a few GHz, and the relatively slow PDH modulation signal, Ω_{PDH}, which is only a few MHz. At the same time, the phase modulation now becomes an amplitude modulation on two RF waves at Ω_{offset} that are in quadrature.

$$\begin{aligned} V_{\mathrm{EOM}}(t) &= V_0 \sin(\Omega_{\mathrm{offset}} t + \beta_{\mathrm{PDH}} \sin(\Omega_{\mathrm{PDH}} t)) \\ &= V_0(\cos(\beta_{\mathrm{PDH}} \sin(\Omega_{\mathrm{PDH}} t)) \sin(\Omega_{\mathrm{offset}} t) \\ &\quad + \sin(\beta_{\mathrm{PDH}} \sin(\Omega_{\mathrm{PDH}} t)) \cos(\Omega_{\mathrm{offset}} t)) \\ &= I(t) \sin(\Omega_{\mathrm{offset}} t) + Q(t) \cos(\Omega_{\mathrm{offset}} t), \end{aligned} \tag{6.4}$$

The baseband modulation on the two RF waves are referred to as the in-phase component $I(t)$ and quadrature component $Q(t)$ respectively. We have designed a printed circuit board (PCB) that generates the fast offset signal and takes in the slow PDH modulation signals, $I(t)$ and $Q(t)$, to perform the QAM. The details of the circuit design can be found in the appendix B. The circuit provides a phase-modulated RF signal with Ω_{offset} from 1GHz to 4GHz and Ω_{PDH} below 4MHz. The maximum power output is around 0 dBm. The phase-modulated signal is amplified by an amplifier (Mini-circuits ZFL-2500VH+, 10-2500MHz)

and then sent to the EOM to put the sidebands onto the laser.

6.5.2 ULE Cavity and Sideband Locking Setup

Figure 6.25 shows the schematic of our Rydberg laser locking system. Our experiment has four Rydberg excitation lasers: 420 nm and 1013 nm for Rb; 308 nm and 556 nm for Yb. We lock their fundamental seed light for the frequency-doubled or quadrupled systems (840 nm for 420nm, 1232 nm for 308 nm, and 1112 nm for 556 nm) to a four-bore ULE Fabry-Perot optical cavity, described below. The amplified RF modulation signal for each wavelength, $V_{\mathrm{EOM}}(t)$, is sent to a fiber-coupled EOM (for 1013,1112,1232nm: iXblue NIR-MPX-LN-05-00-P-P-FA-FA; for 840nm: iXblue NIR-MPX800-LN-10-P-P-FA-FA) to introduce the required sidebands for locking. Each of the fundamental beams is then coupled to their designated bore in the four-bore cavity. Fast photodiodes are used to detect the beatnote signals in the reflection from the cavity (PDA10D2: 1013, 1232 nm, PDA8A2: 840 nm, PDA20C2: 1112 nm). The reflected PDH beatnote signal is sent to a mixer (Mini-Circuits ZAD-8+), where it is mixed with a demodulation signal (see appendix B). The output signal of the mixer is then low-pass filtered (Thorlabs EF510 1.7MHz) to give the demodulated PDH error signal. Part of the incoming light is sampled and sent to a scanning Fabry-Perot cavity (Thorlabs SA30-95) for laser mode inspection.

The ULE cavity used in our experiment (Stable Laser System) consists of four pairs of AR-coated mirrors bound to four bores in the ULE glass block. Each pair of mirrors comprises one plano and one concave mirror with a radius of curvature of 50 cm. The separation between mirrors is 10 cm, corresponding to a free spectral range (FSR) of 1.5

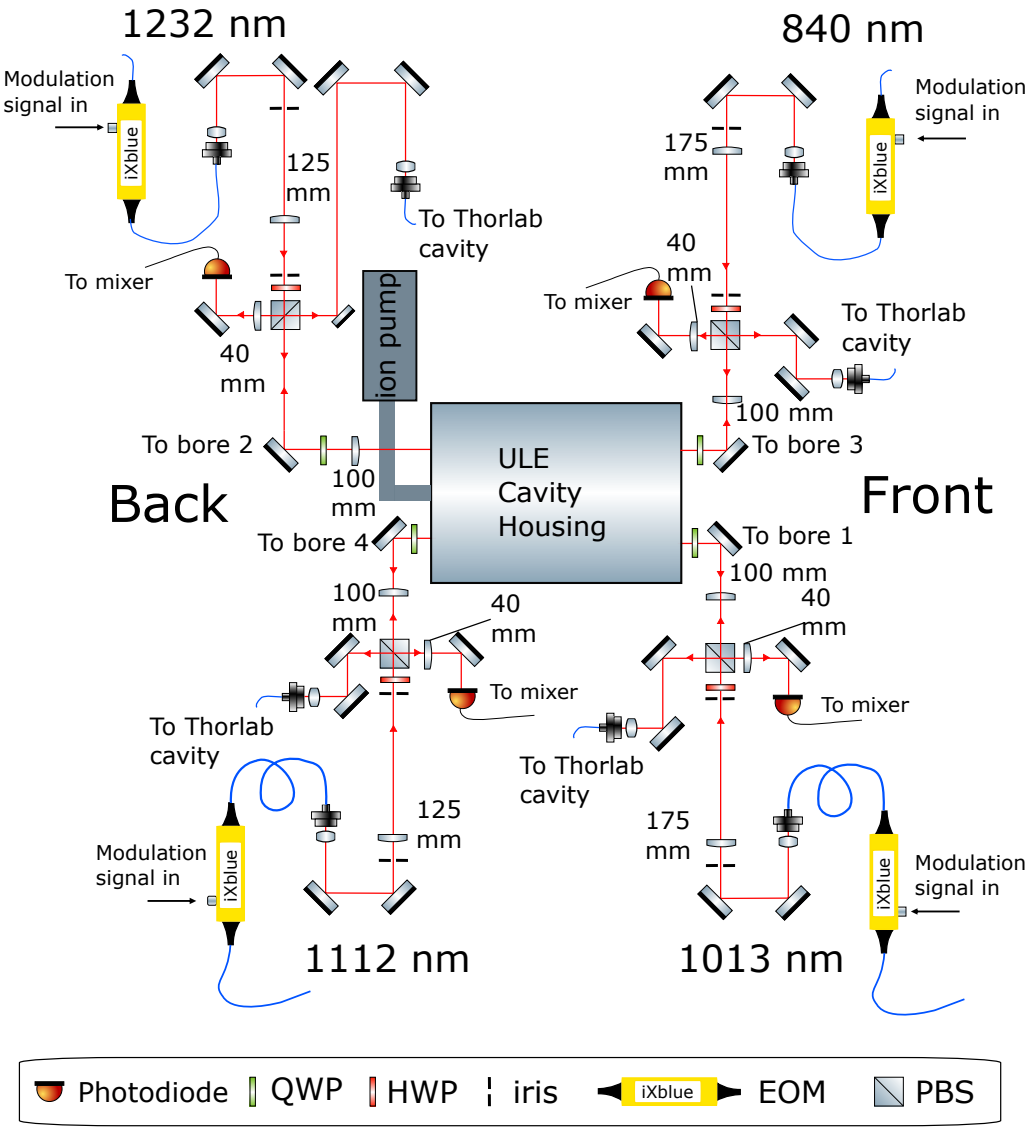

Figure 6.25: Schematic of the ULE cavity setup for electronic sideband locking. The 4-bore ULE cavity is held inside the vacuum chamber in the cavity housing. The fundamental lights of the Rydberg lasers are sent to the designated bores through the cage-mounted alignment assembly. Part of the incoming light is sampled and sent to a scanning Fabry-Perot cavity (Thorlabs SA30-95) for laser mode inspection. Fast photodiodes are used to detect the beatnote signals in the reflection from the cavity.

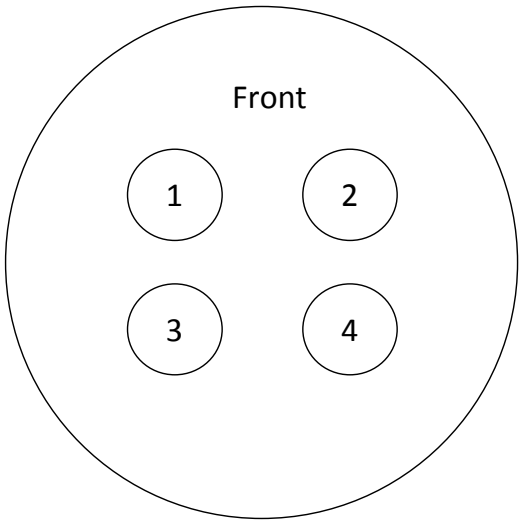

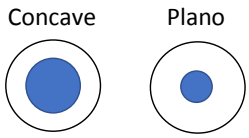

Bore 1	Plano in the front Coating: 840, 1013 nm
Bore 2	Concave in the front Coating: 1112, 1213 nm
Bore 3	Plano in the front Coating: 840, 1013 nm
Bore 4	Concave in the front Coating: 1112, 1213 nm

Figure 6.26: The orientation of the cavity mirrors.

GHz. Two pairs of mirrors share the same coating that works for both 841 and 1013nm light, while the other two pairs have another coating for 1112 and 1232 nm light. The claimed finesses for the coatings are above 60000 for the chosen wavelengths. The orientation of the cavity mirror is shown in Fig. 6.26. To avoid fluctuations in the atmospheric environment, the cavity is housed inside a vacuum chamber with a pressure of 2.4×10^{-7} Torr. The vacuum chamber and the cavity inside are also thermally stabilized to a temperature of 33 °C, where the derivative of the thermal expansion coefficient of the ULE glass is zero.

6.5.3 Lock performance

All the four Rydberg lasers have been locked to the ULE cavity using the electronic sideband locking scheme with the home-built circuit board in a preliminary and unoptimized fashion. The spectral narrowing of lasers has not been verified with a self-heterodyne measurement. In addition, the capability of the lasers to stay locked under an offset

frequency jump needs to be examined after the lock parameters have been optimized. However, preliminary trials show that the lasers remain locked under a jump of 100 kHz.

6.6 Outlook

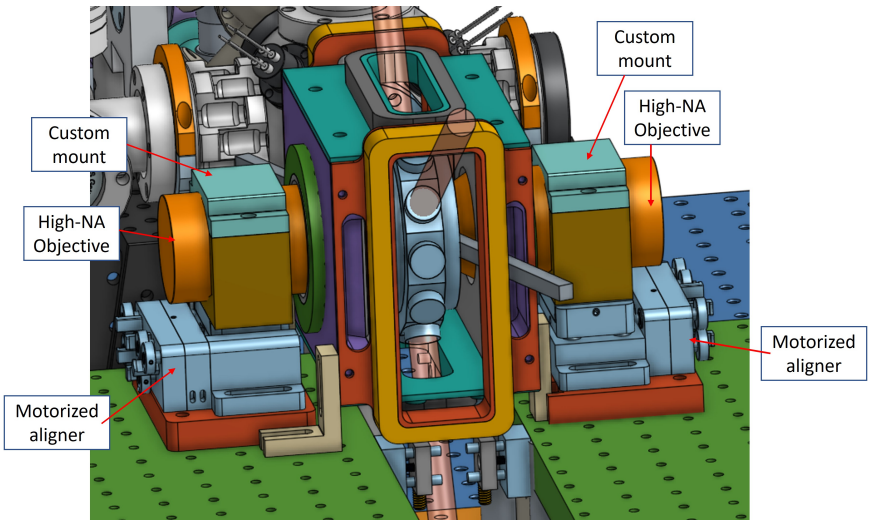

Figure 6.27: The geometry of the objectives with respect to the glass cell

We have realized Rb and Yb 3D-MOTs separately in the glass cell and locked all the lasers, including those for two-photon Rydberg excitation. The next step would be to set up the high-NA imaging optics and cameras. We have two custom-made objectives (Special Optics, model 54-36-30, NA= 0.6, a field of view = 0.2 mm, and a ULTEM housing to avoid magnetic induction). They will be placed on both sides of the glass cell close to the objective windows as shown in Fig. 6.27. The high-NA objectives are held in custom-made PEEK mounts on top of motorized 5-axis tilt platforms (Newport 8081) to facilitate the alignment. We plan to use two scientific imaging cameras on both sides of the glass cell (Andor iXon X3 EMCCD, model number: DU-888D-c00-BV-9JO; Princeton

Instruments, model number: PIXIS 1024B DETECTOR EXCELON). This will give us the capability of dual-sided imaging. The Point Grey Flea2 cameras inherited from the old experiment may be useful for auxiliary purposes such as beam alignment and power calibration. We would also need to incorporate computer control into our system. We plan to implement "labscript suite", which is an open-source python-based experiment control system for automating shot-based experiments and their analysis [119]. Fiber optic USB extenders and PCI/PCIe expansion system (Adnaco-S2A-01-25) will be used to provide USB and PCI/PCIe connections close to the apparatus while preventing ground loops.

After setting the imaging system, we will be ready to generate tweezer arrays and trap atoms. Two 2-axis acousto-optic deflectors (AA Opto-electronics, 532nm: DTSXY-400-532, 850nm: DTSXY-400-850) will be used to generate the tweezer arrays for Rb (850 nm) and Yb (532 nm) respectively. A PCIe arbitrary waveform generator (Spectrum Instrumentation M4i6622-x8) will drive the acousto-optic deflectors independently to deflect light at programmable angles in 2D, which will be mapped into configurable tweezer arrays by the optical system. We will start from a small array where a stochastic loading of atoms should be sufficient. There is a plan to use spatial light modulators to imprint a stationary user-defined trap pattern together with a moving tweezer controlled by a two-axis acousto-optic deflector to rearrange the atoms [120]. Once atoms are trapped, we will be ready to excite atoms into Rydberg states and perform gate operations.

Chapter 7: Conclusion and Outlook

The first half of this thesis focuses on the projects that were carried out in the RbYb degenerate mixture apparatus. I have presented a series of experiments that demonstrated subwavelength control and measurements of cold atoms by manipulating the non-linearity in the three-level system of ^{171}Yb. The first project used this non-linear response to realize a conservative optical lattice with subwavelength ultra-narrow barriers. The scheme can be generalized to higher dimensions and different geometries, allowing nearly perfect box traps, narrow tunnel junctions for atomtronics applications, and dynamically generated lattices with subwavelength spacings. The second project used the non-linear response to shelve a narrow slice of wavefunction density in every unit cell of an optical lattice, allowing us to measure the wavefunction density with a resolution of 10 nm. The third project created a $\lambda/4$-spaced lattice by stroboscopically applying the lattice realized in the first project. Unfortunately, couplings to the spatially and temporally dependent bright states and admixing of states outside the three-level system limit the lifetime of our stroboscopic lattice.

The second half of this thesis describes a new experimental apparatus that is being constructed to trap and manipulate Rb and Yb atoms in optical tweezer arrays for quantum simulation and quantum computation. At the time of writing this thesis, we have created

both Rb and Yb MOTs in the glass cell and locked all the lasers for MOT creation and Rydberg excitation. The next step will be to incorporate computer control, optical tweezer arrays, the optics for Rydberg excitation, and the high-NA optics for imaging and addressing.

As the first step toward a versatile two-species neutral atom quantum computing platform, the first scientific project will involve loading a small number of Rb and Yb atoms into the tweezer arrays and studying the intra- and inter-species Rydberg interaction. This will lay the foundation for future projects trying to tackle the challenges encountered in single-species neutral atom platforms. One direction would be to address the crosstalk issue between nearby qubits. In most neutral atom arrays experiments, the atoms are held in arrays with a separation of a few microns. Single-site imaging and control can be realized with a tightly-focused beam, but scattered photons unavoidably disturb the quantum state of the proximal qubits. Introducing a second atomic element helps mitigate this issue by the vast difference in transition frequencies between different atomic species. According to their intrinsic properties, different atomic qubits can be assigned different tasks to leverage the advantageous properties of each qubit type. For example, the $^1S_0$ ground states of ^{171}Yb has an electronic angular momentum $J = 0$, making it immune to noises such as magnetic field fluctuations and differential light shifts [69, 70]. This makes ^{171}Yb an ideal memory qubit. It could be interesting to map the quantum information from Rb to Yb, where the quantum states are sheltered from environmental noises.

Furthermore, multi-species platforms provide new degrees of freedom, particularly the flexibility to control the intra- and inter-species interaction strength. This extra tuning knob is very useful in realizing multi-controlled multi-target gates, which can provide

significant speedups for quantum algorithms [103, 121, 122] and quantum error correction [76, 123]. By selecting the appropriate pair of Rydberg states for Rb and Yb, we can have a strong van der Waals interaction between the control and target atoms, but weak interaction between control atoms or between target atoms. This asymmetric blockade would allow us to achieve multi-controlled multi-target gates.

Appendix A: Electric Field Calculation

In the COMSOL simulation, we construct the glass cell with the eight tungsten electrodes included using actual design parameters as shown in Fig. A.2. The cube in the center indicates the region of interest, forcing COMSOL to perform delicate meshing to give a more accurate result. The electric potential of one of the electrodes is set to be 1 V and the others set to be 0 V. Then, we run the simulation and export the potential along the three axes around the origin (see Fig. 6.4), which is set at the center of the glass cell. The simulation is repeated for all the electrodes.

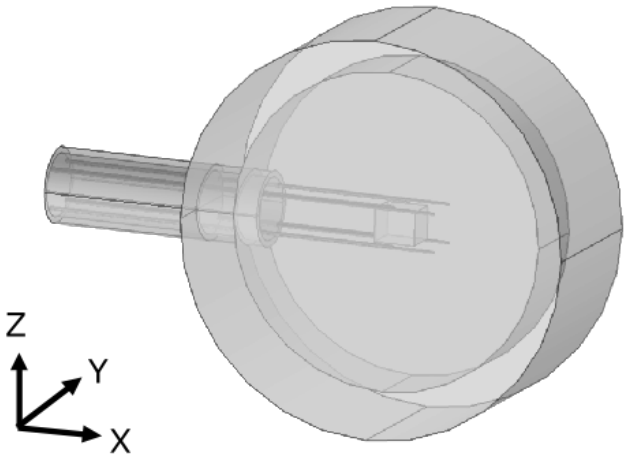

Figure A.1: The geometry used in the COMSOL simulation. The cube in the middle indicated the region of interest and give a finer meshing for a more accurate result.

Our target is to generate an electric field with first-order spatial derivatives equal to zero at the center of the glass cell, such that the electric field is locally homogeneous at the position of atoms. We pair each long electrode with the other long electrode opposite to it (see Fig. A.2), such that each pair of long electrodes gives a dipole-like electric field in the y-z plane that is locally homogeneous near the center. Consider the (Electrode 1 and Electrode 3) pair, it gives an electric field with a magnitude of $E_L = 0.292$ V/cm and $\theta_L = 4.04$ rad, when $V_1 = -V_3 = 1$ V. Similarly, the (Electrode 2 and Electrode 4) pair, it gives an electric field with a magnitude of $E_L = 0.292$ V/cm and $\theta_L = 4.04 + \pi/2$ rad, when $V_2 = -V_4 = 1$ V. Therefore, we have equation 6.1. To give a homogeneous electric field along the x-axis, we set the shorter electrodes to the same voltage such that they only give a homogeneous electric field along the x-axis with no component in the y-z plane.

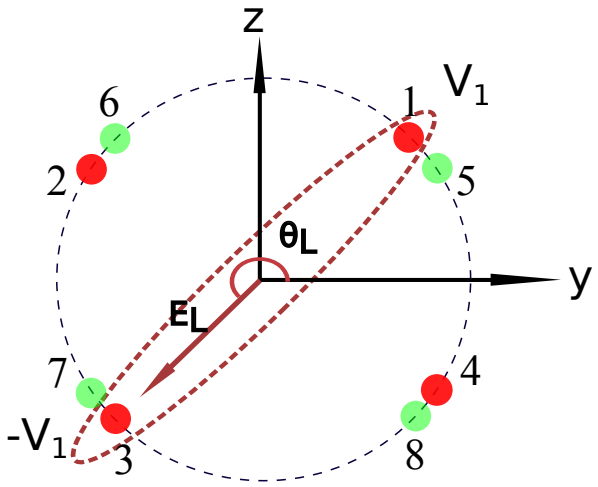

Figure A.2: Illustration of the electrode pairing idea. The electrode 1 and electrode 3 pair. When $V_1 = -V_3 = 1$, they give a dipole-like electric field with magnitude E_L and angle θ_L

Appendix B: Electronic Circuit for Electronic Sideband Locking

This circuit board design is modified from the Analog Devices evaluation board (CN-0285). Design of the board can be found here.[1] The fast carrier wave is provided by the ADF4351 phase-locked loop (PLL) frequency synthesizer chip which has a output frequency range from 35 to 4400 MHz. The chip is controlled using the SPI protocol through a Teensy 3.6 micro-controller board. The lock speed of the PLL chip is around 1 ms, while this speed can be boosted up to around 100 μs at the sacrifice of the phase noise [2]. The fast offset signal is then filtered by a programmable low pass filter (Analog Devices HMC1044) with a tunable cutoff frequency from 1 GHz to 3 GHz. This tunable filter also receives commands from the Teensy board through SPI protocol like the PLL chip, allowing us to block the higher order harmonics in PLL chip output, which degrades the performance of the QAM. The Teensy board empowers platform-independent control through serial communication (microUSB). When a command of frequency update is sent from the control device, the Teensy board determines the appropriate control parameters for both PLL and programmable filter chip and updates the values in the corresponding registers in the chips through SPI interface. The Teensy board is powered directly from the custom-built PCB, so the trace that connects "5V" pads on the Teensy board needs to be cut to isolate the USB power from the rest of

[1] https://github.com/tctsui/ADL5375-ADF4351

[2] https://www.analog.com/media/en/technical-documentation/data-sheets/ADF4351.pdf

the board. The filtered signal is then passed to the quadrature modulator (Analog Devices ADL5375) for QAM. The quadrature modulator has a output frequency range from 400MHz to 6GHz and a broad baseband bandwidth above 100MHz. The baseband inputs (QBBP, QBBN, IBBP, IBBN) of the ADL5375 chip are differential and all the baseband inputs need to be externally dc-biased for best performance. We convert the differential inputs into single-ended by setting IBBP=QBBP=0.5 V, IBBN=I(t)+0.5V and QBBN=Q(t)+0.5V, and have not seen any resulting degradation of performance for the baseband modulation frequency used in this study. The dc voltages at IBBP and QBBP are provided by a tunable internal voltage reference on the board while IBBN and QBBN are provided by an external source described in next paragraph.

The baseband modulation signals, I(t)+0.5V and Q(t)+0.5V, are provided by a STEMlab Red Pitaya 125-14 board which has output sample rate of 125 MSa/s and an output range of $\pm$ 1 V. The STEMlab board can be programmed via a web-based interface or other open-source software through the Ethernet port or microUSB port. The STEMlab board is programmed to output the two baseband modulation signals using the Jupyter Notebook server, which is a built-in application in the Red Pitaya software package. The Ω_{PDH} is chosen to be a rational fraction $125/32 = 3.90625$ MHz of the clock rate of the board. Apart from the fast analog outputs, the STEMlab board also includes 16 fast digital input/output pins with a maximum refresh rate of 125MSa/s on a LVCMOS 3.3V logic. One of the pins is configured to output a square wave with a tunable phase at the frequency Ω_{PDH}. The square wave is filtered by a 5MHz low pass filter before being used for demodulation. The baseband modulation signal and the demodulation signal share the FPGA clock, so they have a definite phase relation as required for demodulation.

To characterize the performance of the circuit board, we generate the $V_{\mathrm{EOM}}(t) = V_0 \sin(\Omega_{\mathrm{offset}} t + \beta_{\mathrm{PDH}} \sin(\Omega_{\mathrm{PDH}} t))$ for $\beta_{\mathrm{PDH}} = \pi/4$, $\Omega_{\mathrm{PDH}} = 3.90625$ MHz at different Ω_{offset} and compare them with the expected waveforms. To simplify the analysis, we perform analog demodulation on $V_{\mathrm{EOM}}(t)$ to extract the amplitude modulation and the phase modulation of the signal. For an ideal $V_{\mathrm{EOM}}(t)$, there is no amplitude modulation. Therefore, we use the resdiual amplitude modulation of the signal to benchmark the quality of the quadrature amplitude modulation. Moreover, we compare the measured phase modulation with $\beta_{\mathrm{PDH}} \sin(\Omega_{\mathrm{PDH}} t)$ to obtain the residual phase modulation. Figure B.1 shows the residual amplitude and phase modulation at different Ω_{offset}. The working frequency range of the circuit board is determined to be from 1 GHz to 4 GHz.

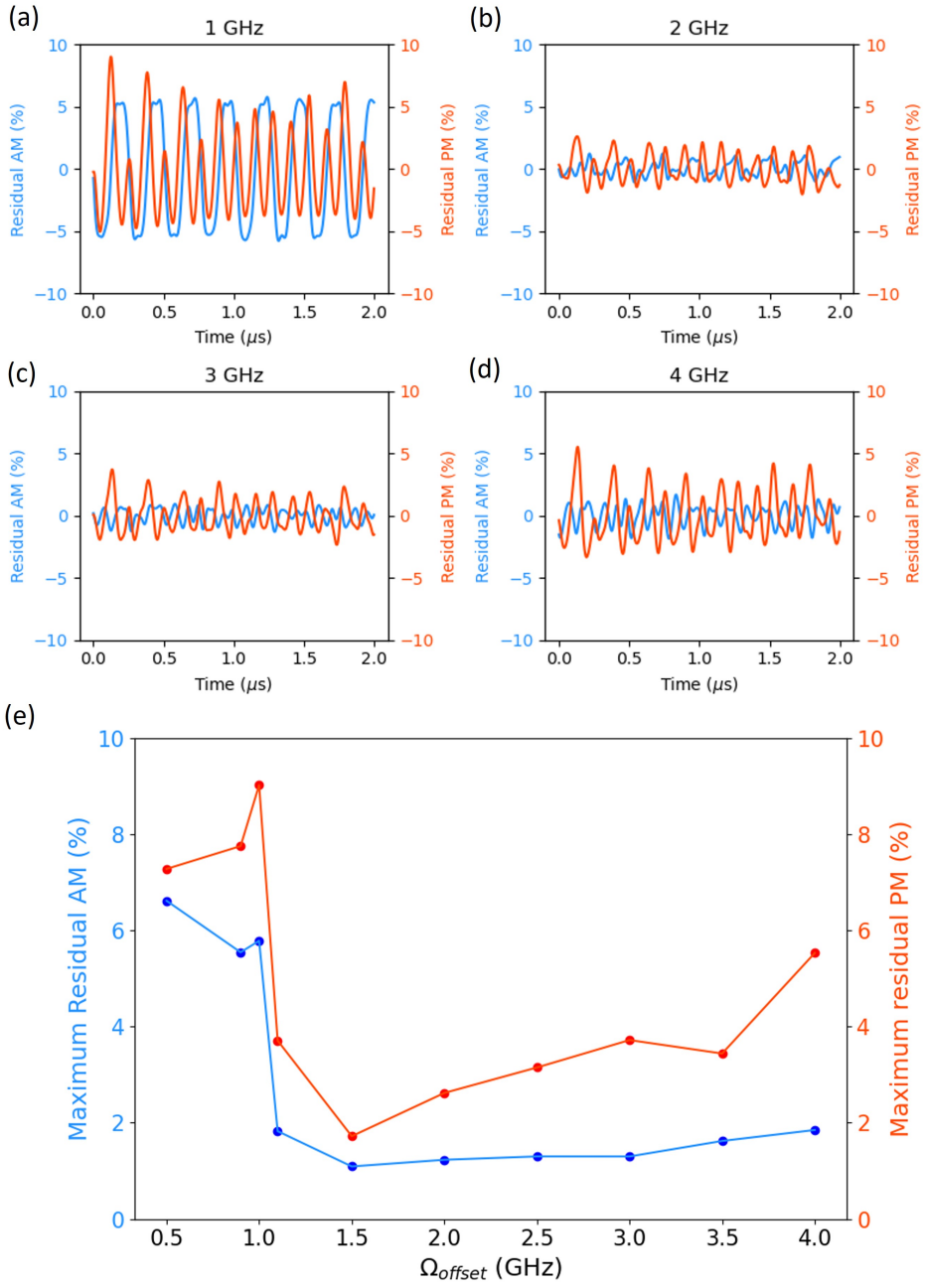

Figure B.1: The residual amplitude and phase modulation at different Ω_{offset}: (a) 1 GHz, (b) 2 GHz, (c) 3 GHz, (d) 4 GHz. (e) The maximum values of amplitude modulation and residual phase modulation at different Ω_{offset}.

Bibliography

[1] Y. Wang, S. Subhankar, P. Bienias, M. Łącki, T-C. Tsui, M. A. Baranov, A. V. Gorshkov, P. Zoller, J. V. Porto, and S. L. Rolston. Dark state optical lattice with a subwavelength spatial structure. Phys. Rev. Lett., 120:083601, Feb 2018.

[2] S. Subhankar, Y. Wang, T-C. Tsui, S. L. Rolston, and J. V. Porto. Nanoscale atomic density microscopy. Phys. Rev. X, 9:021002, Apr 2019.

[3] T-C. Tsui, Y. Wang, S. Subhankar, J. V. Porto, and S. L. Rolston. Realization of a stroboscopic optical lattice for cold atoms with subwavelength spacing. Phys. Rev. A, 101:041603, Apr 2020.

[4] D. Jaksch, C. Bruder, J. I. Cirac, C. W. Gardiner, and P. Zoller. Cold bosonic atoms in optical lattices. Phys. Rev. Lett., 81:3108–3111, Oct 1998.

[5] M. Greiner, O. Mandel, T. Rom, A. Altmeyer, A. Widera, T. W. Hänsch, and I. Bloch. Quantum phase transition from a superfluid to a mott insulator in an ultracold gas of atoms. Physica B: Condensed Matter, 329-333:11–12, 2003.

[6] Masao Takamoto, Feng Lei Hong, Ryoichi Higashi, and Hidetoshi Katori. An optical lattice clock. Nature, 435(7040):321–324, May 2005.

[7] David S. Weiss and Mark Saffman. Quantum computing with neutral atoms. Physics Today, 70(7):44–50, 2017.

[8] Gunnar Ritt, Carsten Geckeler, Tobias Salger, Giovanni Cennini, and Martin Weitz. Fourier synthesis of optical potentials for atomic quantum gases. Phys. Rev. A, 74:063622, Dec 2006.

[9] W Yi, A J Daley, G Pupillo, and P Zoller. State-dependent, addressable subwavelength lattices with cold atoms. New Journal of Physics, 10(7):073015, Jul 2008.

[10] N. Lundblad, P. J. Lee, I. B. Spielman, B. L. Brown, W. D. Phillips, and J. V. Porto. Atoms in a radio-frequency-dressed optical lattice. Phys. Rev. Lett., 100:150401, Apr 2008.

[11] A. González-Tudela, C. L. Hung, D. E. Chang, J. I. Cirac, and H. J. Kimble. Subwavelength vacuum lattices and atom-atom interactions in two-dimensional photonic crystals. Nature Photonics, 9(5):320–325, May 2015.

[12] M. Gullans, T. G. Tiecke, D. E. Chang, J. Feist, J. D. Thompson, J. I. Cirac, P. Zoller, and M. D. Lukin. Nanoplasmonic lattices for ultracold atoms. Phys. Rev. Lett., 109:235309, Dec 2012.

[13] M. Łącki, M. A. Baranov, H. Pichler, and P. Zoller. Nanoscale "dark state" optical potentials for cold atoms. Phys. Rev. Lett., 117:233001, Nov 2016.

[14] F. Jendrzejewski, S. Eckel, T. G. Tiecke, G. Juzeliūnas, G. K. Campbell, Liang Jiang, and A. V. Gorshkov. Subwavelength-width optical tunnel junctions for ultracold atoms. Phys. Rev. A, 94:063422, Dec 2016.

[15] V. D. Vaidya, J. Tiamsuphat, S. L. Rolston, and J. V. Porto. Degenerate bose-fermi mixtures of rubidium and ytterbium. Phys. Rev. A, 92:043604, Oct 2015.

[16] Sylvain Nascimbene, Nathan Goldman, Nigel R. Cooper, and Jean Dalibard. Dynamic optical lattices of subwavelength spacing for ultracold atoms. Phys. Rev. Lett., 115:140401, Oct 2015.

[17] Stephen Eckel, Jeffrey G. Lee, Fred Jendrzejewski, Noel Murray, Charles W. Clark, Christopher J. Lobb, William D. Phillips, Mark Edwards, and Gretchen K. Campbell. Hysteresis in a quantized superfluid 'atomtronic' circuit. Nature, 506:200–203, Feb 2014.

[18] Alexander L. Gaunt, Tobias F. Schmidutz, Igor Gotlibovych, Robert P. Smith, and Zoran Hadzibabic. Bose-einstein condensation of atoms in a uniform potential. Phys. Rev. Lett., 110:200406, May 2013.

[19] W. Morong and B. DeMarco. Simulation of anderson localization in two-dimensional ultracold gases for pointlike disorder. Phys. Rev. A, 92:023625, Aug 2015.

[20] Nathan Gemelke, Xibo Zhang, Chen Lung Hung, and Cheng Chin. In situ observation of incompressible mott-insulating domains in ultracold atomic gases. Nature, 460:995–998, Aug 2009.

[21] W. S. Bakr, A. Peng, M. E. Tai, R. Ma, J. Simon, J. I. Gillen, S. Fölling, L. Pollet, and M. Greiner. Probing the superfluid-to-mott insulator transition at the single-atom level. Science, 329(5991):547–550, 2010.

[22] Maxwell F. Parsons, Anton Mazurenko, Christie S. Chiu, Geoffrey Ji, Daniel Greif, and Markus Greiner. Site-resolved measurement of the spin-correlation function in the fermi-hubbard model. Science, 353(6305):1253–1256, 2016.

[23] Guillaume Salomon, Joannis Koepsell, Jayadev Vijayan, Timon A. Hilker, Jacopo Nespolo, Lode Pollet, Immanuel Bloch, and Christian Gross. Direct observation of incommensurate magnetism in hubbard chains. Nature, 565:56–60, Jan 2019.

[24] A. M. Kaufman, B. J. Lester, C. M. Reynolds, M. L. Wall, M. Foss-Feig, K. R. A. Hazzard, A. M. Rey, and C. A. Regal. Two-particle quantum interference in tunnel-coupled optical tweezers. Science, 345(6194):306–309, 2014.

[25] Jean-Philippe Brantut, Jakob Meineke, David Stadler, Sebastian Krinner, and Tilman Esslinger. Conduction of ultracold fermions through a mesoscopic channel. Science, 337(6098):1069–1071, 2012.

[26] Stefan W. Hell. Far-field optical nanoscopy. Science, 316(5828):1153–1158, 2007.

[27] E. Paspalakis and P. L. Knight. Localizing an atom via quantum interference. Phys. Rev. A, 63:065802, May 2001.

[28] G S Agarwal and K T Kapale. Subwavelength atom localization via coherent population trapping. Journal of Physics B: Atomic, Molecular and Optical Physics, 39(17):3437–3446, Aug 2006.

[29] J. A. Miles, Z. J. Simmons, and D. D. Yavuz. Subwavelength localization of atomic excitation using electromagnetically induced transparency. Phys. Rev. X, 3:031014, Sep 2013.

[30] D. D. Yavuz and N. A. Proite. Nanoscale resolution fluorescence microscopy using electromagnetically induced transparency. Phys. Rev. A, 76:041802, Oct 2007.

[31] Hebin Li, Vladimir A. Sautenkov, Michael M. Kash, Alexei V. Sokolov, George R. Welch, Yuri V. Rostovtsev, M. Suhail Zubairy, and Marlan O. Scully. Optical imaging beyond the diffraction limit via dark states. Phys. Rev. A, 78:013803, Jul 2008.

[32] Alexey V. Gorshkov, Liang Jiang, Markus Greiner, Peter Zoller, and Mikhail D. Lukin. Coherent quantum optical control with subwavelength resolution. Phys. Rev. Lett., 100:093005, Mar 2008.

[33] Nikolay V. Vitanov, Andon A. Rangelov, Bruce W. Shore, and Klaas Bergmann. Stimulated raman adiabatic passage in physics, chemistry, and beyond. Rev. Mod. Phys., 89:015006, Mar 2017.

[34] Creston David Herold. ULTRACOLD MIXTURES OF RUBIDIUM AND YTTERBIUM FOR OPEN QUANTUM SYSTEM ENGINEERING. PhD thesis, University of Maryland, College Park, 2014.

[35] Varun Dilip Vaidya. DEGENERATE MIXTURES OF RUBIDIUM AND YTTERBIUM FOR ENGINEERING OPEN QUANTUM SYSTEMS. PhD thesis, University of Maryland, College Park, 2015.

[36] D. M. Tong, K. Singh, L. C. Kwek, and C. H. Oh. Sufficiency criterion for the validity of the adiabatic approximation. Phys. Rev. Lett., 98:150402, Apr 2007.

[37] Yang Wang, Aishwarya Kumar, Tsung-Yao Wu, and David S. Weiss. Single-qubit gates based on targeted phase shifts in a 3d neutral atom array. Science, 352(6293):1562–1565, 2016.

[38] Mickey McDonald, Jonathan Trisnadi, Kai-Xuan Yao, and Cheng Chin. Superresolution microscopy of cold atoms in an optical lattice. Phys. Rev. X, 9:021001, Apr 2019.

[39] N. Goldman and J. Dalibard. Periodically driven quantum systems: Effective hamiltonians and engineered gauge fields. Phys. Rev. X, 4:031027, Aug 2014.

[40] Maciej Lewenstein, Anna Sanpera, Veronica Ahufinger, Bogdan Damski, Aditi Sen(De), and Ujjwal Sen. Ultracold atomic gases in optical lattices: mimicking condensed matter physics and beyond. Advances in Physics, 56(2):243–379, 2007.

[41] Immanuel Bloch, Jean Dalibard, and Wilhelm Zwerger. Many-body physics with ultracold gases. Rev. Mod. Phys., 80:885–964, Jul 2008.

[42] S Subhankar, P Bienias, P Titum, T-C Tsui, Y Wang, A V Gorshkov, S L Rolston, and J V Porto. Floquet engineering of optical lattices with spatial features and periodicity below the diffraction limit. New Journal of Physics, 21(11):113058, Nov 2019.

[43] M. Lacki, P. Zoller, and M. A. Baranov. Stroboscopic painting of optical potentials for atoms with subwavelength resolution. Phys. Rev. A, 100:033610, Sep 2019.

[44] Martin Holthaus. Floquet engineering with quasienergy bands of periodically driven optical lattices. Journal of Physics B: Atomic, Molecular and Optical Physics, 49(1):013001, Nov 2015.

[45] P. Bienias, S. Subhankar, Y. Wang, T-C. Tsui, F. Jendrzejewski, T. Tiecke, G. Juzeliūnas, L. Jiang, S. L. Rolston, J. V. Porto, and A. V. Gorshkov. Coherent optical nanotweezers for ultracold atoms. Phys. Rev. A, 102:013306, Jul 2020.

[46] Jacob F. Sherson, Christof Weitenberg, Manuel Endres, Marc Cheneau, Immanuel Bloch, and Stefan Kuhr. Single-atom-resolved fluorescence imaging of an atomic mott insulator. Nature, 467:68–72, Sep 2010.

[47] T. Wilk, A. Gaëtan, C. Evellin, J. Wolters, Y. Miroshnychenko, P. Grangier, and A. Browaeys. Entanglement of two individual neutral atoms using rydberg blockade. Phys. Rev. Lett., 104:010502, Jan 2010.

[48] L. Isenhower, E. Urban, X. L. Zhang, A. T. Gill, T. Henage, T. A. Johnson, T. G. Walker, and M. Saffman. Demonstration of a neutral atom controlled-not quantum gate. Phys. Rev. Lett., 104:010503, Jan 2010.

[49] Yang Wang, Xianli Zhang, Theodore A. Corcovilos, Aishwarya Kumar, and David S. Weiss. Coherent addressing of individual neutral atoms in a 3d optical lattice. Phys. Rev. Lett., 115:043003, Jul 2015.

[50] Harry Levine, Alexander Keesling, Ahmed Omran, Hannes Bernien, Sylvain Schwartz, Alexander S. Zibrov, Manuel Endres, Markus Greiner, Vladan Vuletić, and Mikhail D. Lukin. High-fidelity control and entanglement of rydberg-atom qubits. Phys. Rev. Lett., 121:123603, Sep 2018.

[51] Ivaylo S. Madjarov, Jacob P. Covey, Adam L. Shaw, Joonhee Choi, Anant Kale, Alexandre Cooper, Hannes Pichler, Vladimir Schkolnik, Jason R. Williams, and Manuel Endres. High-fidelity entanglement and detection of alkaline-earth rydberg atoms. Nature Physics, 16:857–861, Aug 2020.

[52] Manuel Endres, Hannes Bernien, Alexander Keesling, Harry Levine, Eric R. Anschuetz, Alexandre Krajenbrink, Crystal Senko, Vladan Vuletic, Markus Greiner, and Mikhail D. Lukin. Atom-by-atom assembly of defect-free one-dimensional cold atom arrays. Science, 354:1024–1027, 2016.

[53] Daniel Barredo, Sylvain De Léséleuc, Vincent Lienhard, Thierry Lahaye, and Antoine Browaeys. An atom-by-atom assembler of defect-free arbitrary two-dimensional atomic arrays. Science, 354:1021–1023, 2016.

[54] Hyosub Kim, Woojun Lee, Han Gyeol Lee, Hanlae Jo, Yunheung Song, and Jaewook Ahn. In situ single-atom array synthesis using dynamic holographic optical tweezers. Nature Communications, 7, Oct 2016.

[55] M. Saffman, T. G. Walker, and K. Mølmer. Quantum information with rydberg atoms. Rev. Mod. Phys., 82:2313–2363, Aug 2010.

[56] T. A. Johnson, E. Urban, T. Henage, L. Isenhower, D. D. Yavuz, T. G. Walker, and M. Saffman. Rabi oscillations between ground and rydberg states with dipole-dipole atomic interactions. Phys. Rev. Lett., 100:113003, Mar 2008.

[57] M. Reetz-Lamour, T. Amthor, J. Deiglmayr, and M. Weidemüller. Rabi oscillations and excitation trapping in the coherent excitation of a mesoscopic frozen rydberg gas. Phys. Rev. Lett., 100:253001, Jun 2008.

[58] E. Urban, T. A. Johnson, T. Henage, L. Isenhower, D. D. Yavuz, T. G. Walker, and M. Saffman. Observation of rydberg blockade between two atoms. Nature Physics, 5:110–114, Feb 2009.

[59] Alpha Gaëtan, Yevhen Miroshnychenko, Tatjana Wilk, Amodsen Chotia, Matthieu Viteau, Daniel Comparat, Pierre Pillet, Antoine Browaeys, and Philippe Grangier. Observation of collective excitation of two individual atoms in the rydberg blockade regime. Nature Physics, 5:115–118, Feb 2009.

[60] A. Omran, H. Levine, A. Keesling, G. Semeghini, T. T. Wang, S. Ebadi, H. Bernien, A. S. Zibrov, H. Pichler, S. Choi, J. Cui, M. Rossignolo, P. Rembold, S. Montangero, T. Calarco, M. Endres, M. Greiner, V. Vuletić, and M. D. Lukin. Generation and manipulation of schrodinger cat states in rydberg atom arrays. Science, 365(6453):570–574, 2019.

[61] Alexander Keesling, Ahmed Omran, Harry Levine, Hannes Bernien, Hannes Pichler, Soonwon Choi, Rhine Samajdar, Sylvain Schwartz, Pietro Silvi, Subir Sachdev, Peter Zoller, Manuel Endres, Markus Greiner, Vladan Vuletić, and Mikhail D. Lukin. Quantum kibble–zurek mechanism and critical dynamics on a programmable rydberg simulator. Nature, 568:207–211, Apr 2019.

[62] Antoine Browaeys and Thierry Lahaye. Many-body physics with individually controlled rydberg atoms. Nature Physics, 16:132–142, Feb 2020.

[63] Vincent Lienhard, Pascal Scholl, Sebastian Weber, Daniel Barredo, Sylvain de Léséleuc, Rukmani Bai, Nicolai Lang, Michael Fleischhauer, Hans Peter Büchler, Thierry Lahaye, and Antoine Browaeys. Realization of a density-dependent peierls phase in a synthetic, spin-orbit coupled rydberg system. Phys. Rev. X, 10:021031, May 2020.

[64] Pascal Scholl, Michael Schuler, Hannah J. Williams, Alexander A. Eberharter, Daniel Barredo, Kai Niklas Schymik, Vincent Lienhard, Louis Paul Henry, Thomas C. Lang, Thierry Lahaye, Andreas M. Läuchli, and Antoine Browaeys. Quantum simulation of 2d antiferromagnets with hundreds of rydberg atoms. Nature, 595:233–238, Jul 2021.

[65] G. Semeghini, H. Levine, A. Keesling, S. Ebadi, T. T. Wang, D. Bluvstein, R. Verresen, H. Pichler, M. Kalinowski, R. Samajdar, A. Omran, S. Sachdev, A. Vishwanath, M. Greiner, V. Vuletić, and M. D. Lukin. Probing topological spin liquids on a programmable quantum simulator. Science, 374(6572):1242–1247, 2021.

[66] Sepehr Ebadi, Tout T. Wang, Harry Levine, Alexander Keesling, Giulia Semeghini, Ahmed Omran, Dolev Bluvstein, Rhine Samajdar, Hannes Pichler, Wen Wei Ho, Soonwon Choi, Subir Sachdev, Markus Greiner, Vladan Vuletić, and Mikhail D. Lukin. Quantum phases of matter on a 256-atom programmable quantum simulator. Nature, 595:227–232, Jul 2021.

[67] T. M. Graham, M. Kwon, B. Grinkemeyer, Z. Marra, X. Jiang, M. T. Lichtman, Y. Sun, M. Ebert, and M. Saffman. Rydberg-mediated entanglement in a two-dimensional neutral atom qubit array. Phys. Rev. Lett., 123:230501, Dec 2019.

[68] Harry Levine, Alexander Keesling, Giulia Semeghini, Ahmed Omran, Tout T. Wang, Sepehr Ebadi, Hannes Bernien, Markus Greiner, Vladan Vuletić, Hannes Pichler, and Mikhail D. Lukin. Parallel implementation of high-fidelity multiqubit gates with neutral atoms. Phys. Rev. Lett., 123:170503, Oct 2019.

[69] Shuo Ma, Alex P. Burgers, Genyue Liu, Jack Wilson, Bichen Zhang, and Jeff D. Thompson. Universal gate operations on nuclear spin qubits in an optical tweezer array of ^{171}Yb atoms. Phys. Rev. X, 12:021028, May 2022.

[70] Alec Jenkins, Joanna W. Lis, Aruku Senoo, William F. McGrew, and Adam M. Kaufman. Ytterbium nuclear-spin qubits in an optical tweezer array. Phys. Rev. X, 12:021027, May 2022.

[71] T. M. Graham, Y. Song, J. Scott, C. Poole, L. Phuttitarn, K. Jooya, P. Eichler, X. Jiang, A. Marra, B. Grinkemeyer, M. Kwon, M. Ebert, J. Cherek, M. T. Lichtman, M. Gillette, J. Gilbert, D. Bowman, T. Ballance, C. Campbell, E. D. Dahl, O. Crawford, N. S. Blunt, B. Rogers, T. Noel, and M. Saffman. Multi-qubit

entanglement and algorithms on a neutral-atom quantum computer. Nature, 604:457–462, Apr 2022.

[72] M Saffman. Quantum computing with atomic qubits and rydberg interactions: progress and challenges. Journal of Physics B: Atomic, Molecular and Optical Physics, 49(20):202001, Oct 2016.

[73] James M. Auger, Silvia Bergamini, and Dan E. Browne. Blueprint for fault-tolerant quantum computation with rydberg atoms. Phys. Rev. A, 96:052320, Nov 2017.

[74] P. O. Schmidt, T. Rosenband, C. Langer, W. M. Itano, J. C. Bergquist, and D. J. Wineland. Spectroscopy using quantum logic. Science, 309(5735):749–752, 2005.

[75] T. R. Tan, J. P. Gaebler, Y. Lin, Y. Wan, R. Bowler, D. Leibfried, and D. J. Wineland. Multi-element logic gates for trapped-ion qubits. Nature, 528:380–383, Dec 2015.

[76] Michael A. Nielsen and Isaac L. Chuang. Quantum Computation and Quantum Information: 10th Anniversary Edition. Cambridge University Press, 2010.

[77] Daniel Crow, Robert Joynt, and M. Saffman. Improved error thresholds for measurement-free error correction. Phys. Rev. Lett., 117:130503, Sep 2016.

[78] Cheng Sheng, Jiayi Hou, Xiaodong He, Kunpeng Wang, Ruijun Guo, Jun Zhuang, Bahtiyar Mamat, Peng Xu, Min Liu, Jin Wang, and Mingsheng Zhan. Defect-free arbitrary-geometry assembly of mixed-species atom arrays. Phys. Rev. Lett., 128:083202, Feb 2022.

[79] Kevin Singh, Shraddha Anand, Andrew Pocklington, Jordan T. Kemp, and Hannes Bernien. Dual-element, two-dimensional atom array with continuous-mode operation. Phys. Rev. X, 12:011040, Mar 2022.

[80] I. I. Beterov and M. Saffman. Rydberg blockade, förster resonances, and quantum state measurements with different atomic species. Phys. Rev. A, 92:042710, Oct 2015.

[81] Sylvain De Léséleuc, Vincent Lienhard, Pascal Scholl, Daniel Barredo, Sebastian Weber, Nicolai Lang, Hans Peter Büchler, Thierry Lahaye, and Antoine Browaeys. Observation of a symmetry-protected topological phase of interacting bosons with rydberg atoms. Science, 365:775–780, 2019.

[82] Jeremy T. Young, Przemyslaw Bienias, Ron Belyansky, Adam M. Kaufman, and Alexey V. Gorshkov. Asymmetric blockade and multiqubit gates via dipole-dipole interactions. Phys. Rev. Lett., 127:120501, Sep 2021.

[83] V. Negnevitsky, M. Marinelli, K. K. Mehta, H. Y. Lo, C. Flühmann, and J. P. Home. Repeated multi-qubit readout and feedback with a mixed-species trapped-ion register. Nature, 563:527–531, Nov 2018.

[84] Jarryd J. Pla, Kuan Y. Tan, Juan P. Dehollain, Wee H. Lim, John J.L. Morton, Floris A. Zwanenburg, David N. Jamieson, Andrew S. Dzurak, and Andrea Morello. High-fidelity readout and control of a nuclear spin qubit in silicon. Nature, 496:334–338, Apr 2013.

[85] Thomas F. Gallagher. Rydberg Atoms. Cambridge Monographs on Atomic, Molecular and Chemical Physics. Cambridge University Press, 1994.

[86] Robert Löw, Hendrik Weimer, Johannes Nipper, Jonathan B Balewski, Björn Butscher, Hans Peter Büchler, and Tilman Pfau. An experimental and theoretical guide to strongly interacting rydberg gases. Journal of Physics B: Atomic, Molecular and Optical Physics, 45(11):113001, May 2012.

[87] Xiaoling Wu, Xinhui Liang, Yaoqi Tian, Fan Yang, Cheng Chen, Yong-Chun Liu, Meng Khoon Tey, and Li You. A concise review of rydberg atom based quantum computation and quantum simulation. Chinese Physics B, 30(2):020305, feb 2021.

[88] R. W. P. Drever, J. L. Hall, F. V. Kowalski, J. Hough, G. M. Ford, and H. Munley, A. J. Ward. Laser phase and frequency stabilization using an optical resonator. Applied Physics B, 31:97–105, Jun 1983.

[89] Eric D. Black. An introduction to pound–drever–hall laser frequency stabilization. American Journal of Physics, 69(1):79–87, 2001.

[90] K. A. Safinya, J. F. Delpech, F. Gounand, W. Sandner, and T. F. Gallagher. Resonant rydberg-atom-rydberg-atom collisions. Phys. Rev. Lett., 47:405–408, Aug 1981.

[91] Thibault Vogt, Matthieu Viteau, Amodsen Chotia, Jianming Zhao, Daniel Comparat, and Pierre Pillet. Electric-field induced dipole blockade with rydberg atoms. Phys. Rev. Lett., 99:073002, Aug 2007.

[92] Sylvain Ravets, Henning Labuhn, Daniel Barredo, Lucas Béguin, Thierry Lahaye, and Antoine Browaeys. Coherent dipole-dipole coupling between two single rydberg atoms at an electrically-tuned förster resonance. Nature Physics, 10:914–917, Dec 2014.

[93] M. Müller, I. Lesanovsky, H. Weimer, H. P. Büchler, and P. Zoller. Mesoscopic rydberg gate based on electromagnetically induced transparency. Phys. Rev. Lett., 102:170502, Apr 2009.

[94] Mohammadsadegh Khazali and Klaus Mølmer. Fast multiqubit gates by adiabatic evolution in interacting excited-state manifolds of rydberg atoms and superconducting circuits. Phys. Rev. X, 10:021054, Jun 2020.

[95] Aaron W. Young, William J. Eckner, William R. Milner, Dhruv Kedar, Matthew A. Norcia, Eric Oelker, Nathan Schine, Jun Ye, and Adam M. Kaufman. Half-minute-scale atomic coherence and high relative stability in a tweezer clock. Nature, 588(7838):408–413, Dec 2020.

[96] C. J. Ballance, V. M. Schäfer, J. P. Home, D. J. Szwer, S. C. Webster, D. T.C. Allcock, N. M. Linke, T. P. Harty, D. P.L. Aude Craik, D. N. Stacey, A. M. Steane, and D. M. Lucas. Hybrid quantum logic and a test of bell's inequality using two different atomic isotopes. Nature, 528:384–386, Dec 2015.

[97] Minho Kwon, Matthew F. Ebert, Thad G. Walker, and M. Saffman. Parallel low-loss measurement of multiple atomic qubits. Phys. Rev. Lett., 119:180504, Oct 2017.

[98] M. Martinez-Dorantes, W. Alt, J. Gallego, S. Ghosh, L. Ratschbacher, Y. Völzke, and D. Meschede. Fast nondestructive parallel readout of neutral atom registers in optical potentials. Phys. Rev. Lett., 119:180503, Oct 2017.

[99] Loïc Henriet, Lucas Beguin, Adrien Signoles, Thierry Lahaye, Antoine Browaeys, Georges-Olivier Reymond, and Christophe Jurczak. Quantum computing with neutral atoms. Quantum, 4:327, Sep 2020.

[100] A. Fuhrmanek, R. Bourgain, Y. R. P. Sortais, and A. Browaeys. Free-space lossless state detection of a single trapped atom. Phys. Rev. Lett., 106:133003, Mar 2011.

[101] Alexandre Cooper, Jacob P. Covey, Ivaylo S. Madjarov, Sergey G. Porsev, Marianna S. Safronova, and Manuel Endres. Alkaline-earth atoms in optical tweezers. Phys. Rev. X, 8:041055, Dec 2018.

[102] M. A. Norcia, A. W. Young, and A. M. Kaufman. Microscopic control and detection of ultracold strontium in optical-tweezer arrays. Phys. Rev. X, 8:041054, Dec 2018.

[103] Klaus Mølmer, Larry Isenhower, and Mark Saffman. Efficient grover search with rydberg blockade. Journal of Physics B: Atomic, Molecular and Optical Physics, 44(18):184016, Sep 2011.

[104] Lieven M. K. Vandersypen, Matthias Steffen, Gregory Breyta, Costantino S. Yannoni, and et al. Experimental realization of shor's quantum factoring algorithm using nuclear magnetic resonance. Nature, 414(6866):883–7, Dec 2001.

[105] M. Saffman and K. Mølmer. Efficient multiparticle entanglement via asymmetric rydberg blockade. Phys. Rev. Lett., 102:240502, Jun 2009.

[106] Huai-Zhi Wu, Zhen-Biao Yang, and Shi-Biao Zheng. Implementation of a multiqubit quantum phase gate in a neutral atomic ensemble via the asymmetric rydberg blockade. Phys. Rev. A, 82:034307, Sep 2010.

[107] Xiao-Feng Shi. Deutsch, toffoli, and cnot gates via rydberg blockade of neutral atoms. Phys. Rev. Applied, 9:051001, May 2018.

[108] T. Pohl and P. R. Berman. Breaking the dipole blockade: Nearly resonant dipole interactions in few-atom systems. Phys. Rev. Lett., 102:013004, Jan 2009.

[109] I. I. Ryabtsev, D. B. Tretyakov, I. I. Beterov, V. M. Entin, and E. A. Yakshina. Stark-tuned förster resonance and dipole blockade for two to five cold rydberg atoms: Monte carlo simulations for various spatial configurations. Phys. Rev. A, 82:053409, Nov 2010.

[110] Sören Dörscher, Roman Schwarz, Ali Al-Masoudi, Stephan Falke, Uwe Sterr, and Christian Lisdat. Lattice-induced photon scattering in an optical lattice clock. Phys. Rev. A, 97:063419, Jun 2018.

[111] T. G. Tiecke, S. D. Gensemer, A. Ludewig, and J. T. M. Walraven. High-flux two-dimensional magneto-optical-trap source for cold lithium atoms. Phys. Rev. A, 80:013409, Jul 2009.

[112] S. Subhankar, A. Restelli, Y. Wang, S. L. Rolston, and J. V. Porto. Microcontroller based scanning transfer cavity lock for long-term laser frequency stabilization. Review of Scientific Instruments, 90(4):043115, 2019.

[113] J. I. Thorpe, K. Numata, and J. Livas. Laser frequency stabilization and control through offset sideband locking to optical cavities. Opt. Express, 16(20):15980–15990, Sep 2008.

[114] Rachel Houtz, Cheong Chan, and Holger Müller. Wideband, efficient optical serrodyne frequency shifting with a phase modulator and a nonlinear transmission line. Opt. Express, 17(21):19235–19240, Oct 2009.

[115] D. M. S. Johnson, J. M. Hogan, S. w. Chiow, and M. A. Kasevich. Broadband optical serrodyne frequency shifting. Opt. Lett., 35(5):745–747, Mar 2010.

[116] A. Nevsky, S. Alighanbari, Q.-F. Chen, I. Ernsting, S. Vasilyev, S. Schiller, G. Barwood, P. Gill, N. Poli, and G. M. Tino. Robust frequency stabilization of multiple spectroscopy lasers with large and tunable offset frequencies. Opt. Lett., 38(22):4903–4906, Nov 2013.

[117] Gianmaria Milani, Benjamin Rauf, Piero Barbieri, Filippo Bregolin, Marco Pizzocaro, Pierre Thoumany, Filippo Levi, and Davide Calonico. Multiple wavelength stabilization on a single optical cavity using the offset sideband locking technique. Opt. Lett., 42(10):1970–1973, May 2017.

[118] Jiandong Bai, Jieying Wang, Jun He, and Junmin Wang. Electronic sideband locking of a broadly tunable 318.6 nm ultraviolet laser to an ultra-stable optical cavity. Journal of Optics, 19(4):045501, Feb 2017.

[119] P. T. Starkey, C. J. Billington, S. P. Johnstone, M. Jasperse, K. Helmerson, L. D. Turner, and R. P. Anderson. A scripted control system for autonomous hardware-timed experiments. Review of Scientific Instruments, 84(8):085111, 2013.

[120] Kai-Niklas Schymik, Vincent Lienhard, Daniel Barredo, Pascal Scholl, Hannah Williams, Antoine Browaeys, and Thierry Lahaye. Enhanced atom-by-atom assembly of arbitrary tweezer arrays. Phys. Rev. A, 102:063107, Dec 2020.

[121] C. Figgatt, D. Maslov, K. A. Landsman, N. M. Linke, S. Debnath, and C. Monroe. Complete 3-qubit grover search on a programmable quantum computer. Nature Communications, 8, Dec 2017.

[122] Amit Saha, Ritajit Majumdar, Debasri Saha, Amlan Chakrabarti, and Susmita Sur-Kolay. Asymptotically improved grover's algorithm in any dimensional quantum system with novel decomposed n-qudit toffoli gate, 2020.

[123] Toshiaki Inada, Wonho Jang, Yutaro Iiyama, Koji Terashi, Ryu Sawada, Junichi Tanaka, and Shoji Asai. Measurement-free ultrafast quantum error correction by using multi-controlled gates in higher-dimensional state space, 2021.